Strategies for Improving Efficiency and Emissions in Heavy-Duty Diesel Engines

by

Erick Garcia

A dissertation submitted in partial fulfillment
of the requirements for the degree of
Doctor of Philosophy
(Mechanical Engineering)
in The University of Michigan
2021

Doctoral Committee:

Professor André Boehman, Chair
Associate Professor Herek Clack
Assistant Research Scientist Robert Middleton
Professor Margaret Wooldridge

Erick Garcia

garerick@umich.edu

ORCID iD: 0000-0002-0405-7560

ACKNOWLEDGEMENTS

First and foremost I want to thank my wife Diana Torres for her infinite support and dedication throughout my graduate studies, I know I could not have accomplished this without you by my side. I also want to thank my parents, Jesus Garcia and Isabel Ruiz, for instilling in me a strong work ethic and the value of obtaining a higher education. Your sacrifices were not in vain.

I'd like to express my utmost gratitude toward Dr. André Boehman. It is thanks to his unwavering support and belief in my abilities that I was able to complete my doctoral studies. Outside of the truly amazing tools and financial support I was given to complete my studies, Dr. Boehman provided me with the confidence I needed to see my studies through to the end, even when it most felt unattainable. I also want to thank my thesis committee members, Dr. Herek Clack, Dr. Margaret Wooldridge, and Dr. Robert Middleton for their valuable insight on my research.

Next I want to thank Jian Li and Maxwell Taylor at Volvo Trucks North America for their technical support and collaboration throughout my time at Michigan. Working with them on such a high profile project that is the Department of Energy's SuperTruck II program truly helped elevate my technical abilities to those needed to work with such prominent entities.

They say you are only as good as the company you keep, and I am truly blessed to have had such a wonderful cohort of fellow students at the Walter E. Lay Automotive Laboratory. Thanks to Dr. Jonathan Martin and Aaron Garnier for taking me under their wings when I first arrived to the auto lab, just a few weeks removed from my

undergraduate studies. I can never repay the invaluable mentorship I received from Dr. Vassilis Triantopoulos. I can only hope to mentor others in a similar fashion in my future endeavors. Thanks to Kaustav Bhadra for always lending a helping hand whenever I needed it. Many thanks to Dr. Kwang Hee Yoo and Dr. Taehoon Han for being such supportive senior auto lab students who were never too busy to share insights or lend a hand. And thank you to all of those who proudly formed part of the UMich SuperTruck II team: Ryan Sebastian, Keith Heine, Song Lyu, Ivan Carrasco, Stephen Holmquist, Richard Brady, Tara Larkin, Kevin Pabst, and Joseph Trzaska. Joe, I know the research engine that served me so well is in excellent hands and that you will accomplish great work with that test bed.

This work could not have been accomplished without the dedication of all the staff at the University of Michigan's Walter E. Lay Automotive Laboratory. Thank you to Charles Solbrig, William Kirkpatrick, Kent Pruss, and James Elkins. The technical support from Delphi Technologies, Federal-Mogul, and Lotus Engineering were also invaluable to the success of these experiments.

This work was supported by Volvo Trucks North America and the United States Department of Energy (DOE), Office of Energy Efficiency and Renewable Energy (EERE), under Award Number DE-EE0007745.

TABLE OF CONTENTS

LIST OF FIGURES

Figure

LIST OF TABLES

Table

ABSTRACT

This study presents an experimental investigation of the novel combination of a "wave" bowl piston with thermal barrier coatings (TBCs) and Miller cycle intake valve strategies. All experiments were carried out with a single cylinder research engine with fully-flexible valve timing capabilities. The results indicate the wave bowl geometry enables this combination to improve fuel consumption, steady-state engine-out NO_x emissions, and particulate matter (PM) emissions, improving the NO_x-PM tradeoff that compromises diesel engine efficiency. These benefits were achieved at the expense of elevated turbocharger efficiency requirements.

Three TBCs of varying composition and thickness were tested at seven operating conditions of varying speed and load. TBC performance was highly dependent on volumetric efficiency (VE), as cases with reduced VE increased the heat transfer gradient between the combustion gasses and the combustion chamber. The insulative properties of each TBC determined the impact of the aforementioned change in the heat transfer gradient, with the most pronounced effects on fuel conversion efficiency, up to a 0.6% increase, observed at medium and high load operation. The soot oxidation impacts of the wave piston were diminished at higher engine speeds, with the lowest PM emission increases for the TBC cases with reduced VE observed at the low speed conditions.

Early Intake Valve Closing (EIVC) and Late Intake Valve Closing (LIVC) Miller cycle strategies were compared to a conventional intake valve profile at a low speed-medium load condition under constant engine-out NO_x emissions. The reduction in effective compression ratio from using Miller cycle was symmetric around bottom dead

center, while EIVC profiles were more effective at reducing VE than LIVC profiles. The implementation of an overall turbocharger efficiency (η_{TC}) metric clarified the source of discrepancies found in the current body of work on Miller cycle, as studies reporting fuel consumption penalties were typically underutilizing boost capabilities and those reporting significant efficiency improvements were exceeding boost capabilities. Miller cycle profiles yielded 0.5% BSFC and 30% PM emission increases at the baseline η_{TC}. Those penalties were nullified with an 8% relative increase in η_{TC}.

The combined TBC-Miller cycle study compared extreme Miller cycle strategies to a conventional intake valve profile at a low speed-medium load operating point under high boost conditions. Comparisons were made under fixed cylinder composition, engine-out NO_x emissions, and η_{TC} constraints. Miller cycle at fixed cylinder composition demonstrated that LIVC strategies effectively reduced heat transfer losses, elevated exhaust losses, and reduced engine-out NO_x emissions by up to 35%. Extreme LIVC timings increased fuel consumption by 3% because increased exhaust losses exceeded the reduced heat transfer losses. Miller cycle strategies enabled increased charge dilution at the fixed NO_x constraint, improving fuel consumption by 1.3% over the baseline without compromising exhaust temperatures. This study produced the novel insight that varying EGR rates for NO_x control suppresses the benefits of the inherent low NO_x operation of Miller cycle applications. At an equivalent η_{TC} representative of high boost operation, Miller cycle reduced NO_x emissions by 31% and elevated exhaust temperatures relative to the conventional IVC case without compromising fuel consumption. The TBC piston's insulative properties shifted the inflection point of the heat transfer and exhaust loss tradeoff such that the optimum IVC timing is more extreme than with the uncoated piston for the fixed NO_x emissions and η_{TC} cases.

CHAPTER I

Introduction

Medium and heavy-duty vehicles make up a small fraction of total vehicles on the road, yet they account for 24% of total greenhouse gas emissions from the transportation sector [1]. Despite increases in fuel efficiency standards, overall energy consumption for heavy-duty vehicles will increase by 4% through 2050 as a result of increased demand for freight truck travel [2] as shown in Figure 1.1. Although electricity is the fastest-growing energy source in the transportation sector, it is only projected to account for less than 2% of transportation fuel consumption by 2050 [2], also shown in Figure 1.1.

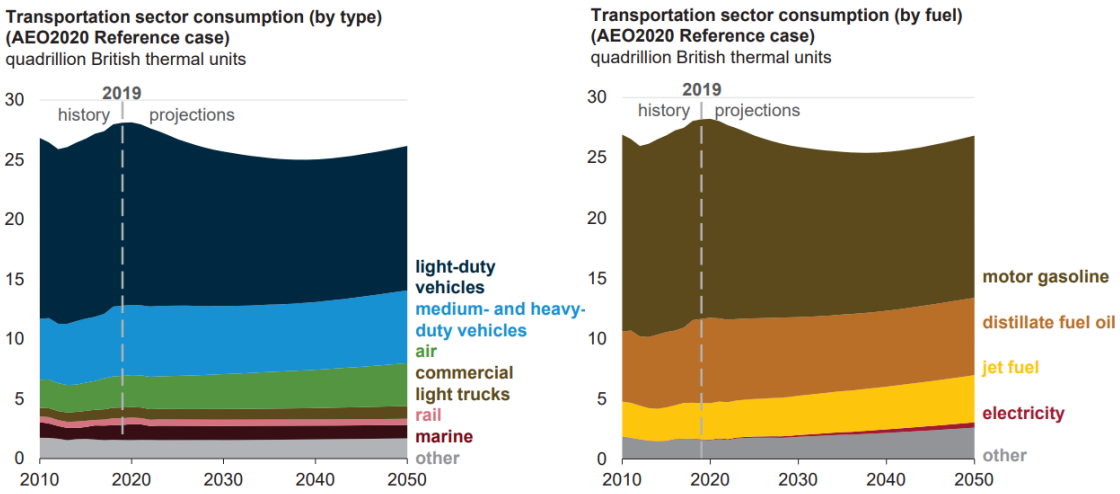

Figure 1.1: 2020 Annual Energy Outlook transportation sector consumption by type (left) and fuel (right) [2].

Given the prominent role the heavy-duty diesel engine will continue to play for the foreseeable future, it is crucial to maximize its fuel conversion efficiency to reduce greenhouse gas emissions. With today's heavy-duty diesel engines only converting approximately 46% of the fuel energy consumed into useful work [3], it is necessary for research efforts to focus on minimizing the losses that decrease fuel conversion efficiency. Reducing cylinder heat transfer losses has the potential to increase thermal efficiency. However, there are difficulties in converting thermal energy retained in the cylinder charge due to reduced heat transfer into work as it most often leads to increased exhaust exergy instead [4].

Thermal barrier coatings (TBCs) are a low heat rejection technology that has shown the capability to promote fuel energy conversion into work instead of waste heat [5]. TBCs in engine applications consist of extremely low thermally conductive materials, ranging from yttria stabilized zirconia ceramics [6] to silica-reinforced porous anodized aluminum [7], applied in thin layers over combustion chamber surfaces. The coated surfaces operate at much higher temperatures than conventional metallic materials can withstand, reducing the gradient driving heat transfer between the combustion gases and combustion surfaces. The theory then is that the diminished heat rejection to the engine coolant will translate to improved work output [8].

Studies have shown that most of the in-cylinder heat transfer is lost through the piston [9, 10], resulting in the prevalence of piston crown coatings in TBC research efforts, such as that in Figure 1.2. Literature on TBC pistons presents a mixed picture, as their performance can vary depending on operating condition [6, 11], coating thickness [12], surface roughness [13] and porosity [14, 15]. The appropriate combination of the aforementioned criteria can lead to increased thermal efficiency [11], while an improper combination can drastically increase soot emissions, exhaust energy instead of work output, or even fuel consumption due to increased heat transfer losses [16]. Naturally aspirated engines in particular experience increased fuel consumption due

to elevated charge temperatures and decreased volumetric efficiency [6].

(a) Uncoated piston crown (b) TBC piston crown

Figure 1.2: Side-by-side view of an uncoated and TBC wave piston crown.

Recent work on TBCs has focused on the "temperature-swing" effect of these coatings, whereby the surface temperature of the combustion chamber wall follows that of the transient gas, as shown in Figure 1.3. O'Donnell et al. [17] stresses that the dynamic effect of surface temperature swing is what positively impacts thermal efficiency, not simply a general insulation and reduction of the cumulative heat loss over the entire cycle. To achieve such large fluctuations in surface temperatures of the insulation coatings a low volumetric heat capacity is needed in addition to low thermal conductivity [7]. Thermal effusivity establishes the relationship between thermal conductivity and volumetric heat capacity and is a measure of a material's ability to exchange heat with its surroundings, defining the material's temperature swing behavior [16]. Thermal effusivity is given by

$$\epsilon = \sqrt{k\rho\ C_p} \tag{1.1}$$

where k is the thermal conductivity, ρ is the density, and C_p is the specific heat capacity of a material.

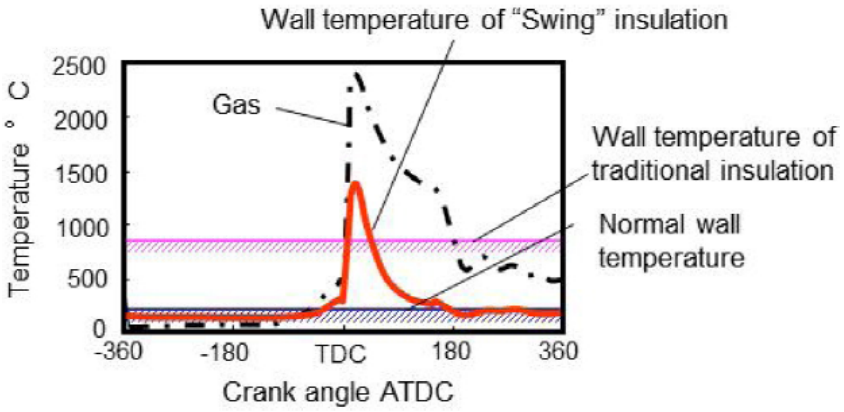

Figure 1.3: Temperature swing effect of TBCs [7].

Selectively coating only certain areas of the piston crown surfaces has also been shown to counteract the negative effects of reduced volumetric efficiency typically associated with TBC applications [18]. Partially coating the piston crown avoids insulating areas that will negatively impact volumetric efficiency, such as near the inlet port. However, the maximum thermal efficiency benefit of the TBC is compromised.

Reducing NO_x emissions is of equal importance to fuel consumption improvements in heavy-duty diesel engines. Current federal emissions standards have lowered overall NO_x emissions, but have not resulted in effective control under all operating conditions. Heavy-duty engines are projected to be one of the largest contributors of mobile source NO_x emissions nationwide well into 2045 [19]. Exhaust aftertreatment systems alone may no longer be able to meet stricter NO_x emission standards, therefore achieving fuel efficiency improvements without increasing engine-out NO_x levels is of great research interest. However, as engines become more efficient exhaust temperatures drop and reduce overall catalyst performance, as shown in Figure 1.4, making it difficult to simultaneously improve fuel consumption and NO_x emissions.

Unconventional valving strategies have been extensively studied to improve fuel conversion efficiency in engines employing advanced combustion strategies [21, 22]. Miller cycle is an alternate cycle that has been proposed to improve both thermal efficiency and NO_x emissions in heavy-duty diesel engines. In a conventional internal

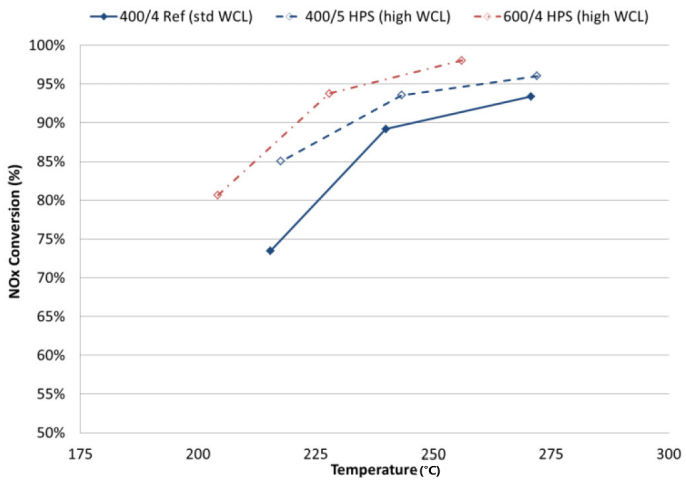

Figure 1.4: Effect of exhaust temperatures on NO_x conversion for three different substrate types with different washcoat loadings [20].

combustion engine, the effective compression and expansion strokes are almost equivalent. With Miller cycle, the effective compression stroke is reduced while the effective expansion stroke is preserved. Ideal air cycle analysis suggests that over-expansion of the working fluid leads to a higher thermal efficiency by increasing the fraction of the expansion work and thus converting energy from the working fluid into work [23, 24]. Miller cycle is commonly implemented using an early intake valve closing (EIVC) or a late intake valve closing (LIVC) timing strategy, as shown in Figure 1.5.

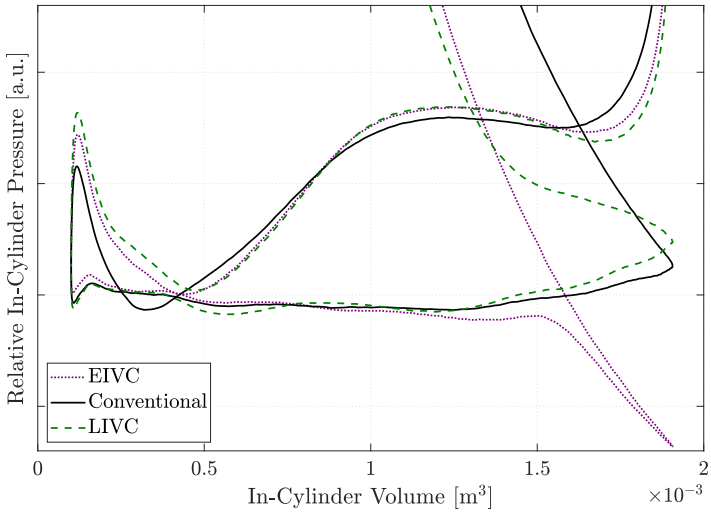

Figure 1.5: Pumping loops for the single-cylinder research engine used in this thesis. EIVC, LIVC, and conventional intake valve closing timings are shown.

Numerous studies have been conducted with the intent of using Miller cycle-based intake valve strategies to improve fuel conversion efficiency and pollutant emissions in heavy-duty diesel engines. The majority of this work can be organized into two broad categories dictated by how intake manifold pressures are utilized.

The first category of past work to consider is that in which Miller cycle strategies are compared to a conventional baseline case at equivalent intake manifold pressures [25–28]. In general, the outcome of these studies point to improved NO_x emissions when utilizing Miller cycle. However, changes in volumetric efficiency (VE) and effective compression ratio (CR_{eff}) compromise fuel consumption and soot emissions.

The other category of Miller cycle studies typically are those conducted at elevated intake manifold pressures such that Miller cycle strategies are compared to a conventional baseline case at equivalent air-to-fuel equivalence ratio (λ) [29–32]. In general, the outcome of these air-fuel ratio parity studies points to improved fuel consumption, but with mixed NO_x emission results when utilizing Miller cycle. While increasing intake manifold pressure for Miller cycle strategies to match the baseline air-fuel ratio improves fuel conversion efficiency over the conventional cases, these studies do not address the requirements and implications associated with producing the increased intake pressures used in their studies.

He et al. [33] considered the effect of delaying IVC on turbocharger efficiency in a light-duty diesel engine, and utilized that metric as a constraint in their experiments. When turbocharger efficiency was held constant, the pressure difference between exhaust and intake manifolds increased as IVC timing was delayed, increasing pumping losses and offsetting fuel consumption gains that could have been achieved with LIVC.

Another deficiency in the current heavy-duty diesel Miller cycle literature is the lack of studies isolating the effect of elevated intake manifold absolute pressures, or intake boost. Given Miller cycle cases require higher intake manifold pressures to improve fuel consumption over the baseline case, conventional intake valve strategies

paired with high boost [34–36] are the true benchmark by which to compare the Miller cycle strategies in the literature reporting improved fuel conversion efficiency.

An additional benefit of EIVC/LIVC applications is the potential to reduce fuel economy penalties associated with emissions control. Guan et al. [37–39] quantified the benefit associated with engine-out NO_x reduction by estimating the change in urea consumption in a selective catalytic reduction system. Miller cycle was found to provide an additional efficiency gain over conventional IVC timing when accounting for the reduction in urea consumption. However, the impact of Miller valve timing on turbocharger performance is not taken into account.

Gosala et al. [40] and Vos et al. [41] have conducted extensive studies with a six-cylinder diesel engine equipped with a camless variable valve actuation system investigating the potential of variable valve actuation strategies to increase exhaust gas temperatures at low load for improved cold start fuel efficiency. At higher engine speeds, LIVC timings take advantage of dynamic charging effects to increase volumetric efficiency over the nominal IVC timing [42]. Utilizing LIVC at high engine speed improved closed cycle efficiency, resulting in BSFC benefits over the baseline.

The body of work on Miller cycle in heavy-duty applications has served to identify key properties associated with EIVC and LIVC profiles and their effect on fuel consumption and emissions. However, prominent differences were observed among the experimental approaches used in each study that make it difficult to draw clear conclusions on whether or not Miller cycle is beneficial for use in a diesel engine. Due to confounding effects of changes in injection pressure, start of injection timing, and EGR dilution, among others, it is difficult to isolate the effect Miller cycle is having on combustion properties and thermodynamic processes.

The Achilles' heel of the diesel engine is the NO_x-soot tradeoff that compromises operation at peak efficiency. Piston bowl geometries have been shown to have a significant influence on the soot emissions from diesel engines [43, 44]. Studies by Genzale

et al. [45] and Pickett et al. [46] identified the influence jet-wall and jet-jet interactions have on soot formation. In a conventional diesel combustion chamber, combustion spray flames collide with one another and compete for oxygen, creating locally rich zones that impede soot oxidation. Increasing compression ratio also increases soot emissions due to poorer mixing conditions in the cylinder caused by a reduction in the chamber volume ratio [47] or set-off length [48].

Volvo's wave piston geometry [49] shown in Figures 1.2 and 1.6 is a novel advancement to combustion chamber design that enhances in-cylinder mixing. Fuel spray interactions in conventional pistons cause significant loss of gas jet velocity as the jets collide with each other. When flame fronts meet, rich zones form as available oxygen is depleted, quenching the flame and forming soot. Eismark et al. [50] found that after the end of injection, the supply of kinetic energy from the injected fuel disappears, allowing the stoichiometric zone to be diluted, resulting in lower temperatures that diminish soot oxidation. The wave piston geometry controls flame propagation, redirecting the fuel-flame jets toward the bowl center and maintaining jet velocity in an oxygen rich environment for more complete combustion and enhanced soot oxidation.

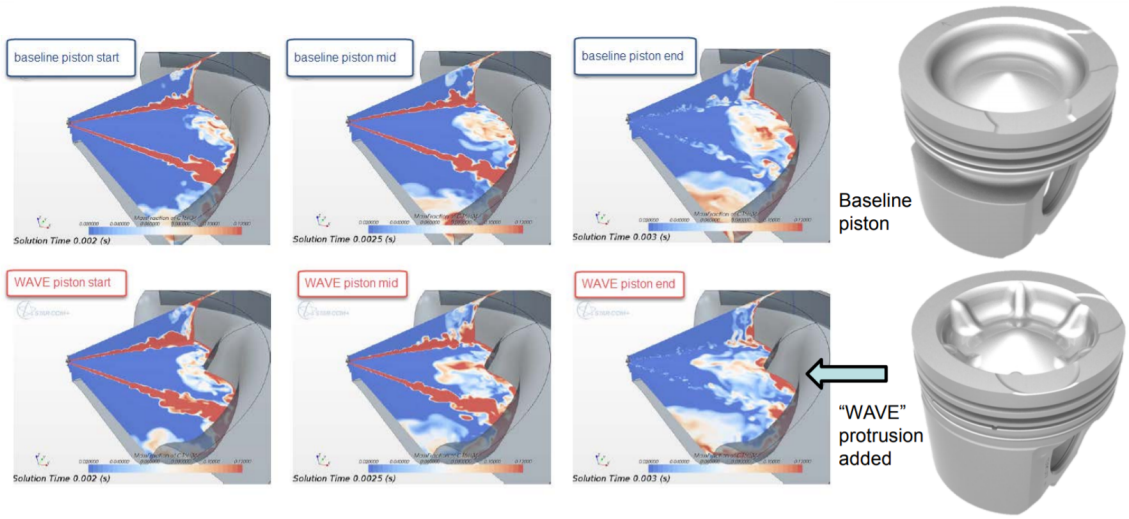

Figure 1.6: In a conventional diesel combustion chamber, flame fronts collide with one another and create rich zones that quench the flame and form soot. The protrusions of the wave bowl piston redirect fuel-flame jets toward the oxygen rich bowl center, improving air entrainment at the end of combustion [51].

The wave piston design has shifted the NO_x-soot curve [52], as shown in Figure 1.7, such that unconventional approaches that would otherwise lead to undesirable soot behavior can be utilized to increase thermal efficiency. Applications that would benefit from the wave design are thermal barrier coatings and Miller cycle intake valve closing timings. As outlined earlier in this section, both strategies have previously been limited in their ability to improve thermal efficiency by their detrimental effect on soot emissions due to reduced volumetric efficiency, and therefore will benefit from the improved soot oxidation of Volvo's wave piston bowl geometry. The goal of this thesis is to leverage the enhanced in-cylinder charge mixing of Volvo's wave bowl geometry to further increase the thermal efficiency of a heavy-duty diesel engine by utilizing Miller cycle and TBCs. The following describes the format and content of this dissertation.

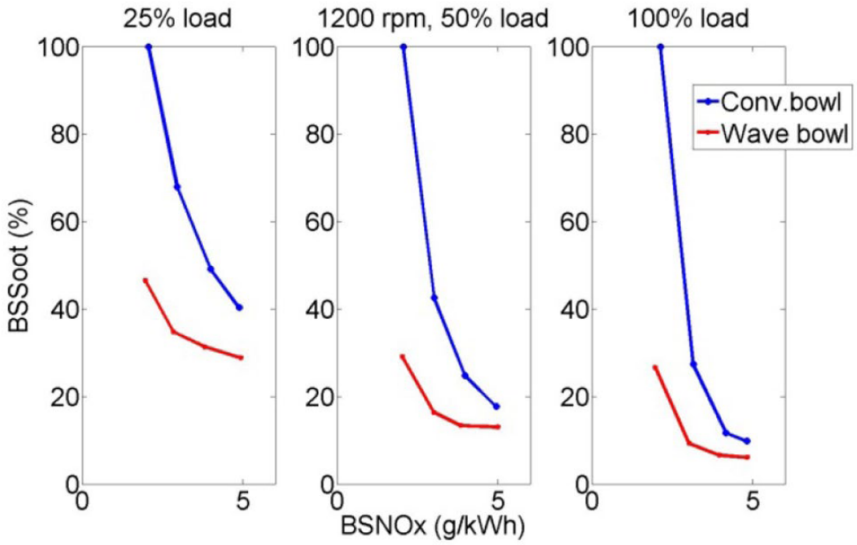

Figure 1.7: Wave bowl vs conventional soot-NO_x tradeoff. The wave bowl piston design shifts the soot-NO_x tradeoff [52], allowing for the implementation of unconventional strategies to improve efficiency.

Chapter II presents the experimental setup of the heavy-duty single cylinder research engine as well as the data analysis methods utilized in these experiments. In Chapter III, the combined influence of the wave bowl geometry and TBCs on the

combustion characteristics, emissions and efficiency of the heavy-duty diesel engines is investigated. The novel application of a TBC to a wave piston bowl will test the soot suppression impacts of this geometry. In Chapter IV, the effect of Miller cycle strategies on the combustion process is isolated to address the shortcomings discussed in the preceding literature review, specifically the implication of turbocharger efficiency on the performance of Miller cycle strategies. Chapter IV was accepted for presentation at the Society of Automotive Engineers 2020 World Congress, under the title of "Impact of Miller Cycle Strategies on Combustion Characteristics, Emissions and Efficiency in Heavy-Duty Diesel Engines". Chapter V builds on the work of Chapter IV to explore how extreme Miller cycle timings and high boost levels can be paired to achieve improved thermal efficiency and NO_x emissions in a heavy-duty diesel engine. Additionally, the effects of pairing TBC pistons with Miller cycle on combustion characteristics is explored. Simulation work on TBC applications has shown that heat losses can be reduced most effectively by increasing the exhaust load rather than striving to achieve a benefit to thermal efficiency [53]. Therefore, Miller cycle and TBC combination could have synergistic effects given the influence of Miller cycle on exhaust temperature. Additionally, both LIVC and EIVC strategies are investigated in an attempt to further identify differentiating characteristics between the two Miller strategies.

CHAPTER II

Experimental Setup and Methods

2.1 Engine Test Bed

2.1.1 Single Cylinder Research Engine with Fully-Flexible Valve Train

The research engine used to conduct the experiments in this thesis is a modified 11L six-cylinder Volvo MD11 heavy-duty direct injection diesel engine that is installed in a state-of-the-art AVL test bed. It has been converted into a single-cylinder research engine by deactivating cylinders 1-5, as shown schematically in Figure 2.1. The detailed engine specifications are listed in Table 2.1.

Table 2.1: University of Michigan MD11 single cylinder research engine specifications.

Parameter	**Value**
Test engine	Volvo MD11
Number of cylinders	1 (5 deactivated)
Displaced volume	1.81 L
Bore x stroke	123 mm x 152 mm
Connecting rod length	225mm
Geometric compression ratio	16.74:1 (Ch.3 and Ch5); 19:1 (Ch. 4)
Cylinder head	4 valves, fully-variable valve timing
Diesel injection system	Common rail
Injector	6 hole nozzle
Piston design	Wave bowl
EGR system	High pressure loop

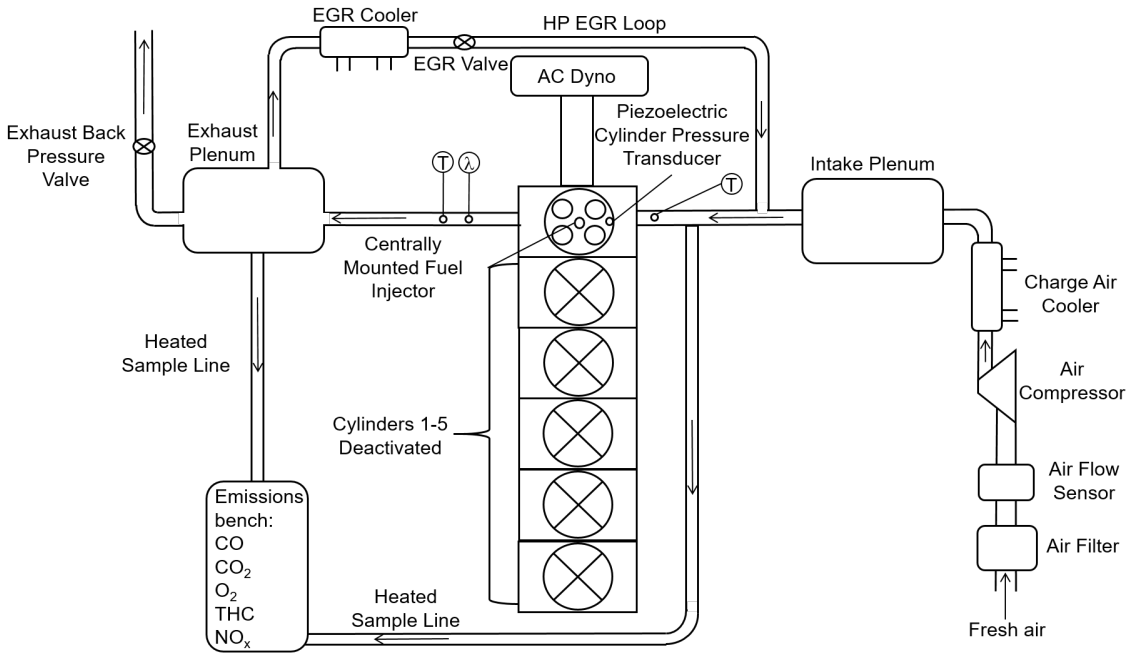

Figure 2.1: Schematic of the single cylinder research engine set up. Engine is based on a 6-cylinder Volvo MD11 where cylinder 6 is the firing cylinder and cylinders 1-5 are deactivated by keeping those valves closed and not energizing those fuel injectors.

The conventional camshaft-rocker valve train has been replaced with an electro-hydraulic Lotus Active Valve Train (AVT) system, as shown in Figure 2.2. This system allows for full control over intake and exhaust valve timing, lift, and velocity.

Figure 2.3 shows multiple views of the Lotus AVT hydraulic actuator assembly [54]. Each actuator has an electro hydraulic servo valve, displacement transducer, and a double-acting piston. A hydraulic power pack supplies pressurized hydraulic fluid to electro-hydraulic servo valves that control the flow of hydraulic fluid proportionally to either the top or bottom of each double-acting actuator piston connected to the engine valve. The displacement transducer provides feedback to the AVT controller as it measures the engine valve position to a resolution of 0.05 mm. Figure 2.4 shows the custom base used to align and house the four AVT actuators used to provide fully independent control of each intake and exhaust valve.

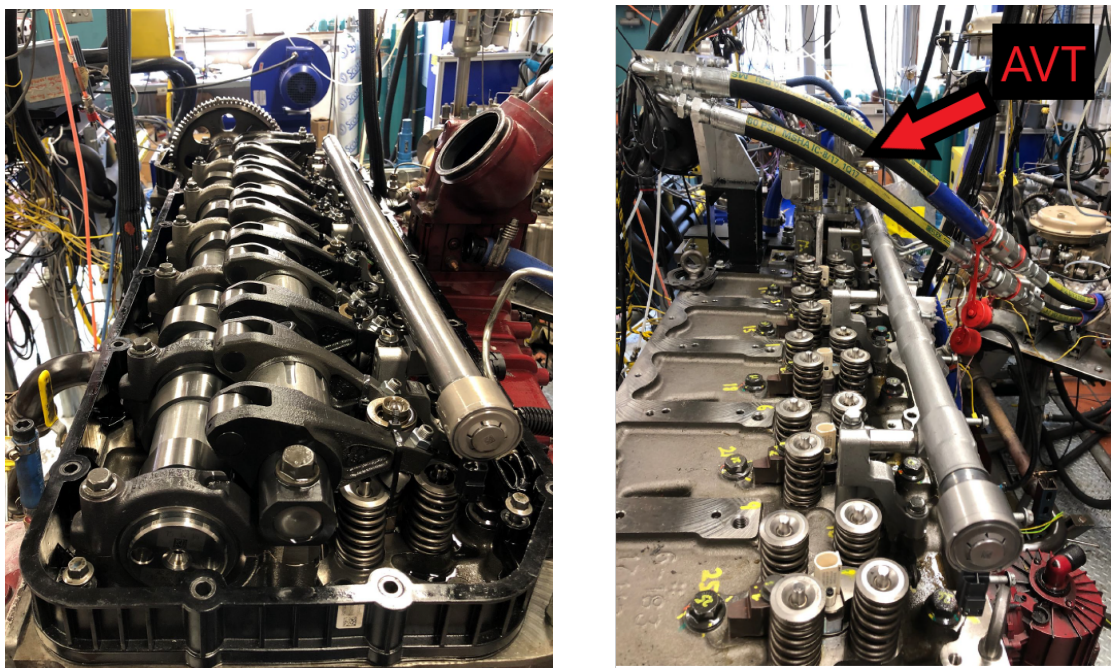

(a) Conventional valve train (b) Lotus AVT

Figure 2.2: The conventional valve train (a) and the Lotus AVT system (b).

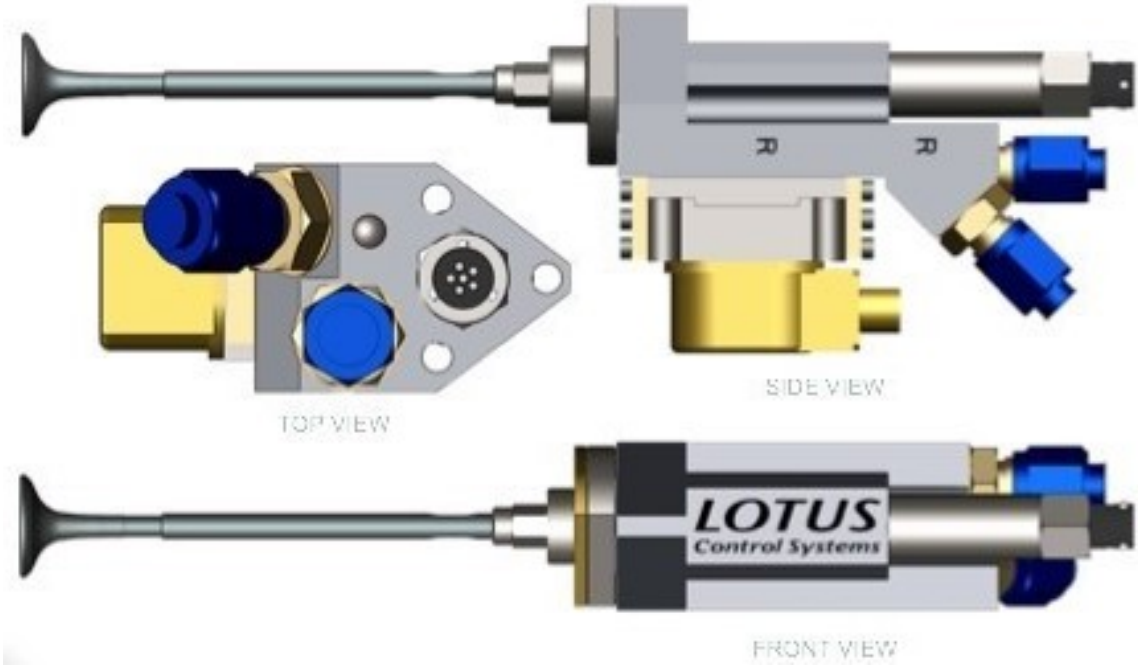

Figure 2.3: Multiple views of the Lotus AVT hydraulic actuator [54].

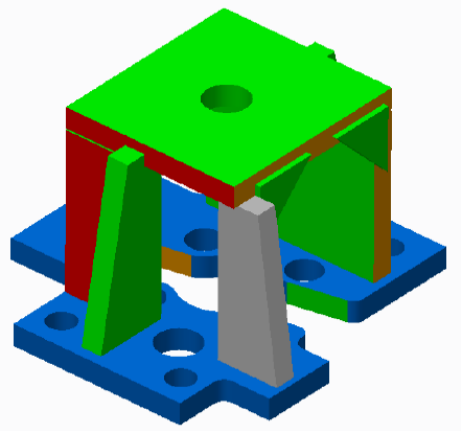

(a) CAD model of actuator base

(b) Actuator base installed

Figure 2.4: CAD model (a) and actual base (b) for AVT actuators on engine head.

2.1.2 Fuel System

The standard engine control unit (ECU) was replaced with one modified by Delphi Technologies for control with Accurate Technologies' VISION calibration and data acquisition software exclusively for control over the engine's fuel injection system, specifically start of injection timing, injection pressure, injection duration, and number of injections. A fuel conditioning system consisting of an AVL 735S fuel mass flow meter and AVL 753C fuel temperature controller was used to deliver bubble free fuel at a constant 25°C to the engine's fuel pump. The specifications and capabilities of these fuel system components are summarized in Tables 2.2 and 2.3. The original gear-driven fuel pump has been replaced with a stand-alone Delphi DFP5 fuel pump, capable of supplying fuel pressures of 300-3000 bar to the Delphi common fuel rail, driven by a Dayton 36VF44 three-phase motor. The original unit injector for the firing cylinder has been replaced with an electronically controlled common rail Delphi injector designed for use with the wave piston. The 6-hole nozzle of this injector

has an optimized spray angle of 150° that precisely directs the fuel spray to enhance interaction with the wave piston protrusions and promote late soot oxidation[52]. The fuel properties for the ultra-low sulfur diesel provided by ExxonMobil for these experiments are listed in Table 2.4.

Table 2.2: Technical specifications of the AVL 735S fuel mass flow meter.

Parameter	**Value**
Measurement range	0-125 kg/h
Systematic measurement uncertainty	$u_s = 0.12\%$
Measurement uncertainty of total consumption	Mass $\leq \pm$(0.05 kg + 0.0001% of MV) Volume $\leq \pm$(0.05 l + 0.0001% of MV)

Table 2.3: Technical specifications of the AVL 753C fuel temperature control unit.

Parameter	**Value**
Fuel Supply Temperature	-10 - 40°C
Cooling Power	1.6 kW
Temperature control range	10 - 80°C
Temperature stability	better than 0.02°C

Table 2.4: Experimental fuel properties provided by ExxonMobil.

Parameter	**Value**
Derived Cetane Number	46.4
Carbon	86.90 wt%
Hydrogen	13.03 wt%
Nitrogen	0.02 wt%
Density at 23°C	850 kg/m^3
Gross heat of combustion	45.4 MJ/kg

2.1.3 Charge Air System

The research engine is equipped with an AVL charge air conditioning system that consists of an Atlas Copco GA55P FF compressor, charge air cooler, and an AVL 515x smart plenum for accurate boost control. The air temperature at the smart

plenum is held constant at 35°C for all experiments. The technical specifications of the charge air system can be found in Table 2.5 and Table 2.6.

Table 2.5: Technical specifications of the Atlas Copco GA55P FF compressor.

Parameter	**Value**
Maximum allowable working pressure	7.15 bar
Maximum volumetric flow rate	183.2 L/s

Table 2.6: Technical specifications of the AVL 515x smart plenum.

Parameter	**Value**
Pressure control range	200-4000 mbar abs.
Pressure control accuracy	± 10 mbar
Temperature control range	30 - 130°C
Temperature control accuracy	± 5°C

The high pressure EGR loop for this engine was developed by students at Pennsylvania State University and Chalmers University to provide better control of the EGR flow rate and temperature than the stock system [55]. A CAD model of the EGR loop is shown in Figure 2.5. The EGR supplied to the engine is cooled by a standalone Thermo Fisher Scientific Thermoflex 500 recirculating chiller before mixing with the fresh air charge in the intake manifold. The technical specifications for the chiller circulator can be found in Table 2.7. A butterfly valve at the end of the exhaust circuit is used to adjust the exhaust back pressure to the minimal level needed to drive the required EGR into the intake manifold. This results in operating under minimal pumping mean effective pressure (PMEP) losses for any given EGR level.

Table 2.7: Technical specifications of the Thermo Fisher Scientific recirculating chiller.

Parameter	**Value**
Model Number	Thermoflex 5000
Cooling capacity	5 kW
High temperature setpoint range	5 - 90°C
High temperature setpoint stability	± 0.1°C

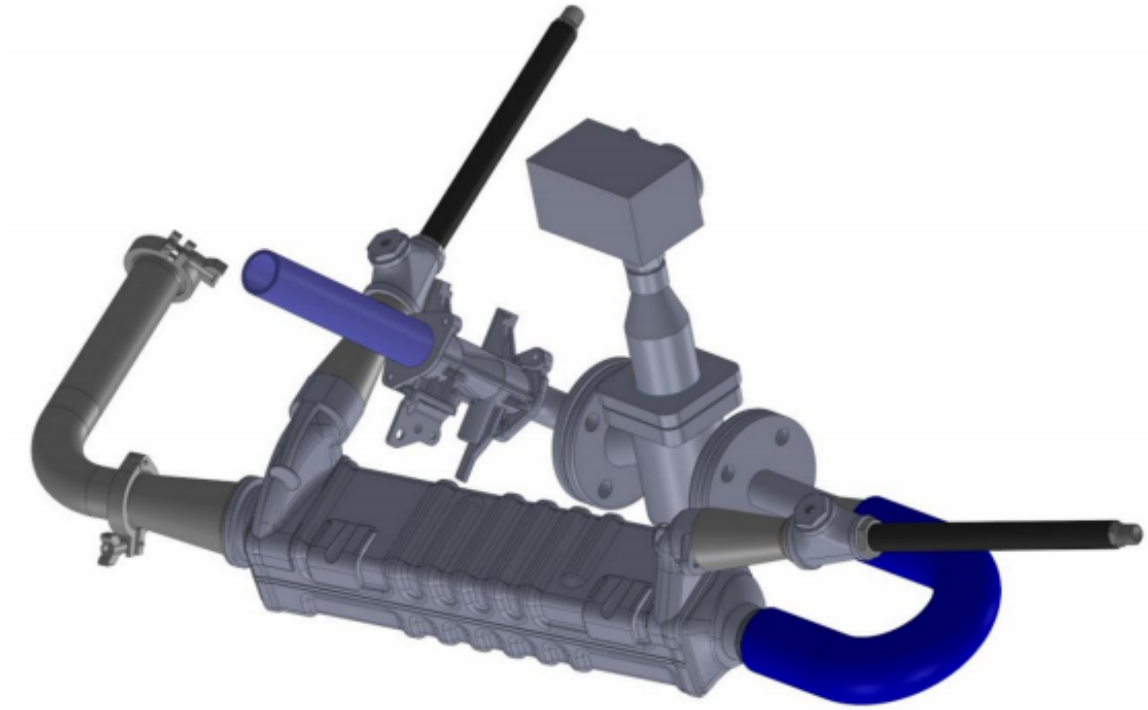

Figure 2.5: CAD model of the EGR system developed for this research engine [55].

2.1.4 Emissions Collection

A Horiba MEXA-ONE emissions bench was used to measure CO, CO_2, O_2, and NO_x. The EGR fraction is calculated from the ratio of CO_2 levels measured in the intake and exhaust streams using a dedicated, compact EGR CO_2 analyzer that sits closer to the engine, providing a more accurate EGR measurement. The measurement principle and range for each analyzer in the emissions bench is listed in Table 2.8.

Engine-out particulate emission trends were studied using filter smoke number (FSN) data obtained using an AVL 415S smoke meter. FSN is not a true measure of soot mass, it instead provides a measure of the change in reflectivity of a filter paper after a known sample of raw exhaust has passed through it [56]. However, the correlation between FSN and soot mass is known [56], thus FSN suffices to identify PM trends in diesel applications. The technical specifications of the smoke meter can be found in Table 2.9.

Table 2.8: Range of each analyzer in the Horiba MEXA-ONE emissions bench.

Analyzer	**Principle**	**Range**
CO	NDIR	0-50 to 0-5000 ppm
CO_2	NDIR	0-0.5 to 0-20 vol%
CO_2 (EGR)	NDIR (dry)	0-10 to 0-20 vol%
O_2	NDIR	0-1 to 0-25 vol%
THC	Heated FID	0-50 to 0-60000 ppmC
CH_4	Heated FID	0-50 to 0-5000 ppm
NO	Dual heated-CLD	0-10 to 0-10000 ppm
NO_x	Dual heated-CLD	0-10 to 0-10000 ppm
NO_2	Dual heated-CLD	Measured by dual detector

Table 2.9: Technical specifications of the AVL 415S smoke meter.

Parameter	**Value**
Resolution	0.001 FSN
Lower detection limit	0.002 FSN
Measurement range	0-10 FSN
Maximum exhaust temperature	600°C
Repeatability	$\sigma \leq \pm$ (0.005 FSN + 3% of MV @ 10s intake time)

2.1.5 Indicating System

An AVL Indimaster and Indicom indicating system was used as the data acquisition hardware and software, respectively. The cylinder pressure data was obtained at a resolution of 0.1 crank angle degree (CAD) using an AVL GH14P pressure sensor and sleeve, Kistler Type 5010B charge amplifier, and an AVL 416 crank angle encoder. Figure 2.6 shows the location of the pressure sensor on the fire deck. Relevant technical specifications for the pressure sensor are listed in Table 2.10.

The phasing of the pressure trace does not match that of the actual piston travel due to heat losses during compression [57], i.e. the timing of peak cylinder pressure for a motoring case will not coincide with the piston being at top dead center. The thermodynamic loss angle is an important parameter used in indicating systems to

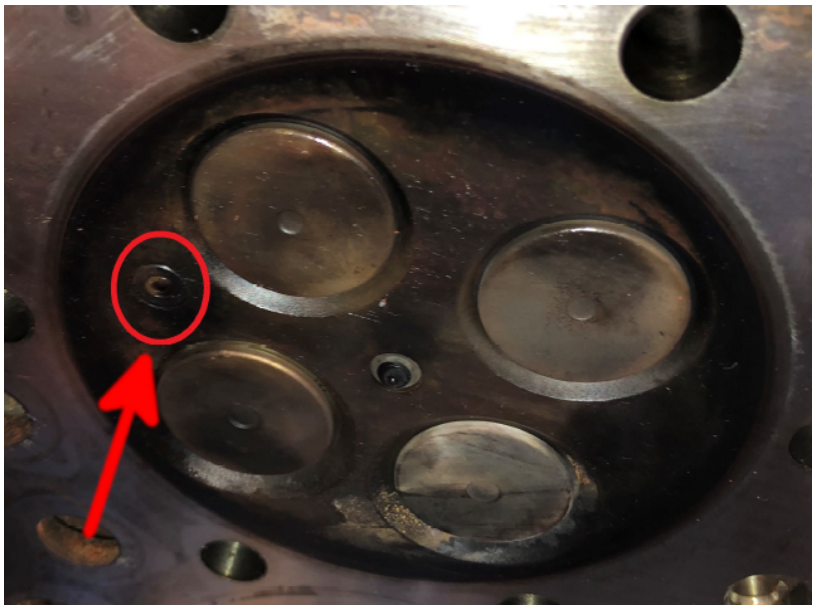

Figure 2.6: Location of the AVL GH14P pressure sensor used to obtain in-cylinder pressure data.

Table 2.10: Technical specifications of the AVL GH14P pressure transducer.

Parameter	**Value**
Measuring range	0-250 bar
Sensitivity	15 pC/bar nominal
Linearity	$\leq \pm 0.3\%$
Insulation resistance	$10^{13}\ \Omega$
Operating temperature range	-40 - 400°C
Cyclic temperature drift	$\leq \pm 0.5$ bar

adjust cylinder pressure derived top-dead-center (TDC) timings to match the physical TDC timing [58]. The difference in heat transfer characteristics of the TBC pistons could affect the thermodynamic loss angle, skewing the indicated measurements. As such, rather than using the same thermodynamic loss angle for each piston, an AVL 428 TDC sensor was utilized after the installation of every new piston to physically determine the crank angle timing for TDC and ensure the accuracy of indicated measurements between piston studies.

2.2 Data Collection Procedure

The data collection at each test point adhered to the following procedure:

- The engine was brought to a steady state at the desired operating condition, as indicated by flat, unchanging trends in the exhaust temperature, EGR fraction, and intake manifold temperature.
- High-speed synchronous data (i.e. the cyclic pressure trace) was collected in consecutive 200-cycle samples at a resolution of 0.1 CAD. CoV for the cylinder pressure traces reported was always ¡1%.
- Low-speed data, i.e. the various temperatures and pressures measured on the engine and fuel mass flow rate, was sampled at 4 Hz and reported as the time average over a 30-second collection period during each of the 200-cycle events above.
- Gas emissions measurements with the Horiba Mexa-ONE emissions bench were also sampled once per second over a 30-second period.

Additionally, an 8 hour break-in procedure was conducted for each new piston before collecting any experimental data. The break-in procedure ensured the new piston rings seated properly with the cylinder liner.

2.3 Experimental Data Analysis

The 200-cycle cylinder pressure data obtained with the aforementioned procedure were used to create an ensemble-averaged pressure trace which is then smoothed at a 2 kHz cutoff frequency to remove high-frequency fluctuations without modifying fundamental features. The processed pressure trace was then utilized to calculate the apparent rate of heat release, without considering heat exchange to the combustion chamber, using the zero-dimensional single-zone model shown in Equation 2.1 [24].

$$\frac{dQ_{\text{net}}}{dt} = p\frac{dV}{dt} + \frac{dU}{dt} \tag{2.1}$$

To obtain a better estimate of the heat release behavior, an in-house heat release analysis code [59, 60] was utilized to more precisely estimate the actual rate of heat release, taking heat transfer losses into account.

NO_x formation is directly influenced by combustion flame temperatures, the duration and timing of the peak combustion temps, and the oxygen content in the cylinder [61]. As such, bulk cylinder average gas temperature is calculated using the pressure trace data to be used as a tool for characterizing NO_x and heat transfer behavior during combustion. The bulk cylinder average gas temperature of the mixture was estimated in this study using the ideal gas equation of state as shown in Equation 5.7.

$$T_{\text{bulk}} = \frac{PV}{mR} \tag{2.2}$$

where P and V are the instantaneous cylinder pressure and volume, respectively, m is the total in-cylinder mass, and R is the specific gas constant. The total in-cylinder mass was estimated at intake valve closing timing by summing up the masses of air, external EGR and residual gas. The residual gas mass was estimated using the equation of state for an ideal gas at exhaust valve closing timing. The residual gas fraction was $\sim$ 3% for all cases studied, thus its effect on the trends presented is negligible.

Mean effective pressures (MEP) are used throughout the analysis of the results to quantify the various pathways taken by fuel energy during each combustion event [62]. Fuel mean effective pressure (FuelMEP) is the amount of fuel energy input to the engine per combustion event. It was calculated as shown in Equation 2.3.

$$\text{FuelMEP} = \frac{2\dot{m}_f Q_{LHV}}{NV_D} \tag{2.3}$$

where $\dot{m}_f$ is the fuel mass flow rate, Q_{LHV} is the lower heating value of the fuel and N is the rotational speed of the engine's crankshaft. The exhaust mean effective pressure (EXMEP) represents the energy lost to the exhaust stream and was calculated as shown in Equation 2.4.

$$\text{EXMEP} = \frac{mc_p(T_{\text{exh}} - T_{\text{amb}})}{V_D} \tag{2.4}$$

where m is the mass of the products, c_p is the heat capacity at constant pressure, T_{exh} is the exhaust temperature, T_{amb} is the ambient temperature and V_D is the displacement of the engine cylinder. A Chen-Flynn friction model, shown in Equation 2.5, was used to estimate the friction mean effective pressure to predict six-cylinder engine behavior on a brake basis.

$$\text{FMEP} = C_1 + (C_2 * P_{\text{cyl,max}}) - (C_3 * \bar{S_p}) + (C_4 * \bar{S_p}^2) \tag{2.5}$$

where C_1-C_4 are constants determined from experimental data obtained using the same engine configuration as our research engine operated in a six-cylinder mode, $P_{cyl,max}$ is the peak cylinder pressure and $\bar{S_p}$ is the mean piston speed.

The brake torque measured by the dynamometer does not correspond to the brake torque expected in a six cylinder configuration because only one cylinder is active. Therefore, BMEP was calculated by subtracting the Chen-Flynn friction from the nIMEP, as in Equation 2.6.

$$\text{BMEP} = \text{nIMEP} - \text{FMEP} \tag{2.6}$$

where nIMEP is the net indicated mean effective pressure. nIMEP is defined as the integral of cylinder pressure with respect to cylinder volume from the bottom dead center position of the compression stroke to BDC of the expansion stroke.

Heat transfer mean effective pressure (HTMEP) indicates how much energy is lost to the engine coolant. It was calculated indirectly by subtracting the exhaust and pumping losses and net indicated work from the fuel energy input as shown in Equation 2.7. This approach was compared and validated against a Hohenberg heat transfer model [63].

$$\text{HTMEP} = \text{FuelMEP} - \text{EXMEP} - \text{PMEP} - \text{nIMEP} \tag{2.7}$$

where PMEP is the pumping mean effective pressure. PMEP is defined as the integral of cylinder pressure with respect to cylinder volume from the bottom dead center position of the exhaust stroke to BDC of the intake stroke.

Gas exchange efficiency (η_{GE}) serves as a measure of the efficiency of the breathing process, relating the work lost in the exhaust stroke expelling burned gas and in the intake stroke inducting fresh to that of the total work over the entire engine cycle. It was calculated as shown in Equation 2.8.

$$\eta_{\text{GE}} = \frac{\text{nIMEP}}{\text{nIMEP} + \text{PMEP}} \tag{2.8}$$

2.3.1 Uncertainty Analysis

Error bars, with heights corresponding to a 95% confidence interval, are calculated when reporting indicated specific fuel consumption data as well as select filter smoke number and NO_x emission data. The methods used to establish the error bounds for each measurement are outlined in Appendix A.

CHAPTER III

Leveraging Piston Crown Coatings to Improve Combustion Characteristics, Emissions and Efficiency in Heavy-Duty Diesel Engines

The experimental studies outlined in Chapter I focus on single scenarios, such as high load operation, when testing multiple TBC pistons, failing to present a complete understanding of TBCs across a broad range of operating conditions. Studies encompassing a wide range of operating conditions conversely focus on a single TBC technology. Somhorst et al. [64, 65] has analyzed the effects of several TBC technologies and surface roughnesses on engine efficiency and heat losses at multiple operating conditions, however these studies are conducted in a light-duty diesel engine. Given heavy-duty diesel engines operate under more extreme conditions (higher peak cylinder pressures, pressure rise rates, aggressive combustion phasing, etc.), light-duty diesel TBC behavior may not be reflected in a heavy-duty diesel engine. This chapter aims to address gaps in the literature by comparing the performance of three TBC pistons against that of a baseline wave piston across seven operating conditions in a single cylinder research engine. The presentation of the results is as follows: First, the effect of TBCs on heavy-duty engine efficiency and emissions is analyzed under low load conditions at two engine speeds. Second, these effects are analyzed under

medium load conditions at two engine speeds. Finally, these effects are studied under high load conditions at three engine speeds. The purpose of these comparisons is to explore the benefits and limitations of TBC technologies and identify the engine operating conditions best suited for TBC applications in heavy-duty diesel engines.

3.1 Operating Conditions

The data presented in this chapter was obtained at the seven operating conditions detailed in Table 3.1 with the wave piston detailed in Chapter II as well as three additional TBC pistons specified in Table 3.2. All "A" conditions represent low speed engine operation (1160 RPM), "B" conditions represent medium engine speed (1460 RPM), and "C" represents high speed operation (1760 RPM). The numbers 50, 75, and 100 represent the percentage of maximum rated power, i.e., A75 is a low speed test condition at 75% of the engine's maximum rated power. The spread of these seven operating points encompasses a broad range of the engine's speed-torque map.

The TBC A piston has a thermal barrier coating with a target thickness of 400 μm. The plasma-sprayed coating is based on ceria stabilized zirconia for its thermal properties and is adhered to the steel piston substrate with a passive layer of nickel based alloy bond material. The fabrication process of this thermal coating adds material to the piston surface, thus material is skimmed off of the piston crown prior to the addition of the TBC. The wave bowl geometry complicates the skimming of the crown, thus the compression ratio may have changed.

The TBC B and TBC C pistons have thermal barrier coatings with target thicknesses of 35 μm and 70 μm, respectively. They are fabricated with the same plasma electrolytic aluminating (PEA) methodology that first grows a hercynite ($FeAl_2O_4$) layer and then an alumina (αAl_2O_3) layer into the existing crystal structure of the wave piston's crown [66]. The hercynite layer is a passive layer as its sole purpose

Table 3.1: Operating conditions for 7 minimap points.

	A50	**A75**	**A100**	**B50**	**B75**	**B100**	**C100**
Engine speed [RPM]	1160	1160	1160	1460	1460	1460	1760
Engine load (nIMEP) [bar]	11.9	17.6	23.7	11.2	16.4	21.5	18.5
Intake manifold absolute pressure [kPa]	197	261	324	219	280	320	300
EGR fraction (Y_{EGR}) [%]	21.1	20.0	15.7	21.8	22.8	17.1	15.8
Fuel rail pressure [bar]	1143	1253	1165	1642	1700	1749	2276
Start of injection timing [°aTDC]	-7.0	-6.7	-5.4	-5.4	-8.5	-6.2	-8.3

	All
Engine coolant temperature [°C]	90
Intake plenum temperature [°C]	35
Intake valve opening timing [°aTDC]	350 @0.35 mm lift
Intake valve closing timing [°aTDC]	-164 @0.35 mm lift
Exhaust valve opening timing [°aTDC]	154 @0.35 mm lift
Exhaust valve closing timing [°aTDC]	354 @0.35 mm lift

is to bond the thermal alumina layer to the piston. The PEA fabrication method conserves the geometric compression ratio of these pistons. The comparisons made between TBC B and TBC C will reflect the influence of coating thickness on fuel conversion efficiency, NO_x, and PM emissions.

The thermal properties of the TBC pistons were deliberately engineered to have exceptional "temperature swing" characteristics, whereby the surface temperature of the TBC follows that of the transient gas. The dynamic effect of surface temperature swing is what positively impacts thermal efficiency, not simply a general insulation and reduction of the cumulative heat loss over the entire cycle [17], especially given

Table 3.2: TBC piston properties.

	TBC A	**TBC B**	**TBC C**
Thermal layer composition	Ceria stabilized zirconia	Alumina (αAl_2O_3)	Alumina (αAl_2O_3)
Passive layer composition	Nickel based alloy	Hercynite ($FeAl_2O_4$)	Hercynite ($FeAl_2O_4$)
Total coating thickness [μm]	400	35	70
Thermal conductivity [W/m K]	0.8	0.5	0.5
Geometric compression ratio [-]	16.74	16.74	16.74

elevated wall temperatures during the intake stroke will reduce volumetric efficiency.

At the time of the writing, the density, thermal diffusivity, and specific heat capacity of these coatings were withheld due to the proprietary nature of these materials. Readers seeking more information on TBC B or TBC C can refer to Zhao et al. [66].

3.2 Low Load Testing

The experiments performed in this section examine the effect of TBC pistons on the combustion process under low load conditions. All actuator settings were set as outlined in Table 3.1 for the A50 and B50 operating points, with fuel injection pulse width adjusted to match the nIMEP of each respective test condition.

Figure 3.1 displays cycle average results of 10 key engine performance metrics for the uncoated wave and the three TBC pistons at A50 and B50. Numerous trends were identified as the engine speed increased from 1160 RPM to 1460 RPM. Figure 3.1a shows the relative change in indicated specific fuel consumption compared to the baseline uncoated wave piston at each low load operating condition. TBC A displayed ISFC increases of 0.9% and 0.7% at A50 and B50, respectively. TBC B and C had

similar ISFC results, with statistically insignificant changes at both A50 and B50.

Figure 3.1b shows that the TBC A piston negligibly affected the mass air flow through the engine, thus demonstrating acceptable temperature swing behavior at these low load conditions. TBC B however, shows a decline in volumetric efficiency at low speed with an improvement at the higher engine speed. The TBC C piston also reduced mass air flow through the engine at A50, but increasing engine speed did not improve volumetric efficiency at B50. The richer charge composition of the TBC A cases shown in Figure 3.1c are due to increased fuel consumption, while any decrease in air-fuel ratio for TBC B or C is due to poorer volumetric efficiency, a known impairment of TBC applications [8].

Figure 3.1f shows the relative change in indicated specific NO_x emissions compared to the baseline piston at the low load operating conditions. TBC A reduced NO_x emissions by 6% and 4% at A50 and B50, respectively. The improved NO_x emissions for TBC A are due to the combination of richer operation and lower peak cylinder pressures, as shown in Figure 3.1e. TBC B negligibly impacted NO_x emissions at A50 and increased them by 6% at B50. The rich charge composition of the TBC C piston improves NO_x emissions by 16% and 17% at A50 and B50, respectively. TBC B emits more NO_x emissions than TBC C given elevated intake manifold temperatures, as shown in Figure 3.1h, have a detrimental effect on NO_x emissions [67]. The higher intake manifold temperatures are a product of hotter ambient test cell conditions from summer operation for TBC B versus winter operation for all other cases.

Deteriorated fuel consumption for TBC A is caused by the delayed combustion phasing shown in Figure 3.1d and the increase in overall combustion duration shown in Figure 3.1i. While TBC B and C do not affect combustion phasing, they do have differing influence on the overall combustion duration. TBC C, the thicker of these two coatings, extends combustion duration while TBC B advances it slightly. Powell et al. [68] has also demonstrated that TBC advances combustion phasing relative to

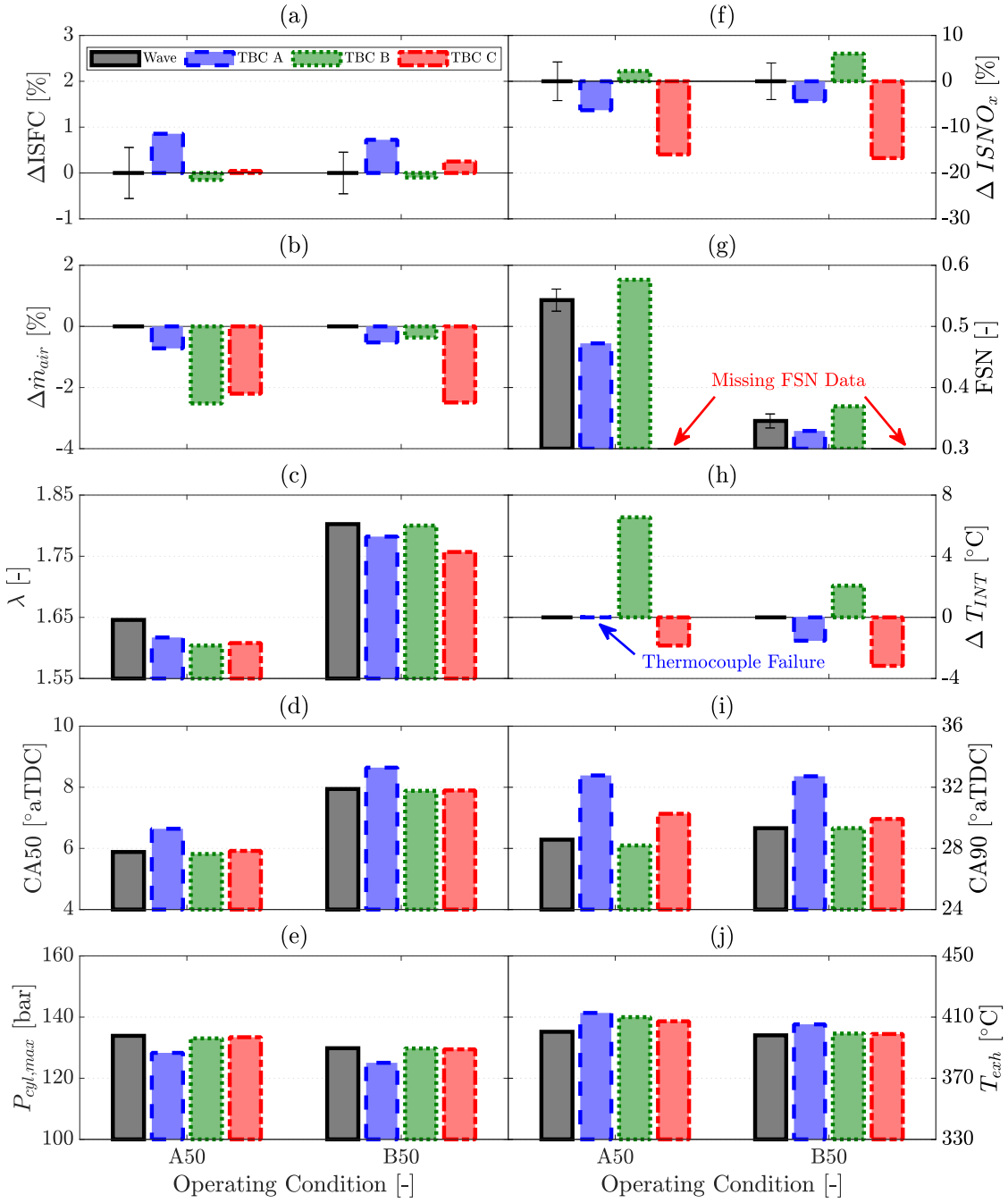

Figure 3.1: Cycle average results of 10 key engine performance metrics for the uncoated wave and the three TBC pistons at A50 and B50. (a) Relative change in ISFC compared to the uncoated wave piston (ΔISFC), (b) mass air flow ($\dot{m}_{air}$), (c) air-to-fuel equivalence ratio (λ), (d) timing of CA50, (e) peak cylinder pressure ($P_{cyl,max}$), (f) relative change in indicated specific NO_x emissions compared to the uncoated case ($\Delta ISNO_x$), (g) filter smoke number (FSN), (h) change in intake manifold temperature relative to the uncoated case (ΔT_{INT}), (i) timing of CA90 and (l) exhaust temperature (T_{exh}).

their metal engine counterpart given fixed operating conditions.

Figure 3.1g shows the filter smoke data for the uncoated, TBC A, and TBC B pistons. TBC C is missing PM data. TBC A reduced PM emissions while TBC B increased PM emissions at all low load conditions. Given the wave piston geometry is designed to promote soot oxidation late in the combustion process [50], the extended combustion duration of the two TBC A cases prolong the soot oxidation event and overcome the negative effect of reduced air-fuel ratio on PM emissions. The combustion duration of the TBC B case is similar to that of the uncoated piston, thus the richer charge composition of the TBC B case increases PM emissions at A50. Though TBC studies have shown contrasting PM emissions behavior [16, 69, 70], TBCs tend to decrease PM emissions if volumetric efficiency penalties are counteracted by a sufficient increase in combustion gas temperatures [5, 6, 71, 72], which TBC B fails to achieve at A50. At B50, TBC B operates at a similar air-fuel ratio and combustion duration as the uncoated piston, resulting in similar PM emissions.

While TBC A demonstrates the largest relative increase in exhaust temperatures in Figure 3.1j, only TBC B and C elevate exhaust temperatures without impacting ISFC at the low load-low speed condition. TBC C fails to increase exhaust temperatures over the TBC B piston despite its thicker thermal barrier layer.

Figure 3.2a shows that TBC A decreases the magnitude of the diffusion burn portion of the heat release and increases that of the premixed portion, the latter stemming from the lower cylinder pressures of TBC A shown in Figure 3.1e. TBC B and C do not affect the heat release rates compared to the uncoated piston. Figure 3.2b shows the bulk cylinder temperature during combustion for the uncoated and TBC pistons at the A50 and B50 conditions.

No TBC piston demonstrated a net heat transfer improvement despite altering characteristics that define the heat transfer gradient during combustion, failing to meet the promise of this low heat rejection technology [8]. The low combustion tem-

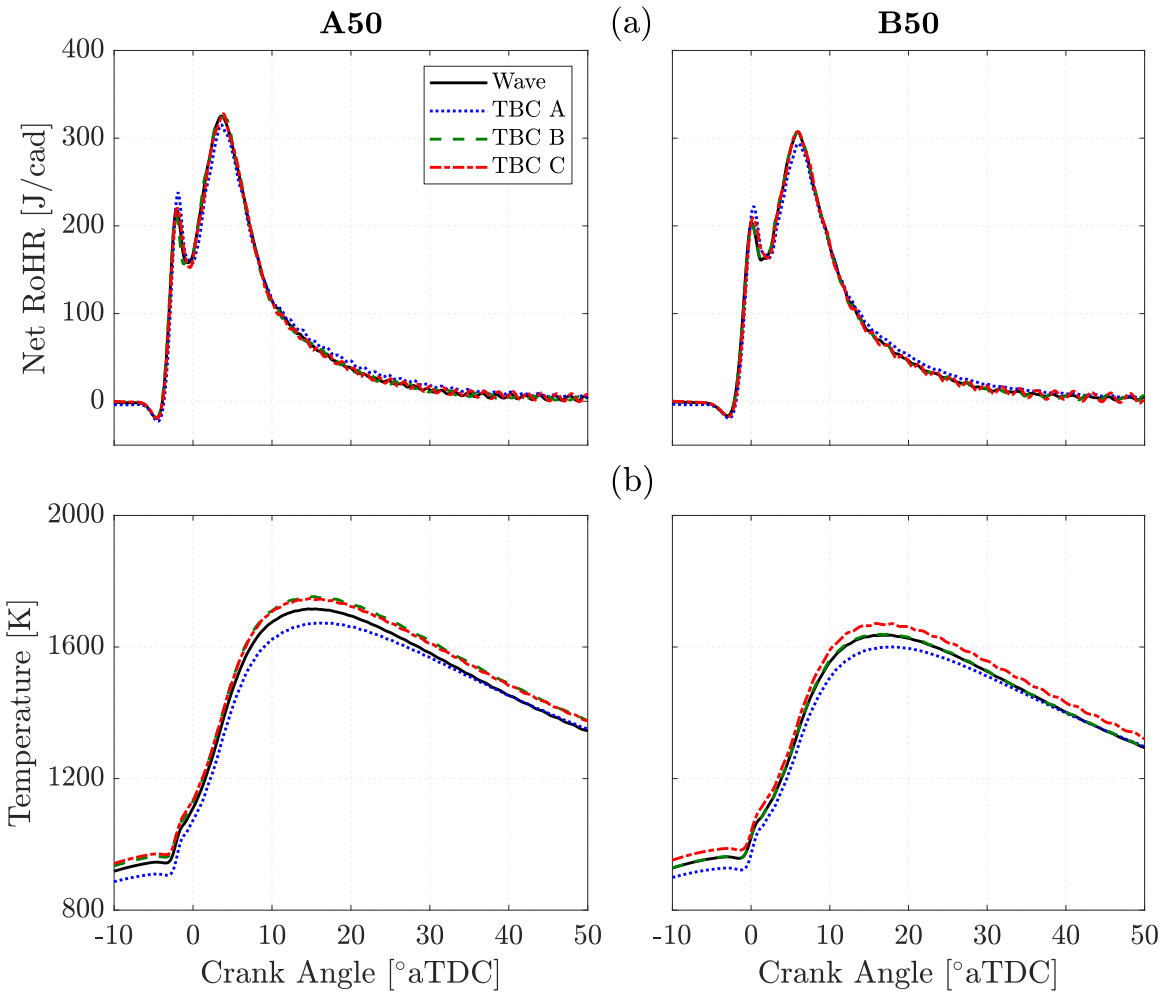

Figure 3.2: (a) The net rate of heat release and (b) bulk cylinder temperature for the uncoated and three TBC pistons at the A50 and B50 operating points.

peratures obtained with TBC A should decrease heat transfer losses, however, the prolonged combustion duration at both operating points resulted in increased ISFC instead. Both the TBC B and C pistons increased the heat transfer gradient at A50 by elevating combustion temperatures, a product of decreased cylinder dilution. However, the TBC C case has a higher propensity to transfer heat from the combustion gasses to the combustion chamber due to its longer combustion duration. The improved volumetric efficiency of the TBC B piston at B50 maintained combustion temperature parity with the uncoated piston while the thicker TBC C increased combustion temperatures, and thus increased the heat transfer gradient. The differences

in heat transfer behavior between TBC B and C at both low load conditions proved insignificant to fuel conversion efficiency.

Considering the improved NO_x emissions, increased ISFC, and decreased peak cylinder pressures across the low load operating conditions, it is concluded that TBC A had excessive material removed from the crown surface prior to the addition of the thermal barrier layer. Thus, the geometric compression ratio for this piston was not conserved and is lower than that of the three other pistons.

3.3 Medium Load Testing

The experiments performed in this section examine the effect of TBC pistons on the combustion process under medium load conditions. All actuator settings were set as outlined in Table 3.1 for the A75 and B75 operating points, with fuel injection pulse width adjusted to match the nIMEP of the respective test condition. TBC A is still considered in this section despite having a lower geometric compression ratio.

Figure 3.3 displays cycle average results of 10 key engine performance metrics for the uncoated wave and the three TBC pistons at A75 and B75. As the engine speed shifted from 1160 RPM to 1460 RPM, a number of trends were identified. Figure 3.3a shows the relative change in ISFC compared to the uncoated baseline wave piston at each medium load operating condition. As expected, TBC A displayed the largest increase in ISFC with penalties of 1.2% and 1.3% at A75 and B75, respectively. The TBC C piston increased ISFC by 0.6% at both A75 and B75. TBC B improved ISFC by 0.2% at A75 and increased ISFC by 0.4% at B75, both statistically insignificant.

Figure 3.3b shows that the TBC B piston reduced mass air flow through the engine more significantly at these medium load conditions than at the low load counterparts. The dependence on engine speed is now inverted, with higher engine speeds deteriorating volumetric efficiency. The negative impact the TBC C piston has on volumetric efficiency is the same as at the low load conditions. TBC A continues to

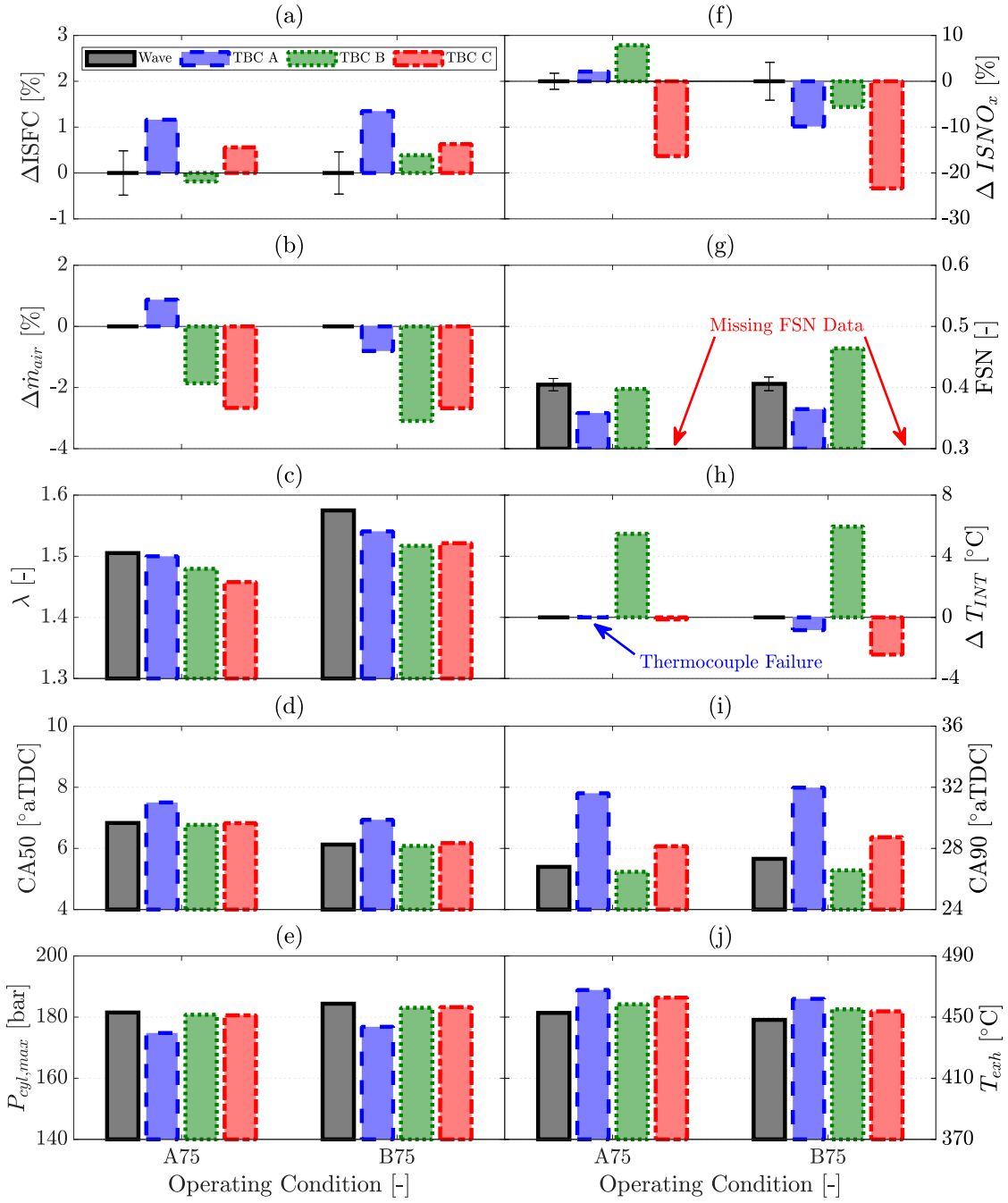

Figure 3.3: Cycle average results of 10 key engine performance metrics for the uncoated wave and the three TBC pistons at A75 and B75. (a) Relative change in ISFC compared to the uncoated wave piston (ΔISFC), (b) mass air flow ($\dot{m}_{air}$), (c) air-to-fuel equivalence ratio (λ), (d) timing of CA50, (e) peak cylinder pressure ($P_{cyl,max}$), (f) relative change in indicated specific NO_x emissions compared to the uncoated case ($\Delta ISNO_x$), (g) filter smoke number (FSN), (h) change in intake manifold temperature relative to the uncoated case (ΔT_{INT}), (i) timing of CA90 and (l) exhaust temperature (T_{exh}).

demonstrate adequate temperature swing behavior at these medium load conditions. The combination of decreased volumetric efficiency and increased fuel consumption result in all of the TBC pistons once again operating under richer charge conditions than the uncoated piston as shown in Figure 3.3c.

Figure 3.3f shows the relative change in indicated specific NO_x emissions compared to the baseline piston at the A75 and B75 operating conditions. The increase in intake temperatures with TBC B presented in Figure 3.3h are again responsible for the superior NO_x emissions performance of TBC C. TBC C improves NO_x emissions by 16% and 23% at A75 and B75, respectively, compared to an 8% penalty and 6% improvement obtained with TBC B. TBC A negligibly impacted NO_x emissions at A75 and decreased NO_x emissions by 10% at B75.

TBC B and C again demonstrate minimal impact on combustion phasing, as shown in Figure 3.3d. The coating thickness again determines the effect each piston has on overall combustion duration, shown in Figure 3.3i, with TBC C extending combustion duration and TBC B accelerating it. The ISFC trends for these two pistons emphasize the importance combustion phasing and duration has on efficiency at these medium loads. The increased fuel consumption for TBC A is caused by the delayed combustion phasing and the increase in overall combustion duration related to the suspected geometric compression ratio reduction, as supported by the peak cylinder pressure trends of Figure 3.3e.

Figure 3.3g shows the filter smoke data for the uncoated, TBC A, and TBC B pistons. TBC A reduces PM emissions at both operating conditions given lower compression ratios improve in-cylinder mixing conditions compared to higher compression ratio counterparts with reduced chamber volume ratios [47] and set-off lengths [48]. While the richer charge of TBC B doesn't impact PM emissions at the A75 condition, it increases PM emissions at B75, indicating that elevated engine speeds hinder the wave piston's impact on soot oxidation late in the combustion process. Figure 3.3j

shows similar exhaust temperature trends as at the low load operating conditions.

Figure 3.4a shows that heat release behavior is as before, with TBC A reducing and delaying the diffusion burn while TBC B and C produce no significant effect on the heat release rates. Figure 3.4b shows that TBC B and C produce similar elevated combustion temperatures at both conditions despite their different coating thicknesses, while TBC A continues to produce the lowest combustion temperatures.

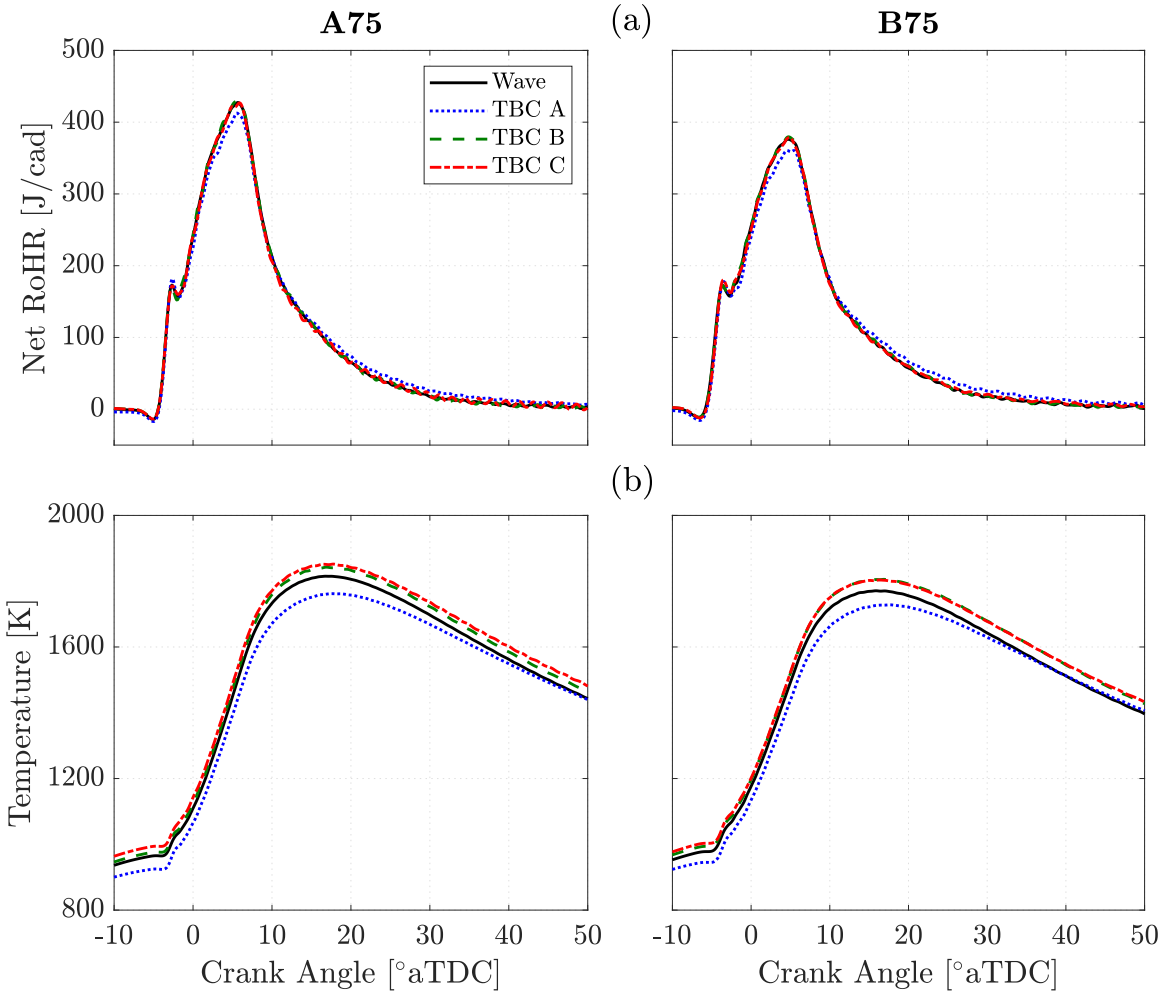

Figure 3.4: (a) The net rate of heat release and (b) bulk cylinder temperature for the uncoated and three TBC pistons at the A75 and B75 operating points.

The low combustion temperatures obtained with TBC A fail to improve ISFC due to the prolonged combustion duration caused by the reduced geometric compression ratio. TBC B increases the heat transfer gradient at A75 by elevating combustion

temperatures, but shortens combustion duration enough for the insulating coating to diminish heat transfer losses, as indicated by the improved ISFC. However, TBC B cannot mitigate the increased heat transfer losses at B75. Though the prolonged combustion duration and raised combustion temperatures of TBC C increase ISFC, the penalty from using this thicker coating does not increase with engine speed. The different effects TBC B and C have on heat transfer behavior are more significant to fuel conversion efficiency at these medium loads than at low loads.

3.4 High Load Testing

The experiments performed in this section examine the effect of TBC pistons on the combustion process under high load conditions. All actuator settings were set as outlined in Table 3.1 for the A100, B100, and C100 operating points, with fuel injection pulse width adjusted to match the nIMEP of the respective test condition. TBC A is still considered in this section despite its lower geometric compression ratio.

Figure 3.5 shows cycle average results of 10 key engine performance metrics for the uncoated wave and the three TBC pistons at each of the three high load engine operating conditions. As the operating conditions shifted to higher engine speeds, several trends were identified that differed from those presented under low and medium load conditions. Figure 3.5a shows the relative change in indicated specific fuel consumption compared to the baseline piston at each high load operating condition. As anticipated, TBC A displayed the worst ISFC across all conditions with increases of 1.3%, 2.1%, and 1.2% at A100, B100, and C100 respectively. Though TBC C had the next highest ISFC penalties, they were statistically insignificant. TBC B also had a statistically insignificant effect on fuel consumption across all test conditions.

Figure 3.5b shows that both the TBC A and B pistons negligibly affected the mass air flow through the engine, thus these coatings demonstrate good temperature swing behavior at these high load conditions. While TBC C still shows a 2% decrease

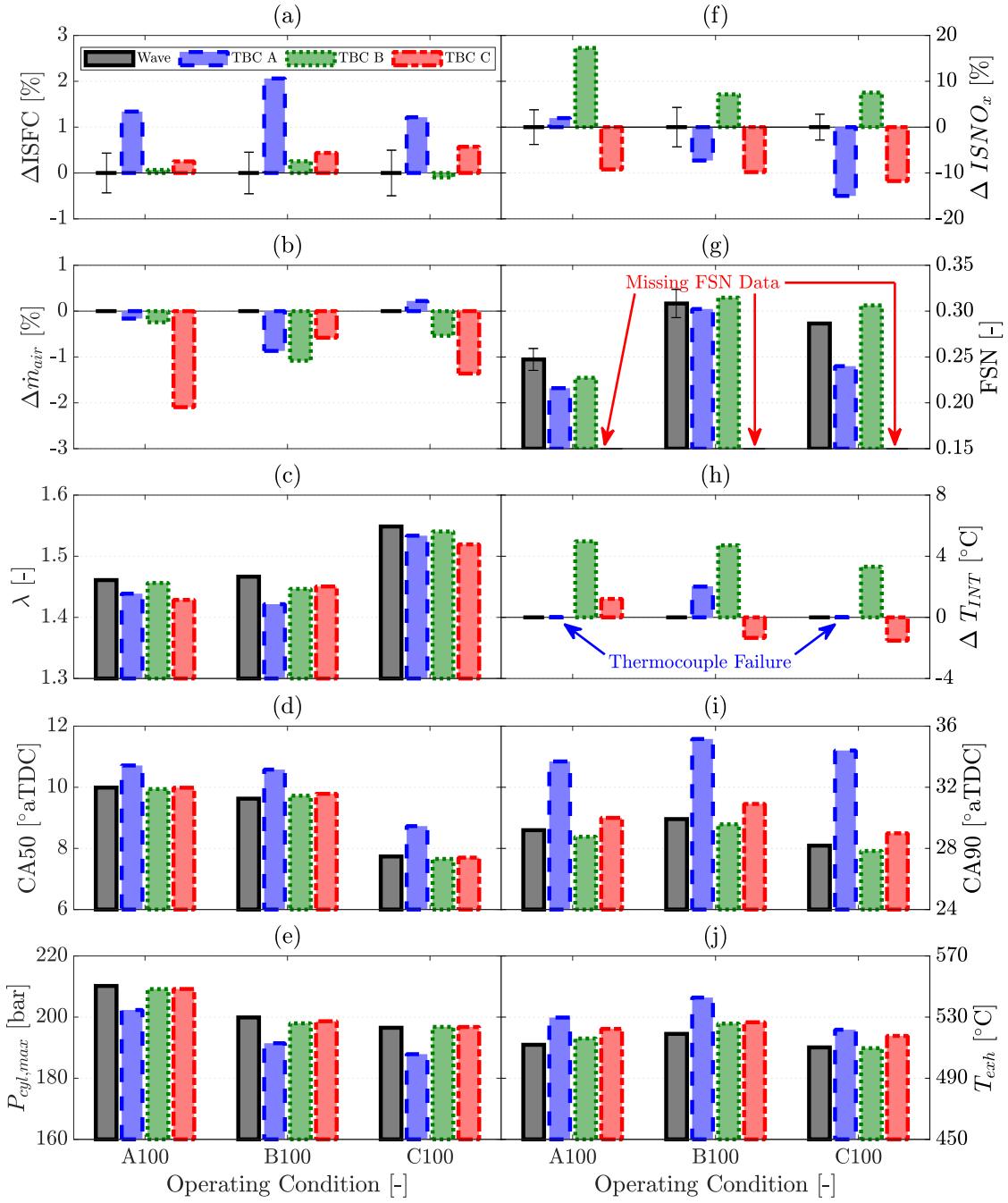

Figure 3.5: Cycle average results of 10 key engine performance metrics for the uncoated wave and the three TBC pistons at A100, B100 and C100. (a) Relative change in ISFC compared to the uncoated wave piston (ΔISFC), (b) mass air flow ($\dot{m}_{air}$), (c) air-to-fuel equivalence ratio (λ), (d) timing of CA50, (e) peak cylinder pressure ($P_{cyl,max}$), (f) relative change in indicated specific NO_x emissions compared to the uncoated case ($\Delta ISNO_x$), (g) filter smoke number (FSN), (h) change in intake manifold temperature relative to the uncoated case (ΔT_{INT}), (i) timing of CA90 and (l) exhaust temperature (T_{exh}).

in mass air flow at the A100 condition, increasing engine speed minimizes those volumetric efficiency penalties, contrary to medium load and low load behavior. The combination of decreased volumetric efficiency and increased fuel consumption result in all of the TBC pistons operating under richer charge conditions than the uncoated piston as shown in Figure 3.5c.

Figure 3.5f shows the relative change in indicated specific NO_x emissions compared to the baseline piston at each high load operating condition. TBC A negligibly impacted NO_x emissions at A100 and decreased NO_x emissions by 7% and 15% at B100 and C100, respectively. The increased intake temperatures shown in Figure 3.5h for TBC B are responsible for the 17%, 7%, and 8% increase in NO_x emissions. The increase in NO_x emissions at A100 for TBC B is exacerbated by a minimal decrease in air-fuel ratio, or preservation of in-cylinder O_2 availability. The superior NO_x behavior of TBC C, with 9%, 10%, and 12% improvements at these high load conditions, is attributed to lower intake manifold temperatures and richer charge composition.

Figure 3.5g confirms that increasing engine speed is detrimental to the wave bowl's ability to suppress increased PM emissions arising from the decreased volumetric efficiency of the TBC pistons. Specifically, the PM emissions with TBC B increase from below baseline levels to above baseline levels as engine speed increases from 1160 RPM to 1760 RPM. TBC A, again, improved PM across all operating conditions due to operation at a lower compression ratio given Figure 3.1e continues to display similar peak cylinder pressure trends as the previous sections.

Figure 3.5j shows that TBC C only increases exhaust temperatures over the TBC B piston when TBC C had a richer charge composition. TBC C again fails to demonstrate increased exhaust temperatures attributed solely to its thicker thermal barrier layer. TBC A demonstrates the largest increase in exhaust temperature, $\approx 20^{\circ}C$, as expected given the inefficiency of this piston at these high load conditions. The increased exhaust temperatures do not merit the increased fuel consumption considering

high exhaust temperatures are not difficult to maintain at high load operation.

Figure 3.5d and Figure 3.5i show the effect these TBC pistons have on combustion phasing and duration are unaffected by engine load or speed, as observed in the previous sections. Figure 3.6a shows TBC B and C continue to insignificantly affect heat release rates while TBC A decreases the magnitude and extends the duration of the diffusion burn portion of combustion as engine speed increases.

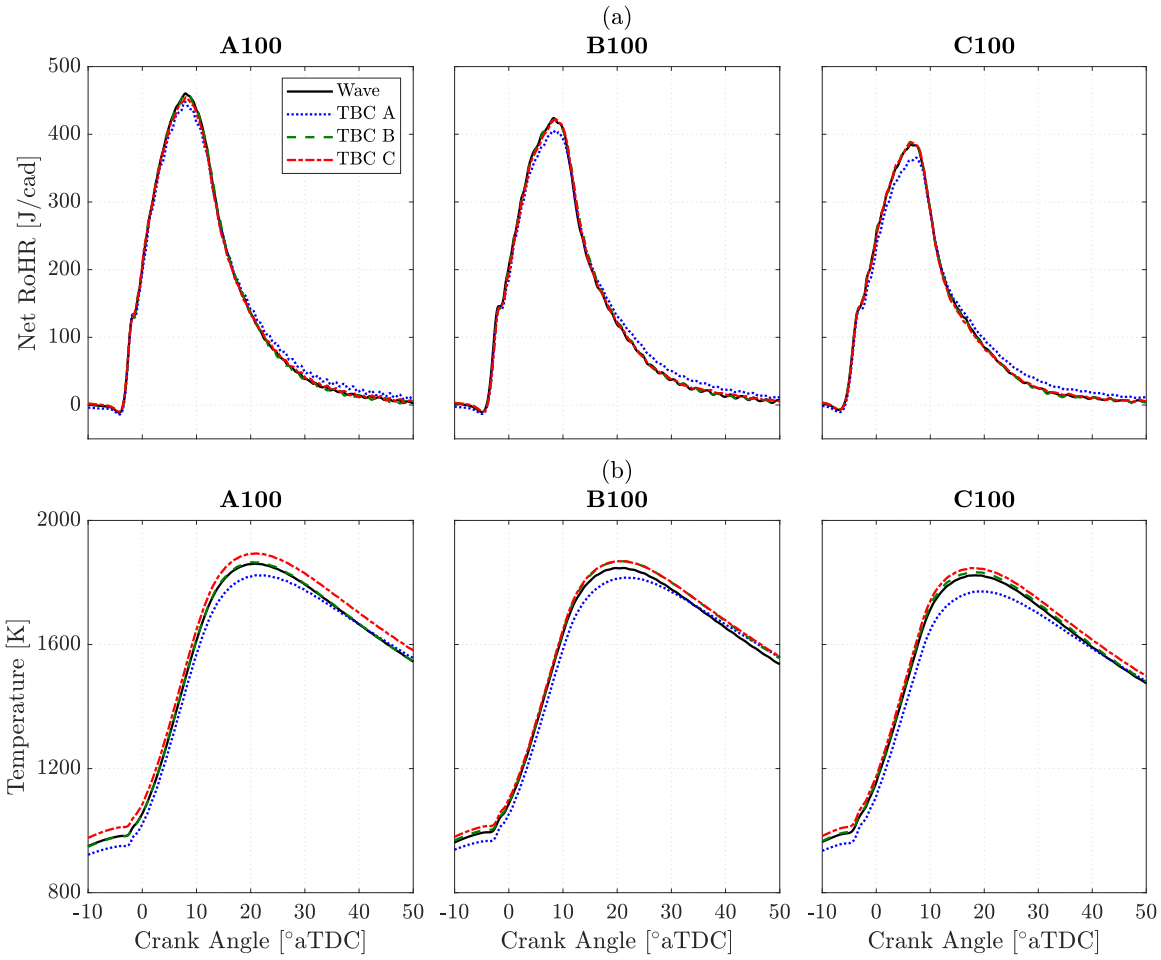

Figure 3.6: (a) The net rate of heat release and (b) bulk cylinder temperature for the uncoated and three TBC pistons at the A100, B100, and C100 operating points.

Figure 3.6b shows that at these high load conditions, cylinder dilution continues to play a vital role on dictating combustion temperatures. TBC B and C produce similar elevated combustion temperatures at B100 where air-fuel ratio is similar, and TBC B maintains combustion temperature parity with the uncoated piston at A100

where air-fuel ratio is similar. TBC A continues to produce the lowest combustion temperatures.

All TBC pistons fail to demonstrate a net heat transfer benefit despite altering characteristics that define the heat transfer gradient during combustion. The low combustion temperatures obtained with TBC A should decrease heat transfer losses, however, the prolonged combustion duration at all operating points result in increased ISFC instead.

TBC B does not significantly shorten combustion duration or alter combustion temperatures, thus conserving the heat transfer gradient at these high load conditions. TBC C both extends the combustion duration and increases combustion temperatures, increasing the heat transfer gradient. The insulating properties of TBC B are insufficient for improving ISFC, but prevent increased fuel consumption. The insulating properties of TBC C are insufficient for impeding increased heat transfer losses from deteriorating ISFC. The contrasting heat transfer behavior shown with TBC B and C are very significant to fuel conversion efficiency at high loads, proving inconsequential at low loads only.

3.5 Summary and Conclusions

This chapter presented an experimental investigation of the effect of coating the wave piston crown with a thermal layer on the combustion process, emissions, and thermal efficiency in a single cylinder heavy-duty research engine. Three TBCs of varying composition and thickness were utilized in this study. The experiments were carried out at seven operating conditions representative of a broad range of the engine's speed-torque map.

TBC performance was highly dependent on volumetric efficiency, which was determined by temperature swing characteristics, engine load, and engine speed. Cases with volumetric efficiency penalties increased the heat transfer gradient between the

combustion gasses and combustion chamber due to reduced cylinder dilution. The insulative properties of each TBC are what determine how each coating will respond to the aforementioned change in heat transfer gradient, and that variable response leads to the varying results on the impact TBCs have on fuel conversion efficiency found in this study, and others [11, 64].

Operation of the TBC pistons at low, medium, and high loads across different engine speeds yielded the following observations for the TBC B and C wave pistons in this study:

- At low load operation, the use of thermal barrier coated pistons had a neutral effect on indicated specific fuel consumption regardless of coating thickness or decreased volumetric efficiency.
- At medium and high load operation, decreasing volumetric efficiency creates heat transfer gradients strong enough to exceed the insulative capabilities of the thinner TBC piston.
  - The thinner TBC operates at ISFC parity with the baseline piston at all conditions with minimal volumetric efficiency reduction, as that keeps heat transfer gradient increases at a minimum. ISFC increased by 0.4% at the medium load-medium speed condition, where the decrease in volumetric efficiency is large.
  - The superior insulative properties of the thicker coating fails to prevent increased ISFC, up to 0.6%, because of extended combustion duration across all conditions.
- The impact the wave piston has on soot oxidation is diminished at higher engine speeds, with the lowest PM emission increases from the TBC pistons observed at the low speed conditions.

Further experiments should be conducted at engine operating conditions with higher combustion temperatures. The EGR requirement for each of the seven operating conditions tested is high, $Y_{EGR} > 15\%$ for NO_x control, and thus decreases peak combustion temperatures. If EGR rates were lower, and thus combustion temperatures higher, then the insulative properties of the TBC should minimize additional heat transfer losses compared to an uncoated piston, amplifying any thermal efficiency benefit. Work involving modulating EGR fraction with the intent of increasing combustion temperatures will be conducted in Chapter V. Adjusting EGR fraction will also serve to better understand the NO_x behavior of an insulated heavy-duty diesel engine.

The current work was completed using a single-cylinder engine, but behavior in an insulated multi-cylinder engine may be different due to the increased heat rejection to the intake manifold that could have a much more pronounced detriment to volumetric efficiency. In that same manner, increased heat rejection to the exhaust manifold may highlight an exhaust temperature benefit of TBC pistons that was downplayed in this study.

Additionally, TBC A should be remade with greater emphasis placed on conserving the geometric compression ratio of the piston. TBC A displayed the best temperature swing behavior during the intake stroke, but due to the poor fuel conversion efficiency caused by the reduced compression ratio, the impact of the temperature swing behavior during combustion is unknown. A retest of the revised piston would serve to identify the superior TBC technology among TBC A and TBC B as well as to further investigate the characteristics that produce the irregular volumetric efficiency behavior for each TBC piston across the seven operating conditions tested.

CHAPTER IV

Impact of Miller Cycle Strategies on Combustion Characteristics, Emissions and Efficiency in Heavy-Duty Diesel Engines

Previous work on the effectiveness of Miller cycle valve timings to improve the NO_x-efficiency tradeoff in heavy-duty engines has led to mixed, often contradicting, conclusions. Several studies outlined in Chapter I fail to isolate the effect of Miller cycle on the combustion process by allowing start of injection timing or intake manifold pressures to vary. This chapter tries to address these shortcomings by using well-controlled experiments on a single cylinder research engine to isolate the effect of Miller cycle strategies on the combustion process. The structure of the presentation of the results is as follows: First, the effect of EIVC/LIVC profiles on volumetric efficiency is analyzed under motoring conditions and compared to the changes in effective compression ratio. Second, the effect of Miller strategies on the combustion process is analyzed at constant intake manifold pressure. Third, Miller cycle performance is analyzed at constant air-fuel ratio to investigate how Miller profiles affect engine performance when the composition of the cylinder charge is conserved. Fourth, Miller cycle performance is analyzed as a function of overall turbocharger efficiency. This work was accepted for presentation at the Society of Automotive Engineers 2020

World Congress [73].

4.1 Operating Conditions

Table 4.1 outlines the baseline operating condition used to quantify the performance of all of the experimental cases. All engine output data is on an indicated basis due to the fact that this single cylinder engine motors the five deactivated cylinders. The baseline operating condition has a fixed EGR rate that leads to the baseline engine-out NO_x emissions of 4.5 g/kWh. For all conditions other than the baseline, NO_x was held constant by adjustment of EGR level.

Table 4.1: Engine operating parameters.

Parameter	**Value**
Engine speed	1160 RPM
Engine load (nIMEP)	1.76 MPa
Engine coolant temperature	90°C
Intake plenum temperature	35°C
Intake manifold absolute pressure	260 kPa
EGR fraction (Y_{EGR})	20%
Air-fuel ratio (λ)	1.5
Fuel rail pressure	125 MPa
Start of injection timing[1]	-6.7° aTDC
Indicated specific NO_x emissions	4.5 g/kWh
Intake valve opening timing	350° aTDC
Exhaust valve opening timing	154° aTDC
Exhaust valve closing timing	354° aTDC

Figure 4.1 shows the selected EIVC/LIVC valve profiles that were designed using the Lotus AVT system for operation in our single cylinder research engine. The middle curve indicates the baseline valve profile, while the left and right arrows point to the selected EIVC and LIVC profiles, respectively. Intake valve opening timing was kept constant across all cases.

[1] All timings referenced to combustion TDC. Valve timings @ 0.35 mm lift.

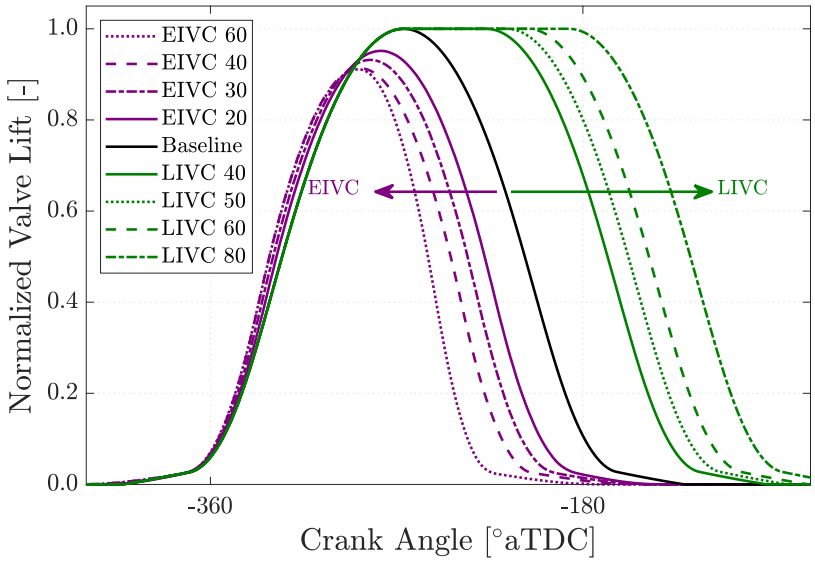

Figure 4.1: The EIVC and LIVC valve strategies used in this study range from IVC timings advanced up to 60 CAD to IVC timings delayed up to 80 CAD.

4.2 Effect of IVC Timing on Effective Compression Ratio and Volumetric Efficiency

EIVC and LIVC profiles were operated under motored conditions to quantify the effect of Miller cycle on volumetric efficiency. Engine speed was held constant at 1160 RPM. The variation in VE from the EIVC/LIVC strategies was compared to the changes in effective compression ratio (CR_{eff}). The geometric compression ratio (r_c) is one of the most important geometric parameters of a reciprocating engine. It is defined as

$$r_c = \frac{\text{maximum cylinder volume}}{\text{minimum cylinder volume}} = \frac{V_\text{d} + V_\text{c}}{V_\text{c}} \tag{4.1}$$

where V_d is the displaced volume and V_c is the clearance volume. Unlike the geometric compression ratio, CR_{eff} is defined as shown in Equation 4.2

$$CR_{\text{eff}} = \frac{V_{\text{IVC}}}{V_{\text{TDC}}} \tag{4.2}$$

where V_{TDC} is the cylinder volume at TDC and V_{IVC} is the cylinder volume at IVC timing. V_{TDC} is equivalent to V_{c} from Equation 4.1. CR_{eff} was computed using crank-slider kinematics and is strictly a function of the engine geometry and IVC timing. Normalized VE is utilized in this study, as shown in Equation 4.3

$$VE_i = \frac{\dot{m}_i}{\dot{m}_{\text{baseline}}} \tag{4.3}$$

where $\dot{m}_{\text{baseline}}$ is the air mass flow rate of the baseline condition and $\dot{m}_i$ is the air mass flow rate of the tested condition.

The experiments were carried out both under naturally aspirated and boosted motoring conditions to understand the effect of intake pressure boundary conditions on the VE reduction with Miller valve timing. This study yielded a similar outcome between naturally aspirated and boosted operation. As a result, only the boosted condition is shown in Figure 4.2, which matches the intake pressure of the baseline condition.

Figure 4.2 displays the effect of IVC timing on effective compression ratio and volumetric efficiency. The baseline IVC timing is highlighted using the grey dotted line, while bottom dead center (BDC) location is highlighted using the red dotted line. As expected, CR_{eff} is symmetric around bottom dead center. The baseline IVC timing corresponds to the maximum VE condition and is located approximately 20 CAD after bottom dead center. For similar shifts in IVC timing from the baseline timing, LIVC strategies result in a larger change in CR_{eff} compared to EIVC strategies. However, EIVC strategies are more effective at reducing VE compared to LIVC strategies.

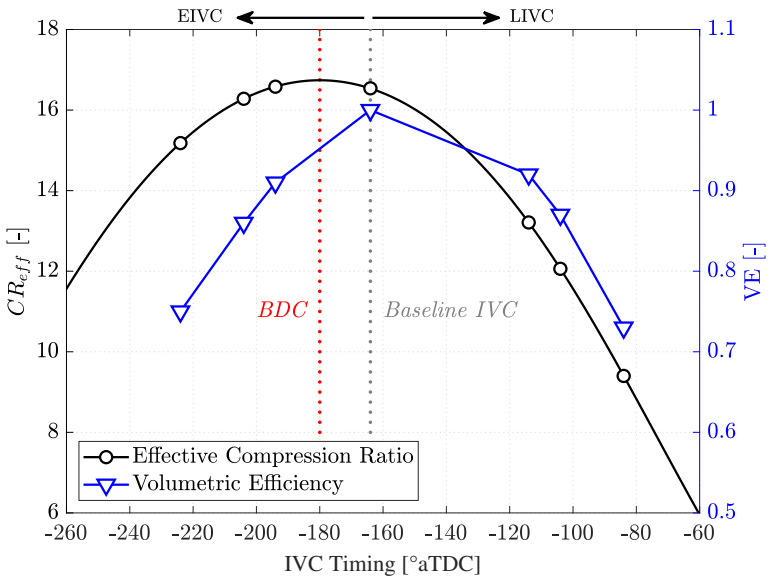

Figure 4.2: IVC timing influence on effective compression ratio and volumetric efficiency. Influence on effective compression ratio (black markers) is symmetric around BDC but volumetric efficiency (blue markers) is not. IVC timings of different effective compression ratios can have similar effect on volumetric efficiency.

This is attributed to EIVC strategies inhibiting flow inertia effects associated with IVC timing after BDC [24].

The triangle markers correspond to the VE of the baseline case and three pairs of EIVC and LIVC profiles of equivalent VE reduction. For example, for a normalized VE of approximately 0.75, IVC timing has to either be advanced by 60 CAD or retarded by 80 CAD from the baseline. Based on these findings, equivalent VE reduction profiles are used in the subsequent sections to compare the performance of EIVC and LIVC Miller strategies.

4.3 Miller Cycle at Constant Intake Pressure and NO_x

The experiments performed in this section investigate the effect of EIVC and LIVC profiles on the combustion process at the baseline intake manifold pressure condition of $P_{INT} = 260$ kPa. All actuator settings were set as outlined in Table 4.1, except for Y_{EGR}, end of injection timing and, naturally, the intake valve profile. Fuel injection

pulse width was adjusted to match the baseline load (net IMEP = 1.76 MPa) and Y_{EGR} was adjusted keep NO_x output at the baseline emission level (4.5 g/kWh). The load at the extreme IVC timings (-224° and -84°) was lower than the baseline value due to the inability to achieve stable engine operation at those conditions. This caused some changes in the experimental trends at the very extreme conditions.

Figure 4.3 displays cycle average results for the performance of each EIVC and LIVC case at constant P_{INT} as a function of IVC timing. The dotted grey line indicates the baseline IVC timing. Deviating from the baseline to the left or right indicates a more extreme EIVC or LIVC strategy, respectively. As the EIVC/LIVC strategy becomes more aggressive, a number of experimental trends can be identified.

As expected from Section 4.2, mass air flow through the engine decreases as IVC timing is moved away from the baseline timing. As a result of this VE reduction, air-fuel ratio decreases because the engine load is held constant across all cases. Peak cylinder pressures decrease as IVC timing deviates from the baseline case. For the EIVC cases the lower peak cylinder pressures are due to lower cylinder pressures at IVC rather than lower CR_{eff}. As the LIVC cases become more aggressive, cylinder pressures at IVC increase due to the piston compressing against a closing intake valve, but not enough to counteract the significant reduction of CR_{eff}.

Exhaust temperatures increase with more aggressive Miller profiles, which is likely due to the lower mass air flow through the cylinder and the associated effect of dilution on the gas temperature. Lower EGR levels are needed to obtain NO_x parity at this condition, but CO emissions increase dramatically as IVC deviates significantly from the baseline timing.

CA50 timing shows a slight delay as IVC deviates from the baseline timing, while CA90 timing is retarded more significantly. The pumping losses decrease with more extreme Miller timing primarily due to the lower EGR requirements under those conditions. Both net indicated and brake specific fuel consumption deteriorate sig-

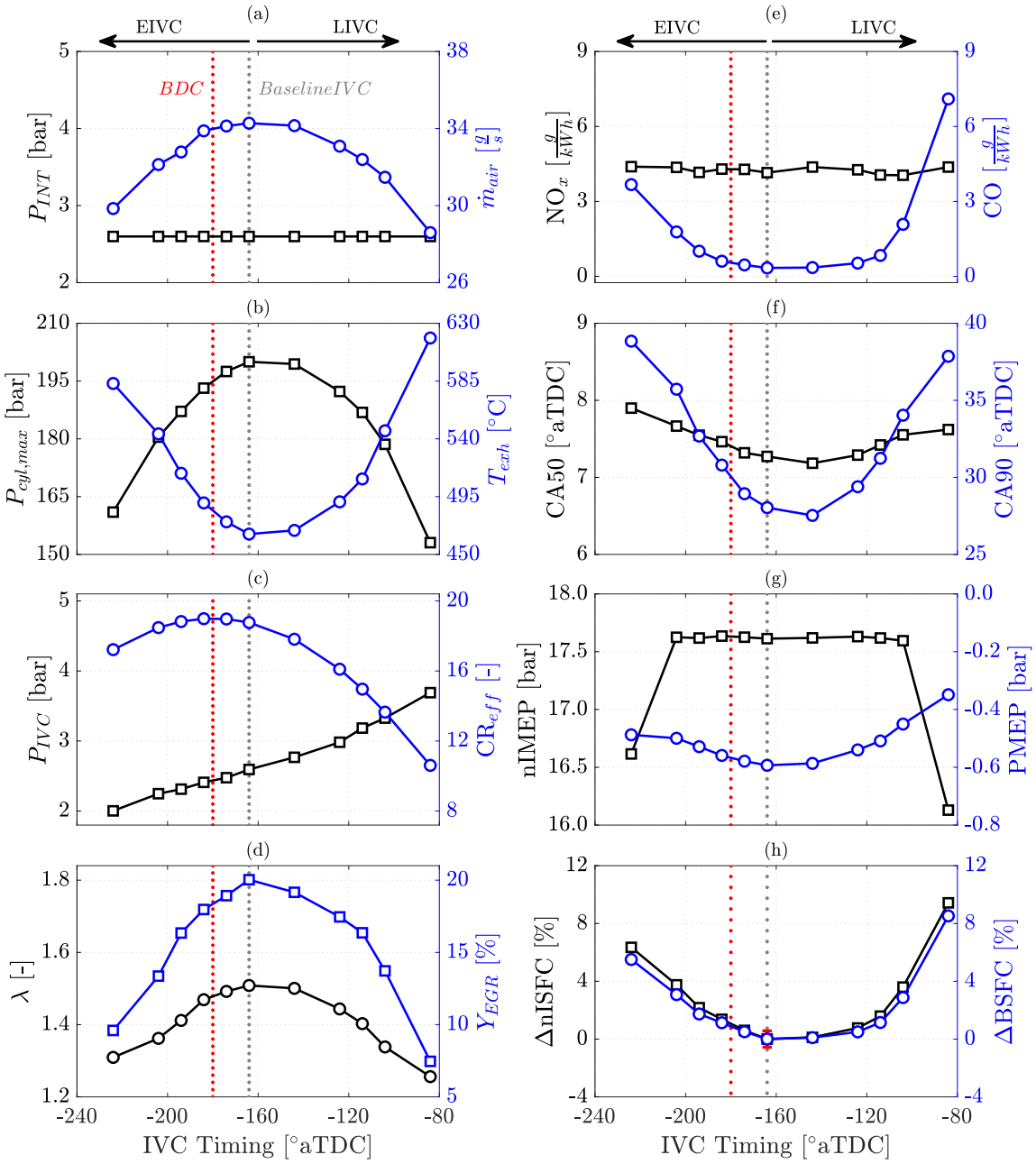

Figure 4.3: Engine performance based on IVC timing at constant intake manifold pressure and engine-out NO_x emission levels. The dotted grey line shows the baseline IVC timing while the dotted red line shows the BDC location. Square markers correspond to the left axis while circle markers correspond to the right axis. Cylinder pressure at IVC and effective compression ratio (a); intake pressure and mass air flow through the engine (b); peak cylinder pressure and exhaust temperature (c); air-fuel ratio and EGR mass fraction (d); indicated specific NO_x and CO engine-out emissions (e); timing of CA50 and CA90 (f); net indicated and pumping mean effective pressure (g); Relative change in ISFC and BSFC compared to the baseline (h).

nificantly as IVC timing deviates from the baseline timing. This is attributed to the unfavorable thermodynamic properties of the mixture associated with the lower dilution level as well as the slower burn rate late in the combustion process.

Figures 4.4a and 4.4b show the pressure traces for the EIVC and LIVC cases. The reduction of pumping losses shown in Figure 4.3g are reflected in the decrease in size of the pumping loop for the Miller cycle cases shown in Figure 4.4c. At constant boost pressure, unfavorable thermodynamic properties of the mixture associated with lower dilution, longer combustion duration and elevated combustion temperatures, as shown in Figure 4.5a and 4.5c, all contribute to increased fuel consumption.

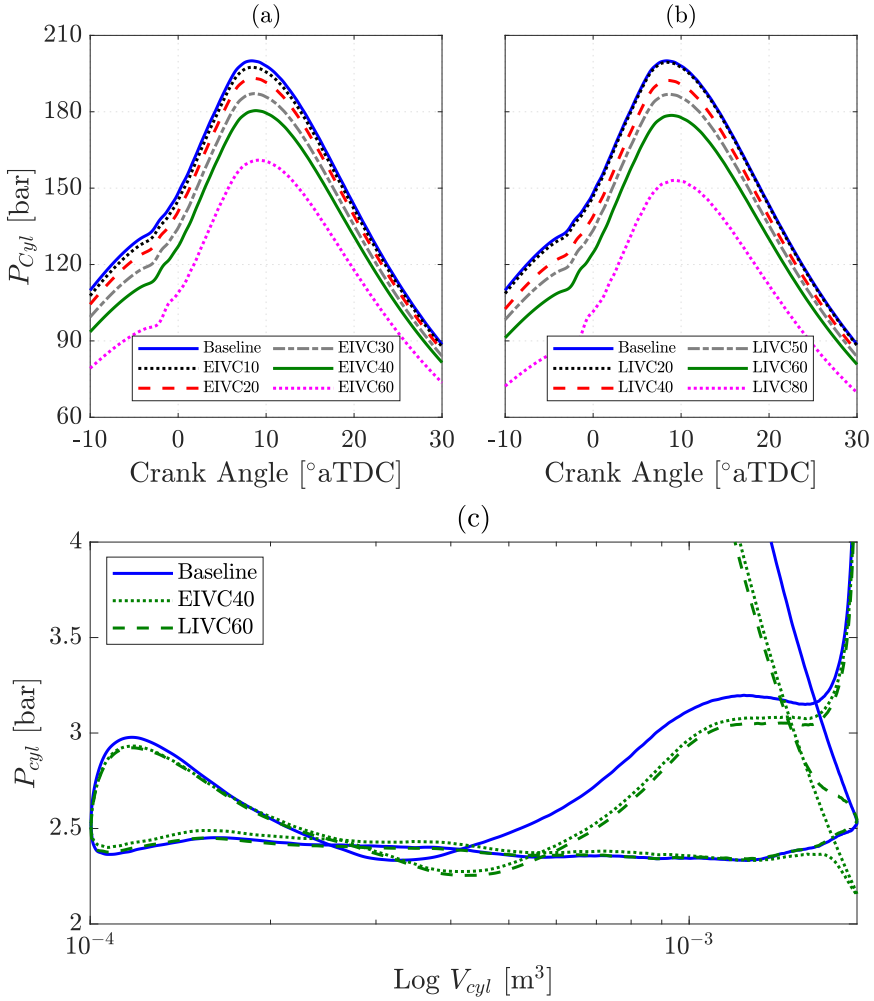

Figure 4.4: Pressure trace for the EIVC (a) and LIVC cases (b) and zoomed-in view of the pumping loop for the baseline, EIVC40 and LIVC60 cases (c) at constant intake manifold pressure and NO_x.

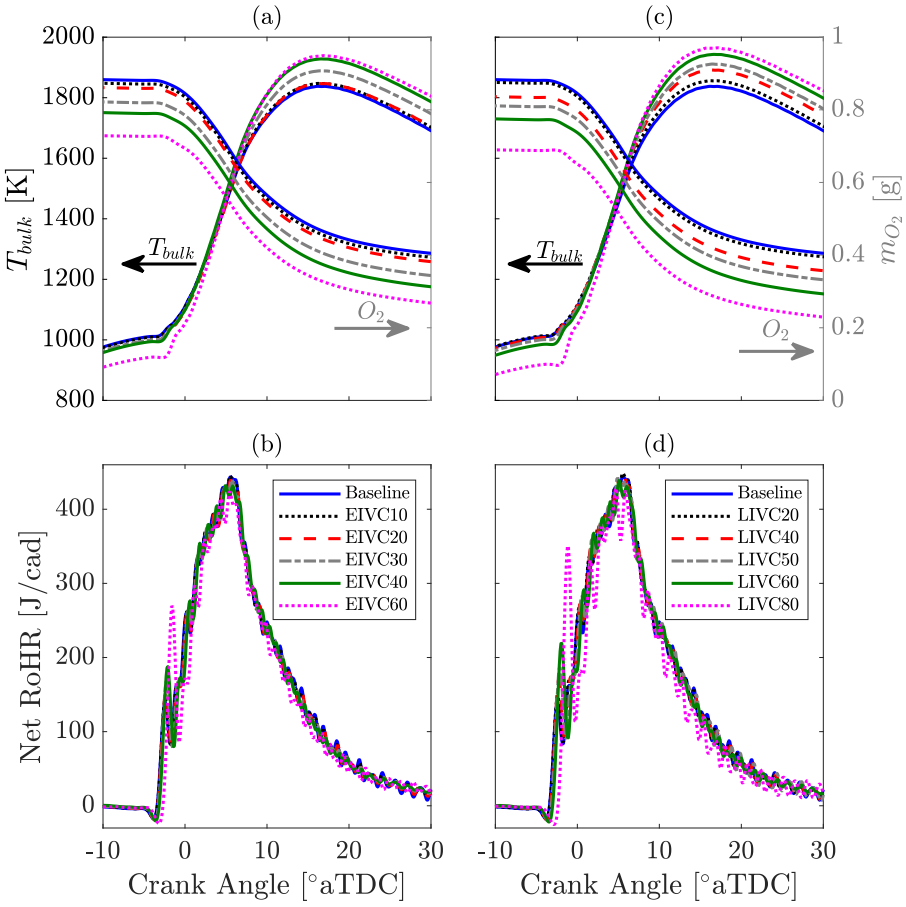

Figure 4.5: Bulk cylinder average temperature, in-cylinder O_2 mass (a) and net rate of heat release (b) during combustion for EIVC cases at constant intake manifold pressure and NO_x. Bulk cylinder average temperature, in-cylinder O_2 mass (c) and net rate of heat release (d) during combustion for LIVC cases at constant intake manifold pressure and NO_x.

NO_x formation is influenced by combustion flame temperatures, the duration and timing of the peak combustion temperatures, and the oxygen content in the cylinder [61]. While the EIVC/LIVC cases have higher combustion temperatures, NO_x parity is achieved at lower Y_{EGR} compared to the baseline condition. The change in Y_{EGR} requirement is due to the reduced oxygen availability in the cylinder having a stronger effect on NO_x production than the elevated combustion temperatures.

Figures 4.5b and 4.5d show the net heat release rates as a function of crank angle for the EIVC and LIVC cases, respectively. EIVC and LIVC strategies lower combustion pressures and end of compression temperatures, due to lower effective

compression ratios, extending ignition delays that retard CA50 for the Miller strategies, as shown earlier in Figure 4.3f. The longer ignition delays also increase rates of premixed combustion. The increasing amount of premixed combustion occurring before TDC contributes to the increased fuel consumption that accompany extreme IVC timings. Increasing premixed combustion also contributes to the reduced NO_x emissions since premixed combustion produces minimal NO_x [24].

4.4 Miller Cycle at Constant λ and NO_x

The experiments performed in this section investigate the effect of EIVC and LIVC profiles on the combustion process at equivalent cylinder composition, represented by λ. All actuator settings were set as in the previous section, except for P_{INT}. Boost pressure was increased to overcome the reduced VE of the Miller profiles such that $\lambda_i = \lambda_{baseline} = 1.5$. Fuel injection pulse width and Y_{EGR} were again adjusted to match the baseline load (nIMEP = 1.76 MPa) and NO_x output (4.5 g/kWh).

Figure 4.6 displays cycle average results for the performance of each EIVC/LIVC case at constant air-fuel ratio as a function of IVC timing. As the EIVC/LIVC strategies become more aggressive, a number of experimental trends can be identified that distinguish constant air-fuel ratio operation from that at constant P_{INT}.

As expected, the mass air flow through the engine remains fairly constant in spite of the Miller VE penalties, due to the increase in intake pressure. For the EIVC cases, the cylinder pressure at IVC increased compared to the previous study due to the increased intake manifold pressure, but peak cylinder pressures remained below the baseline level. The LIVC cases had much higher pressures at IVC than in Section 4.3, but their low CR_{eff} kept the peak cylinder pressures below that of the baseline case.

Exhaust temperatures still show a small increase with more aggressive Miller strategies, even though air-fuel ratio is kept constant. This behavior is likely due to the lower EGR requirement for NO_x parity. Unlike the results at constant intake

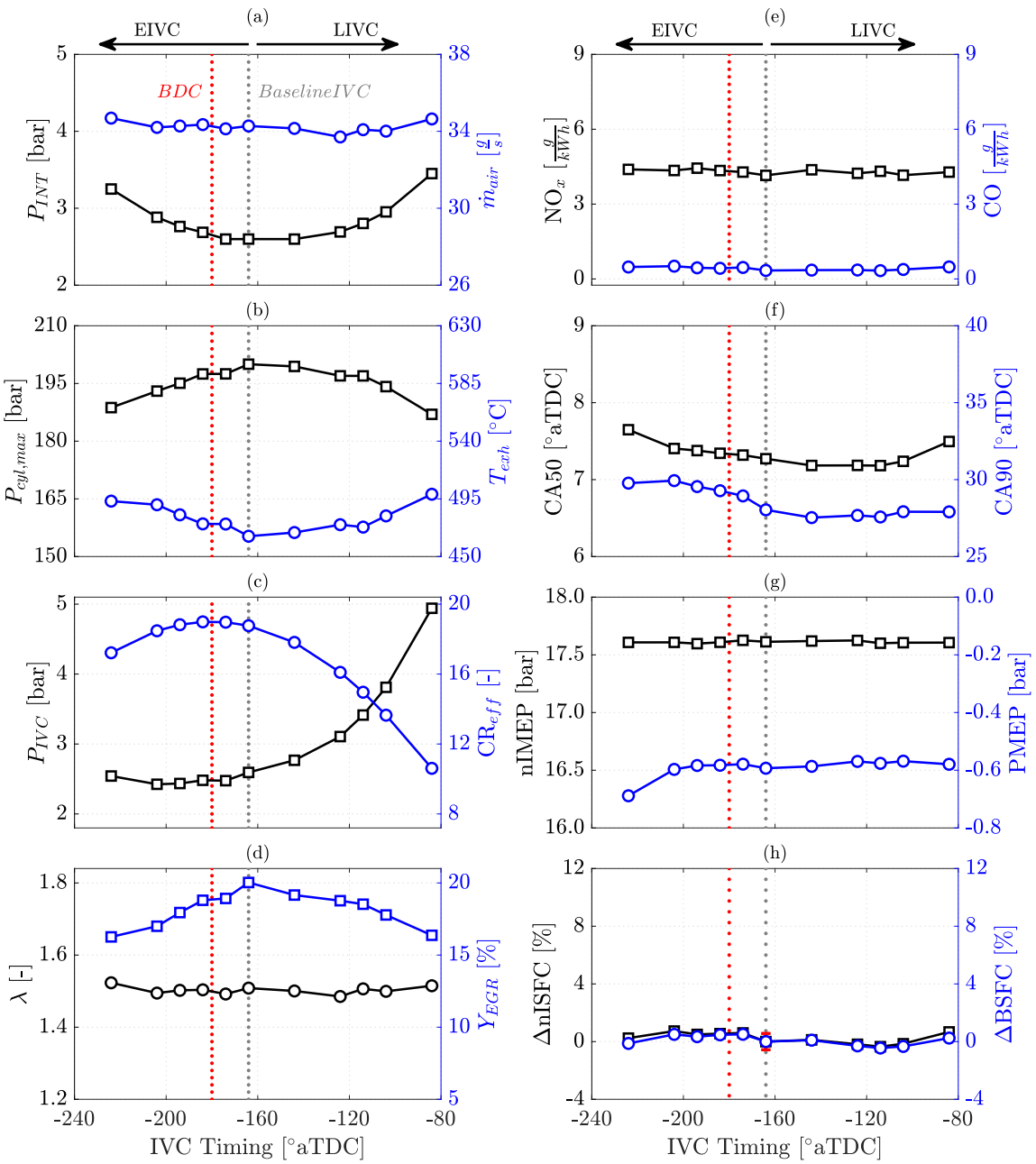

Figure 4.6: Engine performance based on IVC timing at constant air-fuel ratio and engine-out NO_x emission levels. The dotted grey line shows the baseline IVC timing while the dotted red line shows the BDC location. Square markers correspond to the left axis while circle markers correspond to the right axis. Cylinder pressure at IVC and effective compression ratio (a); intake pressure and mass air flow through the engine (b); peak cylinder pressure and exhaust temperature (c); air-fuel ratio and EGR mass fraction (d); indicated specific NO_x and CO engine-out emissions (e); timing of CA50 and CA90 (f); net indicated and pumping mean effective pressure (g); Relative change in ISFC and BSFC compared to the baseline (h).

pressure, CO emissions are similar to the baseline case due to the constant air-fuel ratio mixtures. Similarly CA50/CA90 and PMEP remain approximately constant with changes in IVC timing. Maintaining constant air-fuel ratio results in relatively flat ΔnISFC and ΔBSFC curves, with no statistically significant change demonstrated by any EIVC or LIVC case relative to the baseline case, unlike in Section 4.3.

The cylinder pressures for the EIVC and LIVC profiles, shown in Figure 4.7a and 4.7b respectively, are closer to the baseline values. The stability of pumping losses shown in Figure 4.6g is reflected in the size parity of the pumping loop for the Miller IVC cases shown in Figure 4.7c.

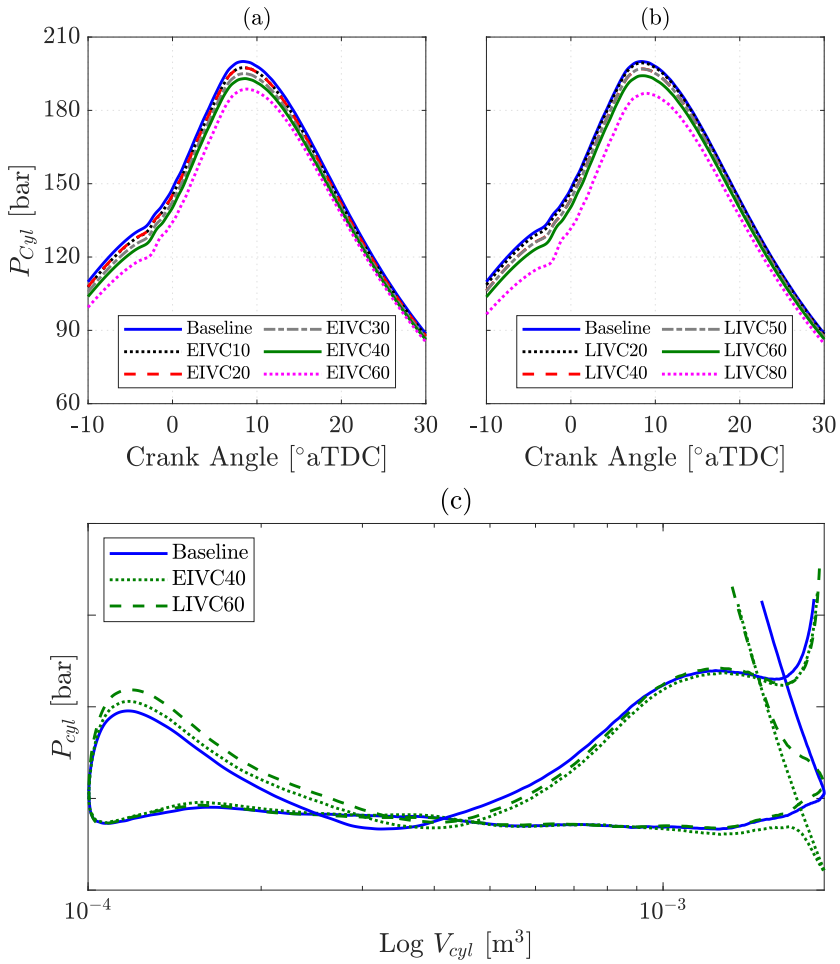

Figure 4.7: Pressure trace for the EIVC (a) and LIVC cases (b) and zoomed-in view of the pumping loop for the baseline, EIVC40 and LIVC60 cases (c) at constant air-fuel ratio and NO_x. The pumping loops in (c) have been aligned, to a constant intake stroke pressure, to facilitate size comparisons.

Similar to the results of Section 4.3, the EIVC and LIVC strategies lead to lower end of compression pressures and temperatures. Unlike those results, estimated peak bulk cylinder temperatures and the m_{O_2} curves shown in Figures 4.8a and Figure 4.8c are nearly identical to those of the baseline case given the similar composition between the mixtures. The magnitude of the reduction in Y_{EGR} required to maintain NO_x parity with the baseline case is diminished because of this similar in-cylinder composition.

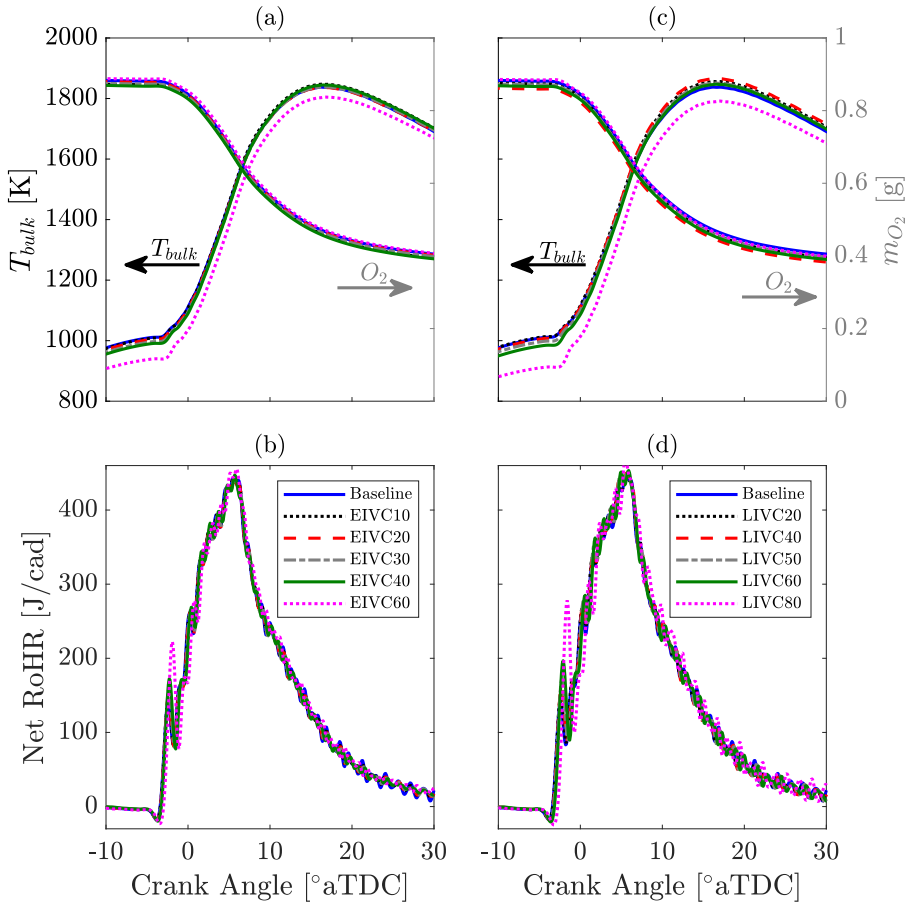

Figure 4.8: Bulk cylinder average temperature, in-cylinder O_2 mass (a) and net rate of heat release (b) during combustion for EIVC cases at constant air-fuel ratio and NO_x. Bulk cylinder average temperature, in-cylinder O_2 mass (c) and net rate of heat release (d) during combustion for LIVC cases at constant air-fuel ratio and NO_x.

Heat release profiles still depict a higher and delayed premixed spike with more aggressive EIVC or LIVC strategy, due the conservation of decreased end-of compres-

sion temperatures. Operation under more dilute conditions, compared to Section 4.3, decreased the magnitude of rates of premixed combustion.

4.5 Miller Cycle Performance as a Function of Overall Turbocharger Efficiency

The EIVC/LIVC studies presented in the previous sections offer valuable insight into Miller cycle performance, however, they do not consider the effect on the turbocharger system.

To quantify the effectiveness of Miller cycle on improving efficiency and NO_x, the experimental approach was extended by using an overall turbocharger efficiency (η_{TC}) metric. η_{TC} is defined as shown in Equation 4.4, which relates the change in enthalpy of the hypothetical, isentropic compressor to that of the hypothetical, isentropic turbine.

$$\eta_{TC} = \frac{\dot{m}_c(h_{o,c} - h_{i,c})}{\dot{m}_t(h_{i,t} - h_{o,t})} \approx \frac{\dot{m}_c c_{p,c}\left[T_{i,c}\left(\frac{P_{o,c}}{P_{i,c}}\right)^{\frac{\gamma_c - 1}{\gamma_c}} - T_{i,c}\right]}{\dot{m}_t c_{p,t}\left[T_{i,t} - T_{i,t}\left(\frac{P_{o,t}}{P_{i,t}}\right)^{\frac{\gamma_t - 1}{\gamma_t}}\right]} \tag{4.4}$$

where $\dot{m}$ is mass flow, h is enthalpy, T is temperature, P is pressure, γ is the heat capacity ratio, and c_p is the specific heat capacity at constant pressure. The subscripts c and t represent compressor and turbine, respectively. The subscripts i and o represent the inlet and outlet states, respectively. The compressor inlet parameters utilized in this calculation are assumed to be at ambient conditions. The compressor outlet pressure was set by the intake manifold pressure and the compressor outlet

temperature was estimated using isentropic compression. The turbine inlet temperature was set by the exhaust manifold temperature and the turbine inlet pressure was set by the exhaust manifold pressure. The turbine outlet temperature was estimated using isentropic expansion to ambient pressure.

η_{TC} describes the efficiency of the turbocharger system at converting exhaust energy into intake boost. Changes in mass air flow, exhaust temperature, and manifold pressures will have an effect on the boundary conditions of the turbocharger system and should be taken into account.

Figure 4.9 shows the η_{TC} values from the data presented in the previous sections. At constant intake pressures, the EIVC and LIVC profiles required a lower η_{TC} than the baseline condition due to the higher enthalpy of the exhaust gas. The opposite trend applies to the constant air-fuel ratio conditions, where a more efficient turbocharger is needed to generate the required intake pressures.

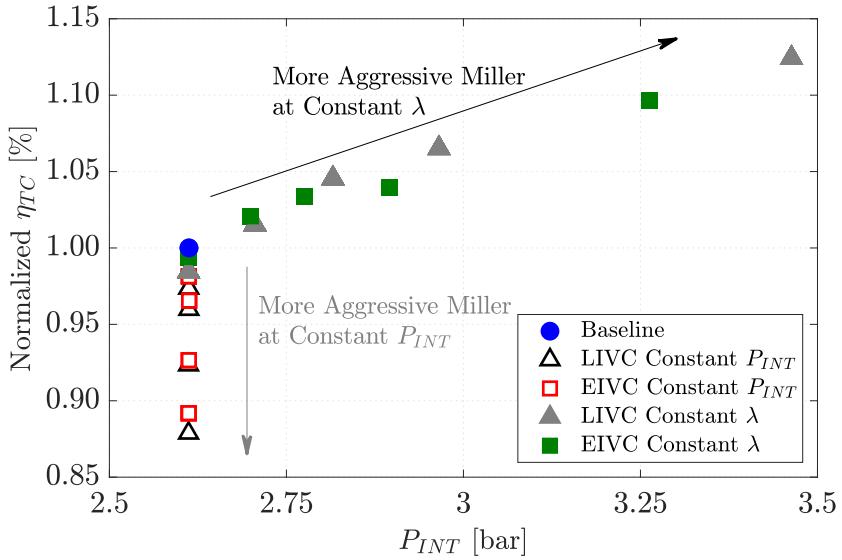

Figure 4.9: Normalized overall turbocharger efficiency versus intake pressure. Operation at constant intake manifold pressure results in a lower η_{TC} for the EIVC/LIVC cases, while operation of these Miller cycle profiles at constant air-fuel ratio requires a η_{TC} higher than that of the baseline.

The experiments performed in this section evaluate the performance of EIVC40 and LIVC60 at three η_{TC} levels, the baseline η_{TC} and two elevated η_{TC} cases. Engine-

out NO_x emissions are kept at the baseline level for all cases. EIVC40 (i.e. IVC at 40 CAD before baseline IVC) and LIVC60 (i.e. 60 CAD after the baseline IVC) are Miller strategies of equivalent VE decrease, compared to the baseline.

Figure 4.10 displays the cycle average results for the performance of the conventional, EIVC40, and LIVC60 cases as a function of normalized η_{TC}. As η_{TC} increases, a number of experimental trends can be identified that distinguish between operation with Miller cycle and conventional valve timings.

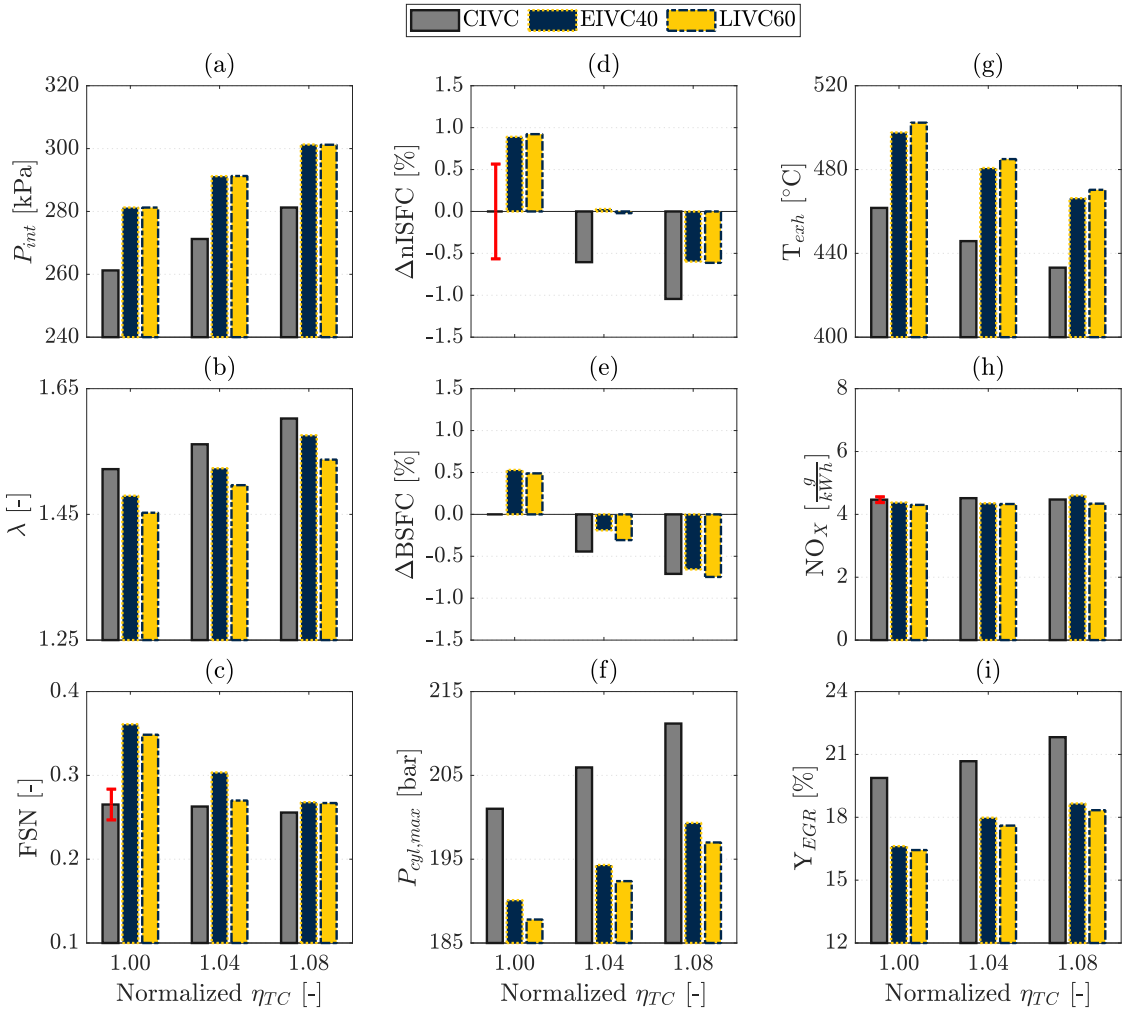

Figure 4.10: Engine performance based on normalized η_{TC}. Intake manifold pressure (a); air-fuel ratio (λ) (b); filter smoke number (c); change in net indicated specific fuel consumption (d); change in brake specific fuel consumption (e); maximum in-cylinder pressure (f); exhaust temperature (g); indicated specific NO_x (h); Y_{EGR} (i).

EIVC40 and LIVC60 operate at about 200 mbar higher intake manifold pressure

than the conventional timing cases at all equivalent η_{TC}. This observation is primarily due to the higher exhaust enthalpy of the Miller cycle cases associated with their elevated exhaust temperatures.

Despite lower intake manifold pressures, the conventional cases always operate at higher air-fuel ratios due to superior VE. The conventional cases exhibit a small benefit in particulate matter emissions over the EIVC40 and LIVC60 cases, as indicated by the lower FSN.

The ΔnISFC comparison demonstrates that EIVC40 and LIVC60 do not improve fuel consumption compared to the conventional case at any η_{TC} level. However, ΔBSFC trends show that these EIVC/LIVC strategies can obtain fuel consumption parity to the conventional timing at higher η_{TC} levels. The peak cylinder pressures of conventional valve operation at higher intake pressures cause increased friction losses. The observed ΔBSFC improvement is thus attributed to the peak cylinder pressure reduction of EIVC/LIVC operation.

Overall, exhaust temperatures decrease with higher η_{TC} due to leaner mixtures. Exhaust temperatures for the EIVC40 and LIVC60 cases, however, do not fall below the baseline exhaust temperature. This proves favorable for exhaust aftertreatment system development, as high temperatures are desirable for effective exhaust aftertreatment.

At the baseline η_{TC}, EIVC40 and LIVC60 meet the target NO_x emissions at lower EGR rates than the conventional cases. However, as η_{TC} increases all cases require elevated EGR rates to maintain NO_x parity, likely due to the higher air-fuel ratio mixtures.

4.6 Summary and Conclusions

This chapter presents an experimental investigation of the effect of Miller cycle on the combustion process, emissions, and thermal efficiency in a single cylinder heavy-

duty research engine equipped with a fully-flexible hydraulic valvetrain. Miller cycle operation was achieved using a suite of EIVC and LIVC profiles ranging from 60 CAD before and 80 CAD after the nominal IVC timing. The experiments were carried out at a fixed engine load of 1.76 MPa net IMEP at 1160 RPM. Start of injection timing was fixed at 6.7° bTDC and engine-out NO_x was held constant at 4.5 g/kWh by adjusting Y_{EGR}.

- While effective compression ratio was symmetric around BDC, VE decrease due to Miller valve timing was not. LIVC profiles were less effective at reducing VE than EIVC, likely due to flow inertia effects and the need to expel fresh charge through a closing intake valve.

- Miller cycle profiles of equivalent VE reduction (e.g. EIVC40 & LIVC60) resulted in similar changes in combustion characteristics and emissions compared to the baseline condition.

- More aggressive EIVC/LIVC profiles lead to:

  - Lower EGR requirements, higher exhaust temperatures and significantly lower peak cylinder pressures.

    * These effects were much less pronounced at the constant air-fuel ratio condition than at the fixed intake manifold pressure condition.

  - Deteriorated net indicated specific fuel consumption compared to the baseline condition at constant intake manifold pressures due to unfavorable mixture properties and slower burn rate late in the combustion process.

  - Net indicated specific fuel consumption parity with the baseline case when the air-fuel ratio was preserved, due to similar composition and heat release rates.

- Miller cycle can have a significant impact on the boundary conditions of a real turbocharger system due to changes in exhaust enthalpy. For that reason, select EIVC/LIVC cases were compared to the baseline condition as a function of overall turbocharger efficiency (η_{TC}). The analysis showed that:
  - At the baseline η_{TC}, Miller cycle profiles lower peak cylinder pressures and increase exhaust temperatures with a minimal increase in nISFC and FSN. The calculated BSFC increase was less than the nISFC penalty due to lower peak cylinder pressures.
  - At higher η_{TC} than baseline, Miller cycle profiles maintain the benefits of lower peak cylinder pressures and higher exhaust temperatures without increasing BSFC or FSN.

This study demonstrated the effects of Miller cycle on the combustion process in a single cylinder research engine. At high overall turbocharger efficiencies, Miller cycle implementation offers reduced peak cylinder pressure and elevated exhaust temperature over conventional intake valve profiles, without compromising BSFC, NO_x or PM emissions. Further experiments should be conducted on a production engine to validate the effect of EIVC/LIVC profiles on BSFC and turbocharger performance. The η_{TC} calculations used in this study are meant to predict real engine behavior, but behavior in a multi-cylinder engine may be different due to the pulsating flow and cylinder-to-cylinder interaction in the intake and exhaust manifolds [74, 75].

Additionally, given Miller cycle strategies were shown to increase combustion temperatures via decreased cylinder dilution, work in Chapter V will pair Miller cycle strategies with a TBC piston. In Chapter III, TBC pistons were shown to maintain ISFC performance with an uncoated baseline despite operation at a lower air-fuel ratio, which should prove significant in Miller cycle applications.

CHAPTER V

Extreme Miller Cycle with High Intake Boost for Improved Efficiency and Emissions in an Insulated Heavy-Duty Diesel Engine

Extreme Miller cycle strategies, and the elevated boost pressures necessary for their operation, are utilized in the present work to experimentally push the boundaries of the typical IVC operating range found in the literature [76, 77] and investigate the implications of pairing a TBC piston with Miller cycle strategies to build on the findings of Chapters III and IV. The experiments were conducted in the following four stages using the single cylinder research engine setup detailed in Chapter II: First, the effect of high boost pressures with conventional intake valve timing on an insulated diesel engine is analyzed. The influence of EGR on the NO_x and particulate matter emissions with the TBC piston is also analyzed. Second, the effect of extreme Miller strategies on the combustion process is analyzed at fixed cylinder charge composition. Third, Miller cycle is analyzed under high boost at constant NO_x emissions to investigate the impact of NO_x control via IVC modulation on fuel conversion efficiency with a TBC piston. Fourth, Miller cycle is analyzed at equivalent overall turbocharger efficiency to identify the IVC strategy best suited for high boost applications with a TBC piston. The latter two sections of this chapter are also meant to identify differing

behavior between EIVC and LIVC strategies with equivalent volumetric efficiency.

5.1 Operating Conditions

The IVC strategies listed in Table 5.2, were tested under the engine parameters outlined in Table 5.1 using both an uncoated and TBC piston (TBC B from Chapter III). Figure 5.1 shows the valve lift traces for each intake profile.

Table 5.1: Engine operating parameters

Parameter	**Value**
Engine speed	1160 RPM
Engine load (nIMEP)	1.76 MPa
Engine coolant temperature	90°C
Intake plenum temperature	35°C
Start of injection timing[1]	-6.7° aTDC
Intake valve opening timing	350° aTDC
Exhaust valve opening timing	154° aTDC
Exhaust valve closing timing	354° aTDC

Table 5.2: Intake valve closing strategies

Intake Valve Strategy	**Intake Valve Closing Timing[1]**
EIVC40	-204° aTDC
CIVC	-164° aTDC
LIVC60	-104° aTDC
LIVC80	-84° aTDC
LIVC100	-64° aTDC

In previous chapters, air-to-fuel equivalence ratio was used to compare the cylinder composition between the IVC cases. The fuel-to-charge equivalence ratio [78], ϕ', is introduced because the air-to-fuel equivalence ratio does not fully represent the characteristics of the cylinder charge when there is EGR dilution. ϕ' is defined as shown in Equation 5.1.

[1] All timings are referenced to combustion TDC and @ 0.35 mm lift.

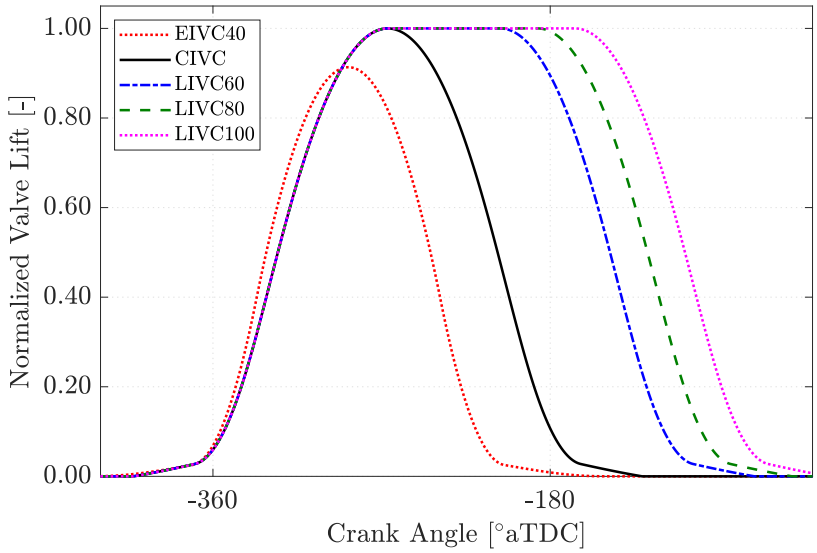

Figure 5.1: Normalized valve lift profiles for EIVC, conventional IVC (CIVC) and LIVC strategies used in this work. EIVC40 refers to a 40 CAD advancement from the conventional IVC timing, LIVC60 refers to a 60 CAD delay, LIVC80 refers to an 80 CAD delay and LIVC100 refers to a 100 CAD delay.

$$\phi' = \frac{\frac{m_f}{(m_a+m_{EGR})}}{(\frac{m_f}{m_a})_{ST}} = \frac{\phi(1-Y_{EGR})}{1+Y_{EGR}*\phi*(\frac{m_f}{m_a})_{ST}} \approx \phi(1-Y_{EGR}) \tag{5.1}$$

The fuel-to-charge equivalence ratio reflects the overall dilution of a mixture with air and/or EGR. ϕ' is directly related to the burned gas temperature of the mixture and represents its specific energy content. For mixtures with only air dilution, the terms ϕ and ϕ' are equivalent. As such, ϕ' will be used along with λ to better define the composition of the cylinder charge in subsequent analyses.

5.2 High Boost Effects on an Insulated Piston with Conventional IVC

The experiments performed in this section investigate the effect of elevated intake manifold pressures on the combustion process using the CIVC profile shown in Figure 5.1 with both an uncoated and TBC piston. Additionally, Y_{EGR} was modulated

from 0 to 20% at each boost level to analyze the influence of EGR on TBC performance. All actuator settings were kept constant as outlined in Table 5.1 and fuel rail pressure was fixed at 125 MPa. The intake manifold absolute pressure was increased from 240 to 320 kPa with fuel injection pulse width adjusted to match the baseline load (nIMEP = 1.76 MPa) at each boost iteration. The intake manifold pressure was capped at an absolute pressure of 320 kPa to avoid exceeding the research engine's peak cylinder pressure rating.

Figure 5.2 displays cycle average results of elevated boosting on the combustion process and NO_x emissions for both the uncoated piston and the TBC piston. As the intake manifold pressures become more extreme, a number of trends can be identified. The λ trends shown in Figure 5.2a show that the TBC piston has a negligible effect on volumetric efficiency and thus good temperature swing behavior during the intake stroke. The indicated specific NO_x emissions ($\widehat{ISNO_x}$) data shown in Figure 5.2d is normalized with respect to the baseline for this operating condition (described as A75 in Chapter III). The increased NO_x emissions were expected given the change in dilution indicated by λ. The TBC piston shows no statistically significant impact on the NO_x emission trends across all tested conditions.

Figure 5.3a and Figure 5.3b show the relative change in indicated and brake specific fuel consumption compared to the baseline point, respectively, as a function of normalized indicated specific NO_x emissions. The high boost point has a 2.4% lower ISFC than the baseline condition, with a 59% increase in engine-out NO_x emissions. Increasing boost pressure leads to reduced fuel consumption as a result of various factors. Increasing dilution, as indicated by the changes in λ shown in Figure 5.2a, benefits thermal efficiency due to the improvement of the thermodynamic properties of the mixture, notably specific heat capacity, that help with extracting work [79]. Additionally, improved thermal efficiency is obtained from the reduction of overall combustion duration as shown in Figure 5.2e. The shorter burn duration results in

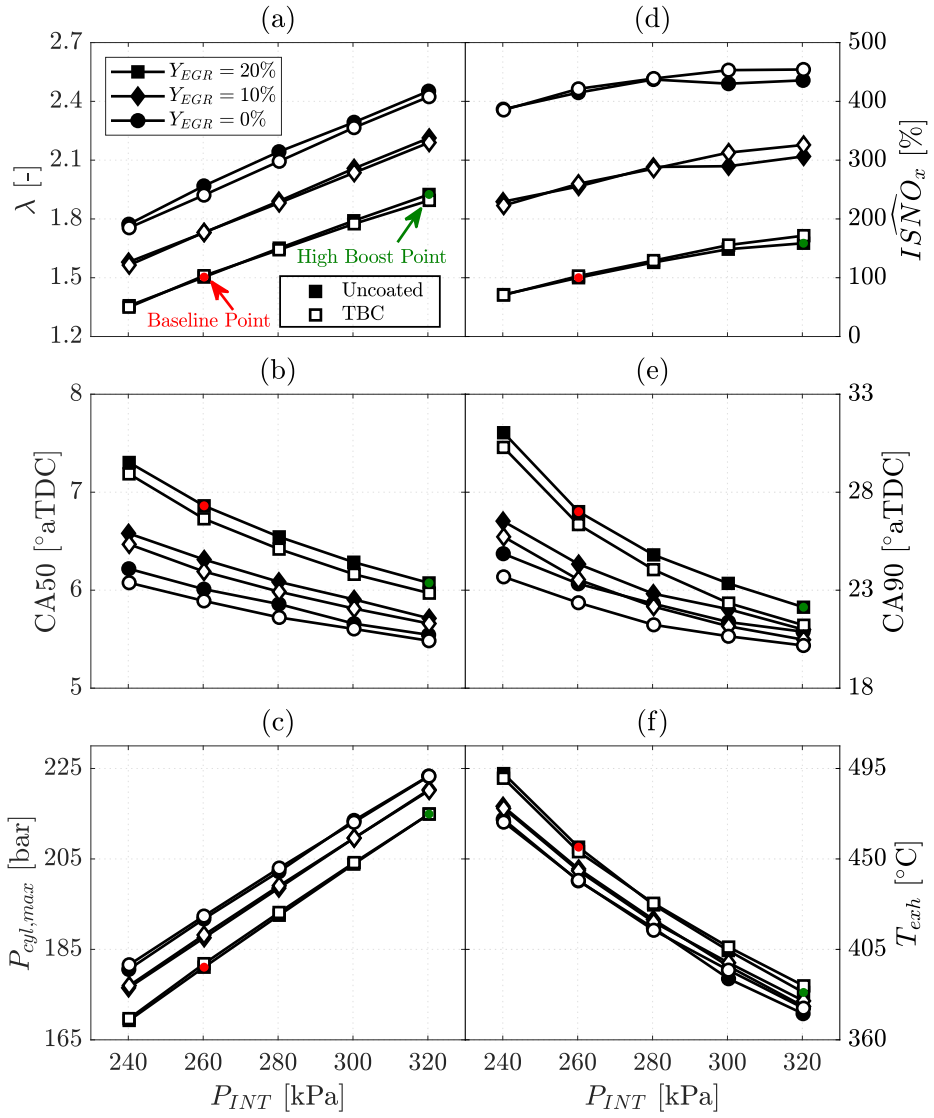

Figure 5.2: (a) Air-to-fuel equivalence ratio (λ), (b) timing of CA50, (c) peak cylinder pressure ($P_{cyl,max}$), (d) normalized indicated specific NO_x emissions ($\widehat{ISNO_x}$), (e) timing of CA90 and (f) exhaust temperature (T_{exh}) as a function of intake manifold pressure.

higher peak pressures, shown in Figure 5.2e, and thus more expansion work. The shift in combustion phasing shown in Figure 5.2c is not as beneficial to thermal efficiency as the "optimal" CA50 for this particular condition is in the 6-7° aTDC zone.

The TBC piston obtained an additional 0.6% improvement in ISFC over the baseline condition, with an additional 13% increase in NO_x emissions. Reducing Y_{EGR} from 20% to 0% does not change the behavior of the TBC, challenging the theory

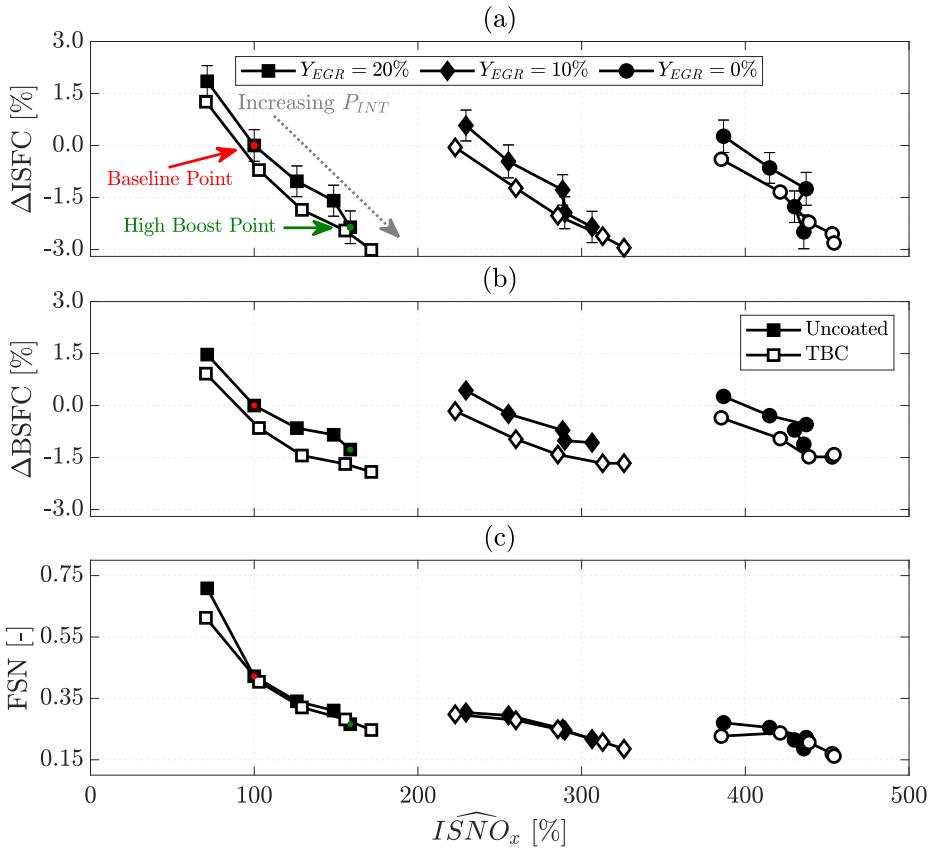

Figure 5.3: (a) Relative change in ISFC compared to the baseline point (ΔISFC), (b) relative change in BSFC compared to the baseline point (ΔBSFC) and (c) filter smoke number (FSN) as a function of normalized indicated specific NO_x emissions ($\widehat{ISNO_x}$).

posed in Section 3.5 with regard to high EGR rates limiting the potential of the TBC piston by keeping combustion temperatures low.

Increasing boost pressure yields diminishing returns, as the ISFC improvements are not as significant at the higher boost pressures as they are at lower pressures. The BSFC benefit at the extreme boost pressures is compromised more so than the ISFC benefit due to increased friction losses stemming from elevated cylinder pressures. BSFC for the high boost point is only 1.3% lower than the baseline case due to the 34 bar increase in peak cylinder pressure shown in Figure 5.2e. The TBC piston improves BSFC for the high boost point by another 0.6%. The TBC had no effect on peak cylinder pressures, thus the BSFC improvements were not due to changes

in friction losses. Reducing Y_{EGR}, on the other hand, does increase peak cylinder pressures and thus slightly increases BSFC for both the uncoated and TBC pistons.

The FSN improvements shown in Figure 5.3c were expected given the increased dilution indicated by λ. The TBC coating does not improve the NO_x-PM curve under any of the tested conditions, but it also does not degrade it. Increasing Y_{EGR} from 0% to 20% results in a small increase in FSN for the high boost points, indicating the wave bowl geometry likely dominates among the PM oxidation processes. The decrease in exhaust temperature shown in Figure 5.2f is especially detrimental given sharp increases in NO_x emissions will be increasingly difficult to treat with a modern aftertreatment system at low exhaust temperatures.

Figure 5.4 compares the uncoated and TBC piston baseline and high boost points under greater detail to identify the combustion characteristics responsible for their differences. The total height of the stacked bars in Figure 5.4 represents the FuelMEP, the amount of fuel energy input to the engine per combustion cycle, at each intake manifold pressure to match the baseline load of 1.76 MPa nIMEP. As such, a shorter column is more efficient than cases with taller columns. The text inside the baseline column is the percentage of total fuel energy utilized by each of the following 5 energy pathways: BMEP, FMEP, PMEP, EXMEP and HTMEP. The text inside each of the other bars is the change in fuel energy for those energy pathways with respect to the baseline.

In Figure 5.4a, operation at $P_{INT} = 260$ kPa shows the TBC piston's biggest influence on the fuel energy pathways is on heat transfer losses. Increasing boost pressure decreases combustion temperatures by $\approx$ 140K, as shown in Figure 5.5a. Combined with shorter combustion duration, as shown in Figure 5.2e, the lower combustion temperatures reduce heat transfer. However, at these lower combustion temperatures the TBC has a negligible effect on heat transfer losses and instead reduces losses to the exhaust stream. Increasing P_{INT} to 320 kPa highlights the dependence of TBC

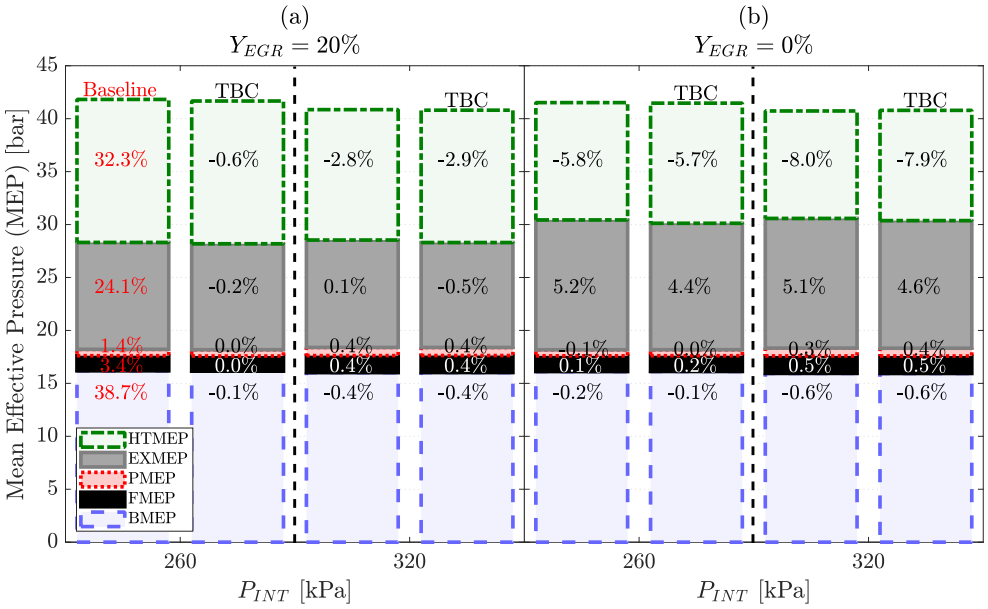

Figure 5.4: Detailed breakdown of the fuel energy pathways at the baseline (260 kPa) and high (320 kPa) intake manifold absolute pressures for both the uncoated and TBC pistons at (a) $Y_{EGR} = 20\%$ and (b) $Y_{EGR} = 0\%$.

performance on combustion temperatures.

Figure 5.4b, shows that reducing Y_{EGR} has a similar effect on the TBC piston as increasing boost did in Figure 5.4a, with the TBC piston favoring reducing exhaust losses over heat transfer regardless of boost pressure. Comparing Figure 5.5a to Figure 5.5c shows that reducing Y_{EGR} did not have the anticipated result of increased combustion temperatures that would, in theory, allow the TBC piston to significantly reduce the heat transfer gradient compared to the uncoated piston.

Increased pumping and friction losses associated with high boost operation work against the heat transfer benefit of increased dilution. The TBC's unsubstantial impact on volumetric efficiency and peak cylinder pressure is reflected in the absence of changes to PMEP and FMEP relative to their uncoated counterparts. Increased charge mass conserves exhaust enthalpy for the uncoated cases, despite a significant exhaust temperature decrease of ≈72°C for the 20% Y_{EGR} case. However, all high boost TBC cases improved thermal efficiency via decreased exhaust losses compared to the corresponding uncoated cases.

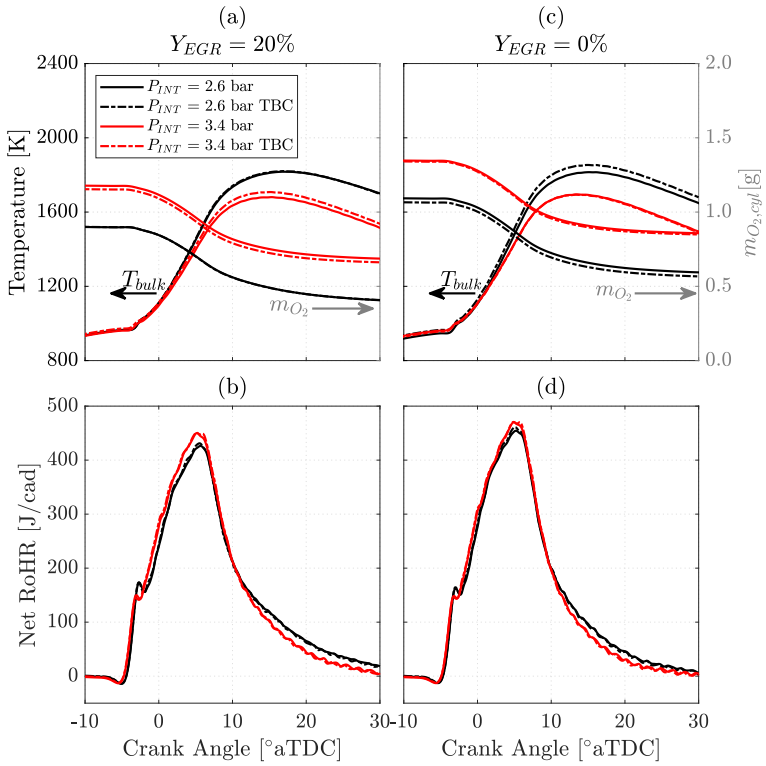

Figure 5.5: (a) Bulk-cylinder temperature, in-cylinder O_2 mass and (b) rate of heat release during combustion at $Y_{EGR} = 20\%$. (c) Bulk-cylinder temperature, in-cylinder O_2 mass and (d) rate of heat release during combustion at $Y_{EGR} = 0\%$.

Figure 5.5a and Figure 5.5c also show the increase in in-cylinder O_2 availability is responsible for the increase in engine-out NO_x emissions at the extreme boost conditions despite the decrease in combustion temperatures. Figure 5.5b and Figure 5.5d show the effect of increased boost pressures and reduced Y_{EGR} on the rate of heat release is minimal. While levels of premixed combustion decrease minimally, the magnitude of the diffusion burn portion of combustion increases and advances phasing.

5.3 Extreme Miller Cycle Effects at Constant Composition

The elevated intake manifold pressures used in Section 5.2 improved fuel consumption at the expense of sharp increases in peak cylinder pressures, engine-out NO_x emissions, and reduced exhaust temperatures. Efficiency gains arising out of

using a TBC piston under high boost conditions stem from reduced exhaust losses, which could further complicate exhaust aftertreatment development for heavy-duty diesel engines. The experiments conducted in this section investigate the ability of Miller cycle strategies to address those deficiencies. Only LIVC profiles are utilized in this study because piston-valve clash prevents the use of equivalent extreme EIVC profiles. Only an uncoated piston is utilized to isolate Miller cycle effects. All actuator settings were set as outlined in Table 5.1, with Y_{EGR} fixed at 0% and fuel rail pressure reduced to 95 MPa in order to operate the engine with the LIVC100 profile. Fuel injection pulse width was adjusted to match the baseline load (nIMEP = 1.76 MPa) and intake manifold pressure was adjusted for each IVC strategy such that $\lambda = 1.70 \pm 0.03$.

Figure 5.6 displays the cycle average results for 12 key engine performance metrics as IVC timing is delayed from the conventional timing of -164° aTDC up to -64° aTDC at constant λ. The intake manifold absolute pressures for each IVC strategy that met this λ criteria were CIVC at 230 kPa, LIVC60 at 270 kPa, LIVC80 at 320 kPa and LIVC100 at 435 kPa as shown in Figure 5.6a. LIVC strategies require a more efficient turbocharger system to maintain a similar composition with the conventional IVC case as shown in Figure 5.6g.

Figure 5.6b shows the change in ISFC relative to the CIVC case, in which LIVC60 demonstrates a statistically insignificant 0.5% ISFC improvement. While delaying IVC by 80 CAD later than conventional leads to a minor ISFC penalty of 0.3%, retarding IVC by an additional 20 CAD results in a significant 3.1% increase in ISFC. Improved ISFC for LIVC60 is attributed to the favorable combination of increased gas exchange and gross thermal efficiencies, as shown in Figure 5.6c and 5.6d respectively.

Figure 5.6e displays the change in BSFC relative to the CIVC case. Despite having lower pre-combustion pressures, conserving λ resulted in similar peak cylinder pressures among all cases (see Figure 5.6h and Figure 5.6f). Therefore, there was

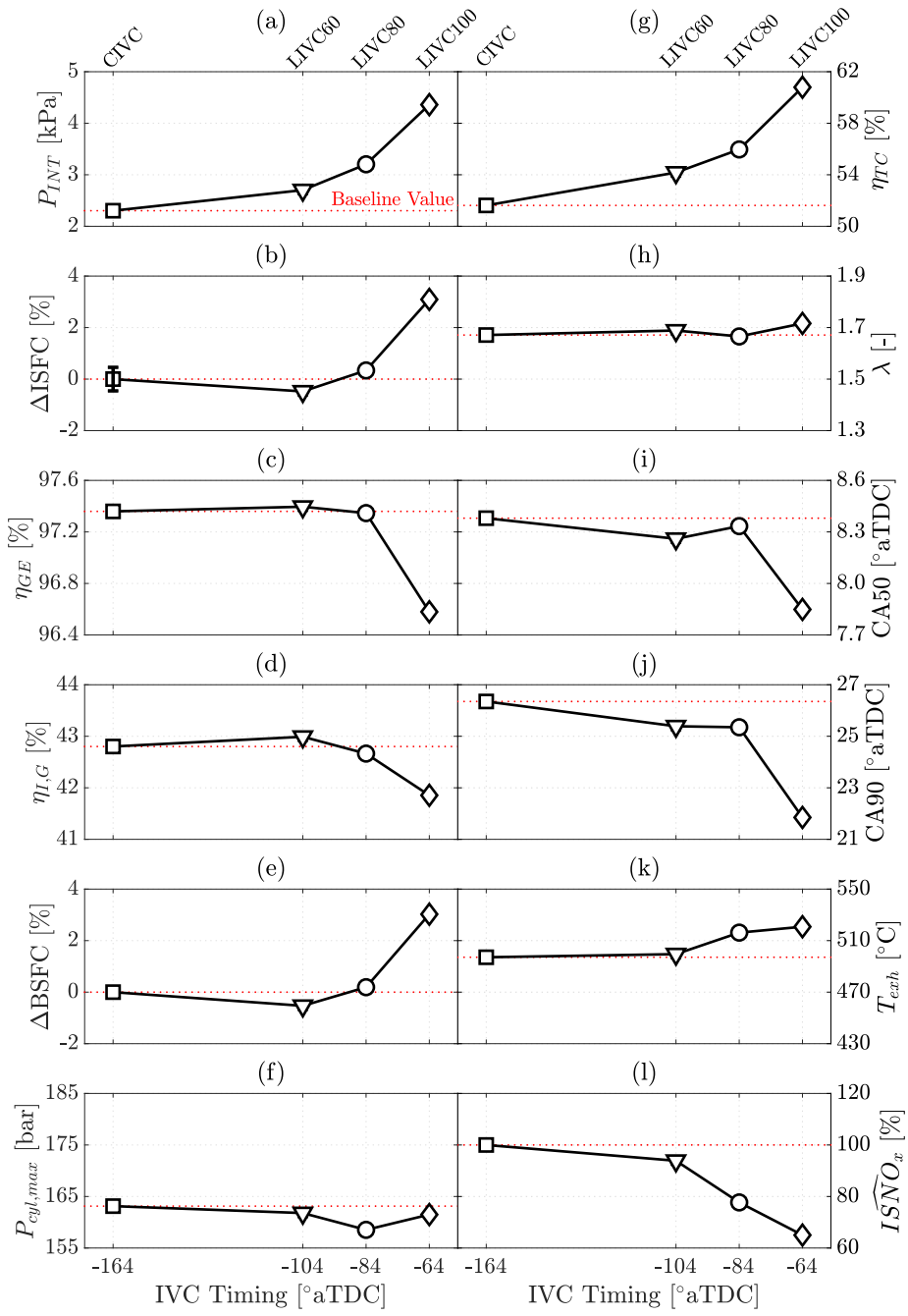

Figure 5.6: (a) Intake manifold absolute pressure (P_{INT}), (b) relative change in ISFC compared to the baseline point (ΔISFC), (c) gas exchange efficiency (η_{GE}), (d) gross thermal efficiency ($\eta_{I,G}$), (e) relative change in BSFC compared to the baseline point (ΔBSFC), (f) peak cylinder pressure ($P_{cyl,max}$), (g) overall turbocharger efficiency (η_{TC}), (h) air-to-fuel equivalence ratio (λ), (i) timing of CA50, (j) timing of CA90, (k) exhaust temperature (T_{exh}) and (l) normalized indicated specific $\mathrm{NO_x}$ emissions ($\widehat{ISNO_{\mathrm{x}}}$) as a function of intake valve closing timing at $\lambda \approx 1.70$. IVC timing is as described in Table 5.2.

no meaningful friction reduction from utilizing LIVC strategies to distinguish brake and indicated engine behavior. Ehleskog et al. [30] also reported a BSFC optimum in the LIVC region with sharp increases at the extremes, under comparable operating conditions.

LIVC60 doesn't affect exhaust temperature, but LIVC80 and LIVC100 increase it by ≈20°C (see Figure 5.6k). Despite equivalent cylinder composition, Figure 5.6l shows a strong correlation between delayed IVC timing and reduced NO_x emissions. Using LIVC100 reduces NO_x emissions by 35%, while LIVC80 and LIVC60 only reduce NO_x emissions by 22% and 6% respectively. Figure 5.7 shows that peak combustion temperatures decrease as IVC timing is delayed. The NO_x benefit of the LIVC profiles is therefore due to lower combustion temperatures, given in-cylinder O_2 concentration, also shown in Figure 5.7, is constant for these λ parity data points.

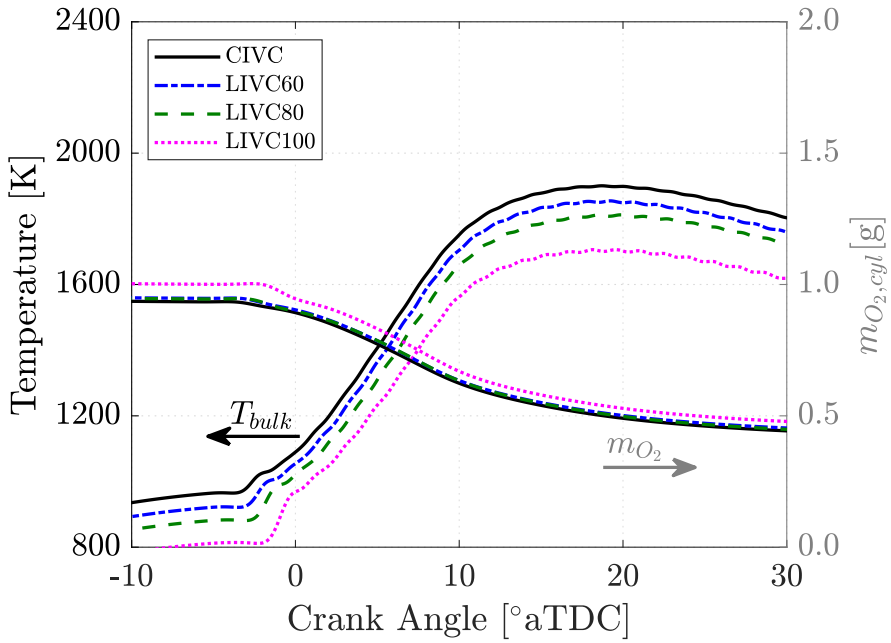

Figure 5.7: The bulk cylinder temperature and in-cylinder O_2 mass during combustion for the CIVC and LIVC cases at $\lambda \approx 1.7$.

These bulk cylinder temperature trends are in stark contrast to those of Section 4.4, wherein combustion temperatures were constant across all Miller strategies. In that study, Y_{EGR} was modulated to keep NO_x emissions constant, affecting com-

bustion temperatures given EGR acts as a heatsink by absorbing combustion heat without participating in combustion reactions. In Section 4.4, LIVC cases maintained NO_x parity with the baseline case at a lower Y_{EGR}, raising combustion temperatures to baseline levels. Because $Y_{EGR} = 0\%$ for the data presented here, the heatsink effect of EGR was absent, revealing Miller cycle strategies have both lower end of compression and peak combustion temperatures when cylinder composition is conserved.

Figure 5.8 displays a breakdown of the fuel energy used by each IVC strategy to match the baseline load. Delaying IVC timing mainly creates a shift of heat transfer losses to the exhaust stream, with a secondary influence on pumping and friction losses. The lower combustion temperatures shown in Figure 5.7 paired with shorter combustion duration, as indicated by the CA50 and CA90 values in Figure 5.6i and Figure 5.6j, reduce heat transfer losses for delayed IVC timings.

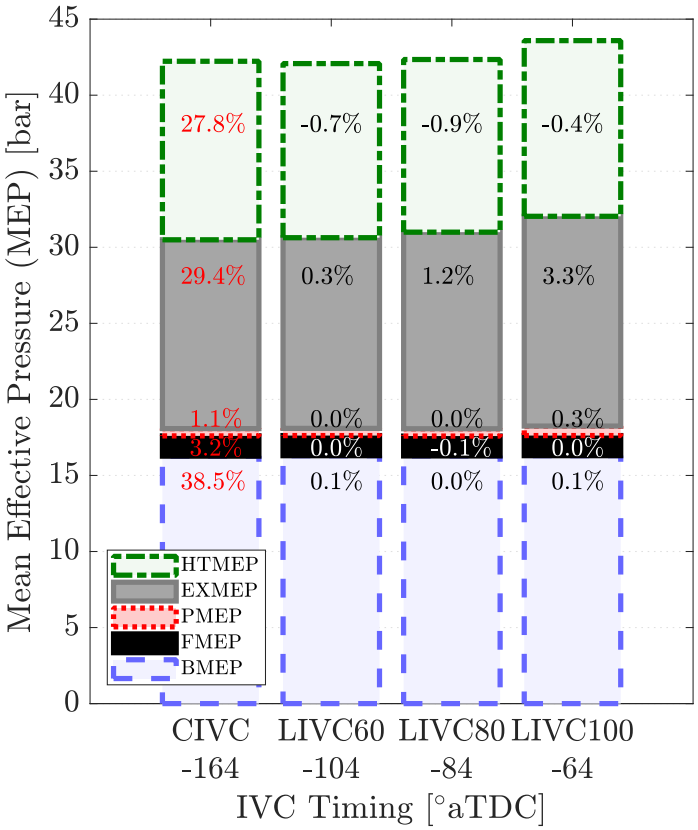

Figure 5.8: Energy breakdown for each IVC timing strategy at $\lambda \approx 1.7$.

The reduction of heat transfer losses compared to the CIVC case contributes to the reduced fuel consumption of the LIVC60 case. Retarding IVC beyond LIVC60 leads to higher exhaust gas losses (EXMEP) than heat transfer (HTMEP) reduction, and ultimately lower BMEP and efficiency. More aggressive LIVC strategies show promise for elevating exhaust enthalpy without a major increase in fuel consumption, as demonstrated for LIVC80, which could benefit diesel exhaust aftertreatment development by counteracting the TBC piston's reduced exhaust enthalpy observed in Section 5.2.

The lower end of compression temperatures and pressures, caused by the lower effective compression ratios of the extreme LIVC profiles, extend ignition delays, increasing the rates of premixed combustion, as shown in Figure 5.9. The increasing amount of premixed combustion occurring before TDC contributes to the observed fuel consumption penalties that accompany extreme IVC timings. Increasing premixed combustion also contributes to the reduced NO_x emissions since premixed combustion produces minimal NO_x [24].

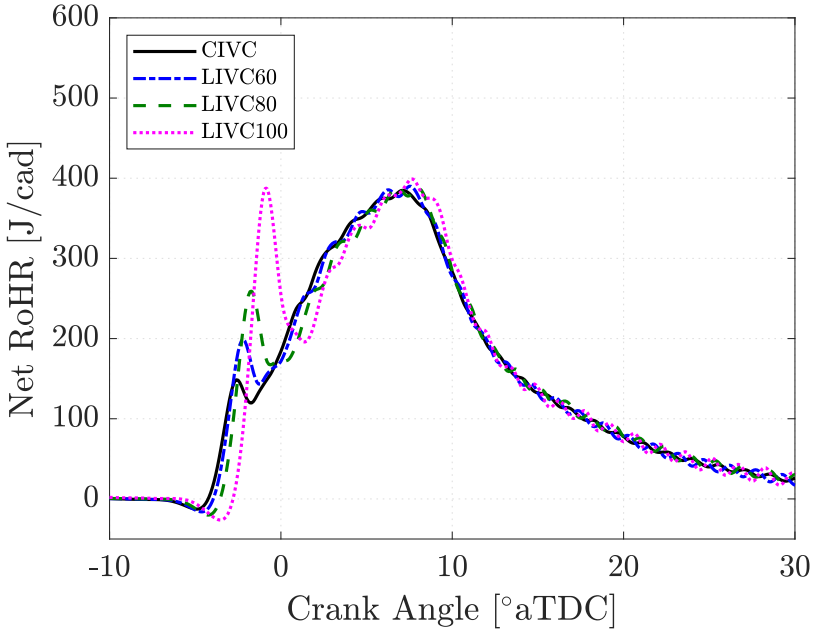

Figure 5.9: The net rate of heat release during combustion for the CIVC and LIVC cases at $\lambda \approx 1.7$.

Figure 5.10a shows the logV-logP diagrams for each of the experimental cases, while Figure 5.10b shows a zoomed-in view of the pumping loops. The latter have been aligned, to a constant intake stroke pressure, to highlight the increase in area of the pumping loop as LIVC timing becomes more extreme. Increased pumping work only occurs at the most extreme IVC timing, further contributing to the increased fuel consumption of the LIVC100 case.

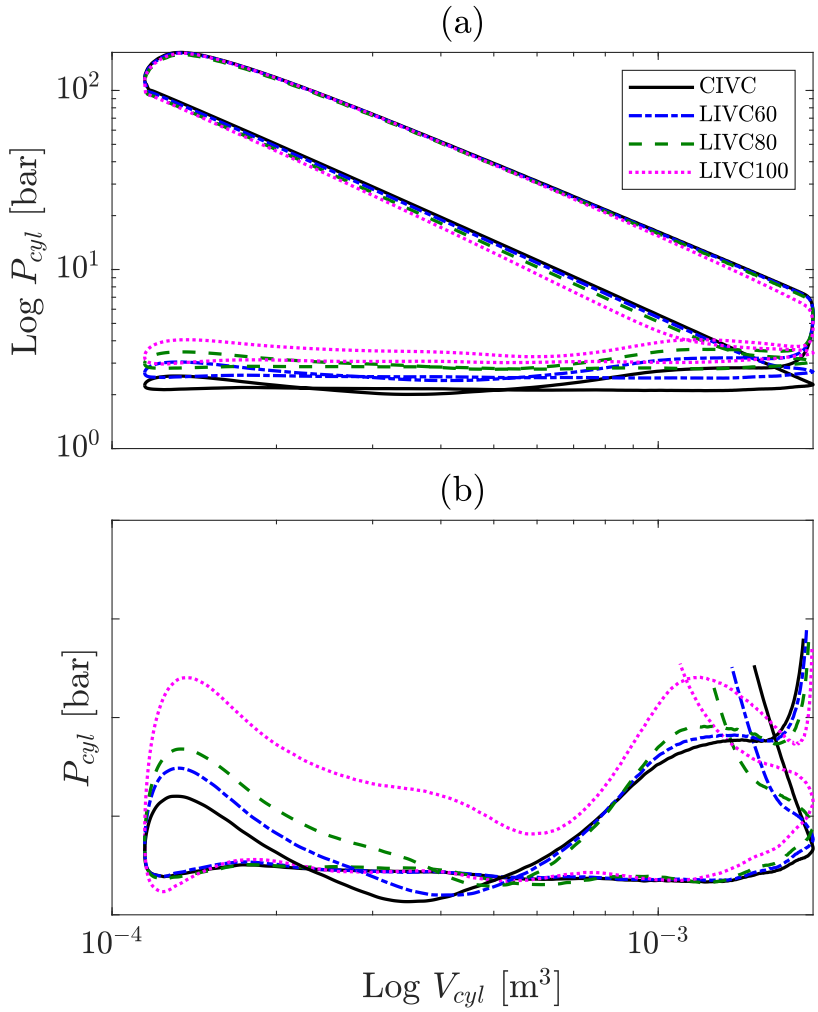

Figure 5.10: (a) The log pressure - log volume diagram and (b) zoomed-in view of the pumping loop for the CIVC and LIVC cases at $\lambda \approx 1.7$. The pumping loops in (b) are offset to highlight relative size differences.

5.4 High Boost and Miller Cycle with a TBC Piston

The analysis conducted in Section 5.3 demonstrated that LIVC strategies, charge composition being equal, significantly reduce NO_x emissions due to lower combustion temperatures. However, very extreme LIVC profiles increase fuel consumption by up to 3%. For that reason, LIVC100 is not considered in this section. Instead, EIVC40 will be considered given the similar behavior to LIVC60 observed in Section 4.5. Additionally, the TBC piston used in Section 5.2 is also utilized in this work.

Figure 5.11a shows the NO_x behavior for the tested IVC profiles as a function of intake manifold pressure. The solid markers correspond to data collected with the uncoated piston and the unfilled markers correspond to data collected with the TBC piston. The dashed red line in Figure 5.11a highlights the cases at the baseline NO_x emission level represented by a red star marker. Kovács and Eilts [32] studied EIVC and LIVC Miller cycle profiles at elevated boost pressures and baseline NO_x levels with the intention of increasing engine output over fuel conversion efficiency. Their experimental approach altered SOI to keep CA50 constant, allowed IMEP to increase, and adjusted the EGR rate for NO_x control, creating compounding effects that resulted in richer charge compositions with Miller cycle. Figure 5.11c and Figure 5.11d show Miller cycle profiles, at identical operating parameters as the CIVC case other than intake manifold pressure, permit leaner charge compositions than CIVC at NO_x emissions parity. The effect of controlling NO_x emissions with Miller cycle-based IVC profiles in an insulated engine on fuel conversion efficiency is analyzed in detail in Section 5.4.1.

Miller cycle strategies have a strong influence on the boundary conditions that define turbocharger boost capabilities, therefore their effect on engine efficiency and emissions must also be considered under a constant η_{TC} constraint. Figure 5.11b shows the η_{TC} behavior for the tested Miller cycle profiles as a function of intake manifold pressure. In Section 5.4.1, the LIVC80 point assumes a 10% absolute increase

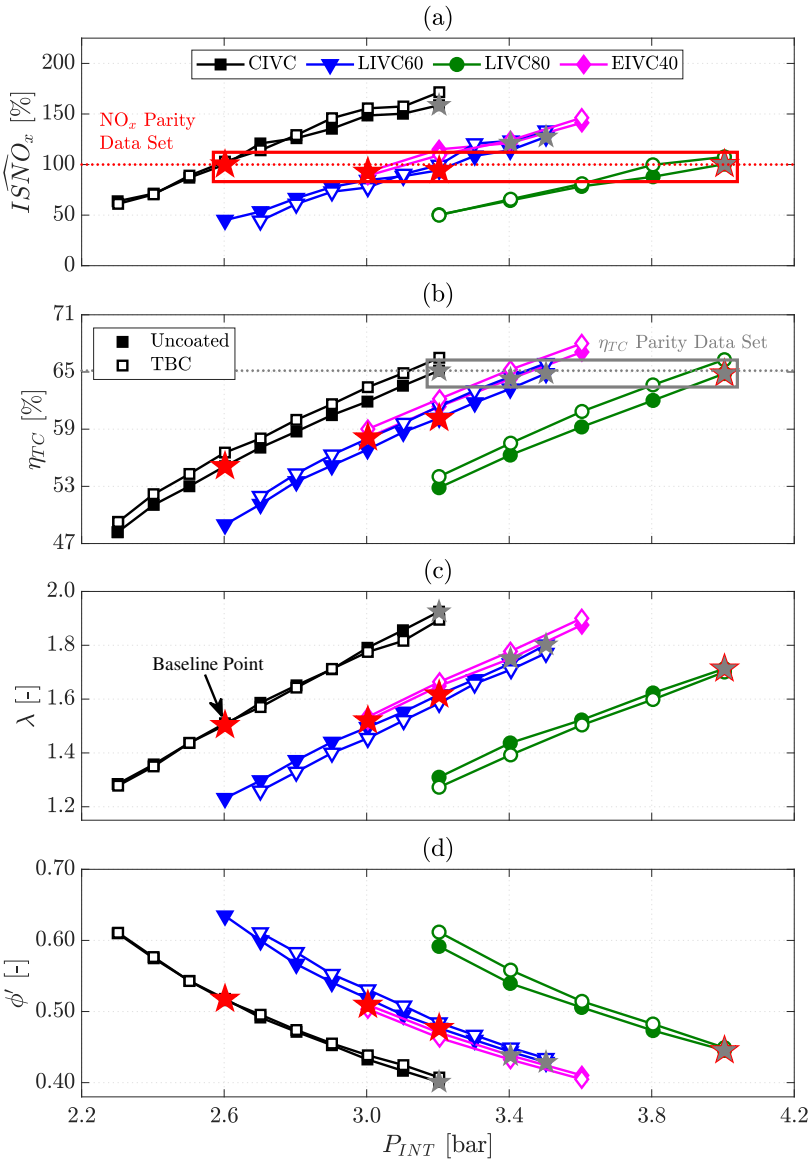

Figure 5.11: Extensive high boost intake manifold pressure sweep and its effect on (a) normalized indicated specific NO_x emissions ($\widehat{ISNO_x}$), (b) overall turbocharger efficiency (η_{TC}), (c) air-to-fuel equivalence ratio (λ) and (d) fuel-to-charge equivalence ratio (ϕ').

in η_{TC} over the CIVC case. Thus it is necessary to investigate how this improved η_{TC} would affect CIVC, LIVC60 and EIVC40 behavior. The grey star markers represent said equivalent η_{TC} scenario and the analysis of their performance is found in Section 5.4.2. The use of a TBC piston elevates the η_{TC} requirement by ≈1% and will be assumed to have a negligible effect on the presented results.

5.4.1 Constant NO_x Emissions Operation

The results of Section 5.3 demonstrate that Miller cycle-based LIVC profiles produce less NO_x than the CIVC case at equivalent cylinder composition, albeit with higher fuel consumption, at the extreme IVC timings. The experiments conducted in this section investigate the pairing of high boost levels and a TBC piston to leverage the NO_x emissions benefit of Miller cycle profiles and remedy the aforementioned fuel consumption issues. All actuator settings were set as outlined in Table 5.1, with Y_{EGR} fixed at 20% and fuel rail pressure set to 125 MPa. Fuel injection pulse width was again adjusted to match the baseline load (nIMEP = 1.76 MPa) and intake manifold pressure was adjusted for each IVC strategy such that $\widehat{ISNO_x} = 100 \pm 11\%$. The intake manifold absolute pressures for each IVC strategy that met this NO_x criteria were CIVC at 260 kPa, LIVC60 at 320 kPa, LIVC80 at 400 kPa, and EIVC40 at 300 kPa.

Figure 5.12 displays the cycle average results for 12 key engine performance metrics as IVC timing deviates from the conventional timing of -164° aTDC, advanced up to -204° aTDC and delayed up to -84° aTDC at constant NO_x, as shown in Figure 5.12a. Figure 5.12b shows the relative change in ISFC with respect to the baseline case. LIVC60 is once again the most efficient point for the uncoated piston, reducing ISFC by 1.3% while LIVC80 improved ISFC by 0.9% and EIVC40 by 0.7%. The TBC piston improved ISFC by 0.7% with CIVC, 1.8% with LIVC60, 1.8% with LIVC80, and 1.2% with EIVC40. Pairing LIVC80 with a TBC piston doubled the ISFC improvement. For the uncoated piston, the LIVC80 case has higher fuel consumption than LIVC60, despite having equivalent gross thermal efficiency (shown in Figure 5.12d) due to increased pumping losses. Gas exchange efficiency decreased with changes to IVC timing, as shown in Figure 5.12c, because of the increase in charge mass pumped through the cylinder for the LIVC cases. The TBC piston improves the gas exchange efficiency of the two LIVC cases, permitting the LIVC80 case to obtain ISFC parity

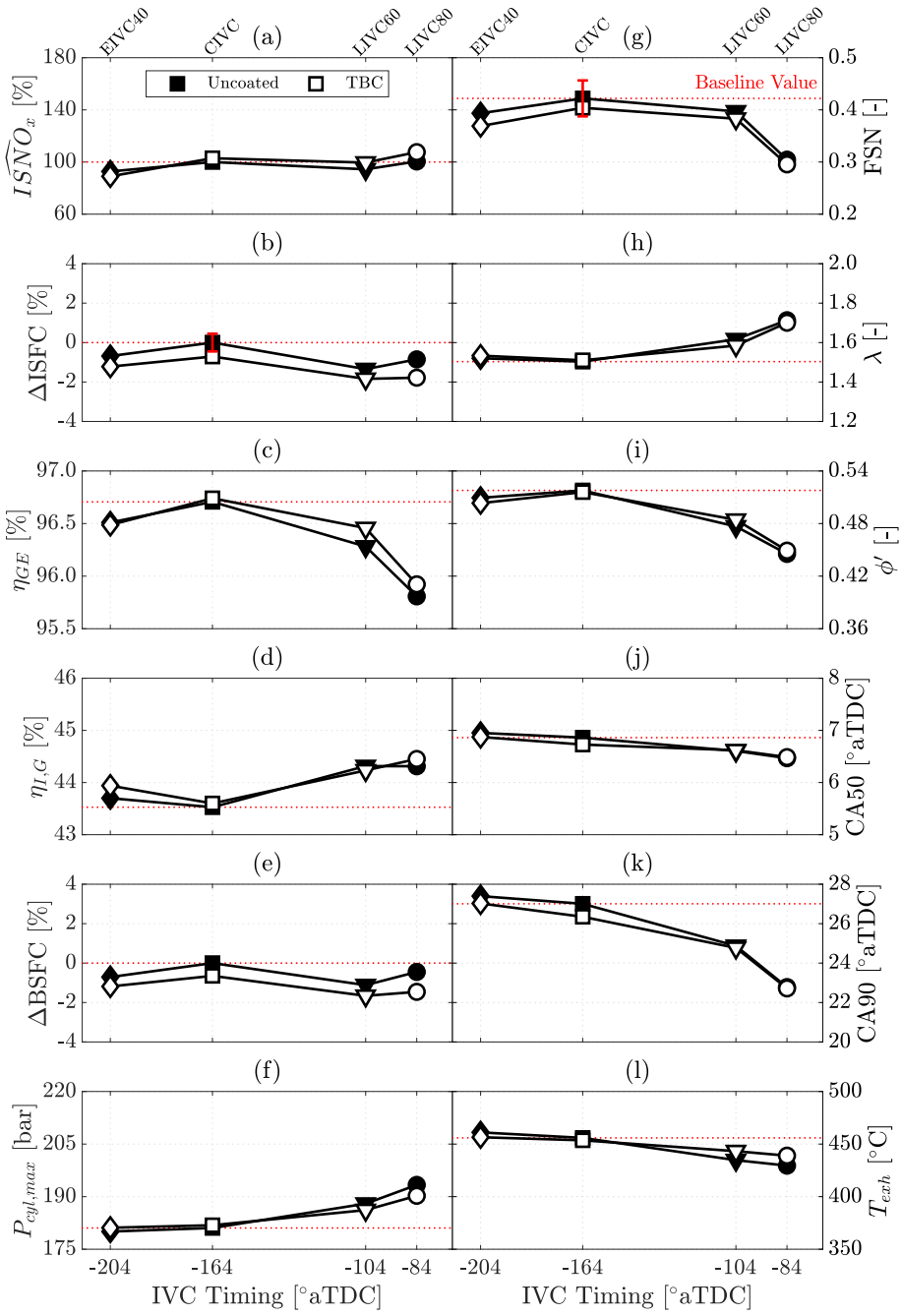

Figure 5.12: (a) Normalized indicated specific NO_x emissions ($\widehat{ISNO_x}$), (b) relative change in ISFC compared to the baseline point (ΔISFC), (c) gas exchange efficiency (η_{GE}), (d) gross thermal efficiency ($\eta_{I,G}$), (e) relative change in BSFC compared to the baseline point (ΔBSFC), (f) peak cylinder pressure ($P_{cyl,max}$), (g) filter smoke number (FSN), (h) air-to-fuel equivalence ratio (λ), (i) fuel-to-charge equivalence ratio (ϕ'), (j) timing of CA50, (k) timing of CA90 and (l) exhaust temperature (T_{exh}) plotted as a function of IVC timing at $\widehat{ISNO_x} \approx 100\%$. The dotted line represents the baseline value of each parameter.

with the LIVC60 case. Kovács and Eilts [32] also examined an LIVC profile with an IVC timing 80 CAD later than the baseline utilizing elevated boost pressures at a prescribed NO_x threshold. Their reported 4% relative ITE improvement is significantly larger than the improvements reported for the uncoated and TBC LIVC80 cases. Their improved performance can be attributed to their optimization of SOI to match CA50 between the baseline and LIVC case as well as reduced EGR rates for the Miller cases that minimize pumping losses.

The air-to-fuel and fuel-to-charge equivalence ratios in Figure 5.12h and Figure 5.12i, respectively, show that the increased charge dilution of later IVC timings at NO_x parity improve PM emissions as shown in Figure 5.12g. EIVC40 does not increase charge dilution, yet still improves PM emissions on a similar magnitude as LIVC60. Given the TBC piston has no impact on dilution, it yields minor, statistically insignificant, improvements in PM emissions. TBCs decrease PM emissions when volumetric efficiency penalties are counteracted by considerably increased combustion gas temperatures that promote soot oxidation [6]. Miller strategies at this NO_x parity constraint affect the two aforementioned requirements for TBCs, resulting in a net neutral effect on PM emissions because the increased dilution minimally impacts exhaust gas enthalpy. Thus, pairing Miller strategies with a TBC mitigates the NO_x-PM tradeoff that limits efficiency improvements in diesel engines.

The fuel consumption benefits obtained with LIVC60 and LIVC80 can be attributed to a shortened combustion duration. While CA50, shown in Figure 5.12j, is not altered significantly by the delayed IVC timings, CA90, shown in Figure 5.12k, advances significantly. The poorer efficiency improvements for the EIVC40 case compared to the LIVC cases can be attributed to the lack of changes to combustion phasing and duration. The TBC piston also does not significantly affect CA50 or CA90, thus efficiency improvements for these cases lie elsewhere.

The relative change in BSFC with respect to the baseline case is shown in Fig-

ure 5.12e. LIVC60 reduces BSFC by 1.1% with the uncoated piston, while LIVC80 only improves BSFC by 0.4% and EIVC40 by 0.7%. The TBC piston improves BSFC for the CIVC case by 0.6%, 1.7% for the LIVC60 case, 1.5% for the LIVC80 case, and 1.2% for the EIVC40 case. BSFC improvement for the LIVC profiles is hindered by elevated peak cylinder pressures, as shown in Figure 5.12f. LIVC profiles minimally decrease exhaust temperatures compared to the CIVC case while EIVC40 has no effect on exhaust temperatures as shown in Figure 5.13l. The TBC piston shows differing behavior with the LIVC cases as it operated at slightly lower peak pressures, reducing friction losses, and raised exhaust temperatures by ≈10°C.

As before, Figure 5.13 provides a breakdown of the energy pathways for each IVC strategy. As shown in Section 5.3, LIVC profiles operating at constant λ decrease heat transfer losses. Given the prescribed NO_x threshold, delaying IVC timing allowed for an increasingly dilute cylinder charge. The combination of increased dilution and LIVC operation leads to substantially reduced heat transfer losses. The EIVC40 case reduced heat transfer losses to a lesser extent than the LIVC cases because it did not increase dilution. The TBC piston reduced heat transfer losses across all cases, with the LIVC80 case experiencing the most significant complementary effect. The reduced peak cylinder temperatures from utilizing Miller IVC strategies shown in Figure 5.14a paired with shorter combustion duration result in lower heat transfer losses. Figure 5.14c shows the TBC piston had no effect on peak combustion temperatures or duration, meaning reduced heat transfer losses are a product of the insulative properties of the piston coating. Only the LIVC80 strategy meaningfully elevates EXMEP over the CIVC case, primarily due to similar exhaust temperatures maintained at a much higher mass air flow rate. All of the TBC cases experience a reduction in exhaust losses.

The increased PMEP and FMEP losses are not as impactful to the overall fuel conversion efficiency of the Miller cycle strategies as the heat transfer and exhaust

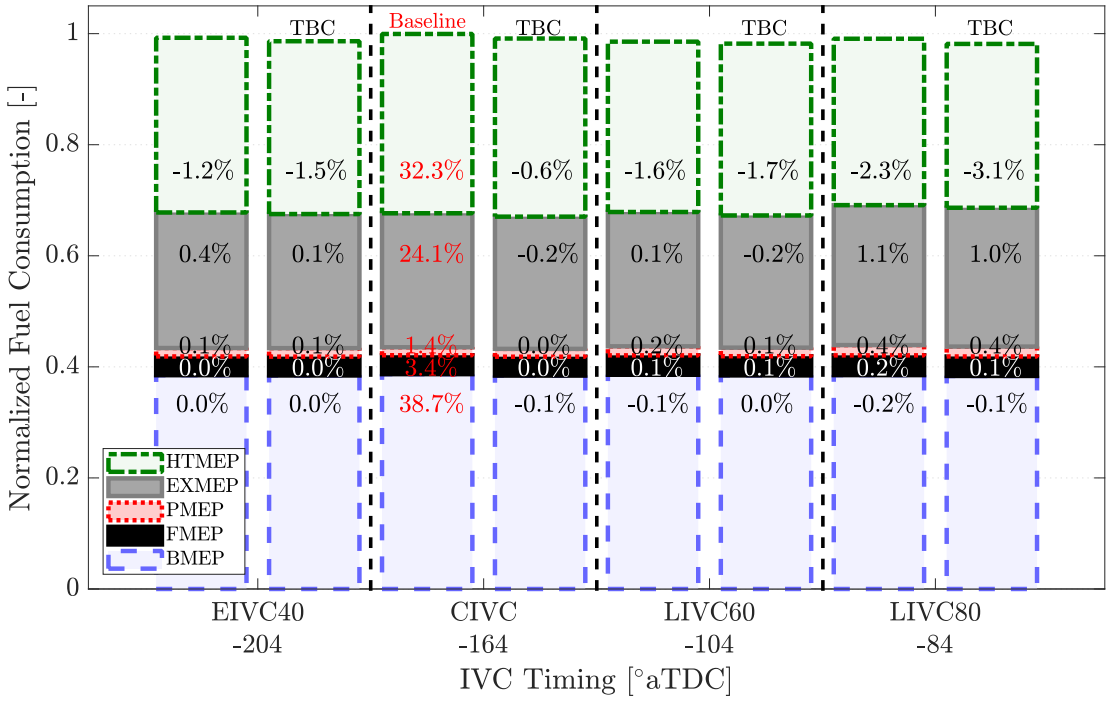

Figure 5.13: Energy breakdown for each IVC timing strategy at $\widehat{ISNO_x} \approx 100\%$.

losses. With the uncoated piston, LIVC60 has the optimal balance of heat transfer benefits and exhaust, pumping, and friction losses that allow for superior fuel consumption over the other cases. The heat transfer and exhaust tradeoff of the Miller cycle profiles is shifted with the TBC piston such that LIVC80 operates at the lowest ISFC and PM emissions.

NO_x parity of the Miller cycle profiles at more dilute conditions than the CIVC case is enabled by leveraging the lower combustion temperatures of Miller cycle profiles discussed in Section 5.3. The counteracting effect of decreased combustion temperatures and increased in-cylinder oxygen content on NO_x emissions enables the increased in-cylinder oxygen, via increased boost, shown in Figure 5.14a. The lower pre-combustion temperatures also contribute to the elevated premixed heat release observed in Figure 5.14b. The TBC piston had no effect on these trends.

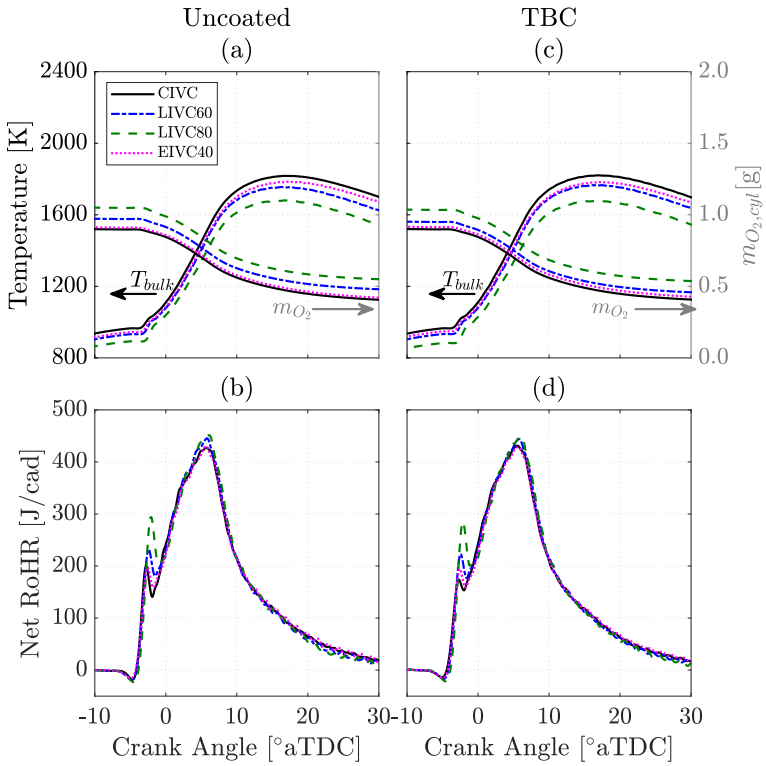

Figure 5.14: The (a) bulk cylinder temperature, in-cylinder O_2 mass and (b) net rate of heat release during combustion for the uncoated CIVC and Miller cycle cases and the (c) bulk cylinder temperature, in-cylinder O_2 mass and (d) net rate of heat release during combustion for the TBC CIVC and Miller cycle cases at $\widehat{ISNO_x} \approx 100\%$.

5.4.2 Constant η_{TC} Operation

This section analyzes the effect of Miller cycle intake profiles on the combustion process when constrained to the same η_{TC} as for the CIVC case. The comparisons made in Section 5.4.1 imply a more efficient turbocharger is available to be paired with the Miller cycle strategies only, which is necessary for maintaining their elevated intake manifold pressures. In this case, η_{TC} is fixed at that of the high boost CIVC case studied in Section 5.2, as this constraint will fairly determine which Miller cycle strategy achieves the lowest fuel consumption under elevated boost conditions. All actuator settings were as set previously, except intake manifold pressure was adjusted such that $\eta_{TC} = 65.4 \pm 1.1\%$. The intake manifold absolute pressures for each IVC strategy that met these η_{TC} criteria were CIVC at 320 kPa, LIVC60 at 350 kPa,

LIVC80 at 400 kPa, and EIVC40 at 340 kPa.

Figure 5.15 displays the cycle average results for 12 key engine performance metrics as IVC timing deviates from the conventional timing of -164° aTDC, advanced up to -204° aTDC and delayed up to -84° aTDC at constant η_{TC}. Figure 5.15a shows the impact constant η_{TC} has on NO_x emissions, with the uncoated CIVC case experiencing a 59% increase over the baseline case. LIVC60 and LIVC80 increased NO_x emissions by 27% and 0% respectively, while EIVC40 increased NO_x by 21%. NO_x emissions for the TBC piston are negligibly higher, with CIVC increasing NO_x output by an additional 13%, LIVC60 and LIVC80 increase it another 6% and 8% respectively, while EIVC40 experiences only a 3% increase. The increased NO_x output is directly attributed to the increase in air-to-fuel and fuel-to-charge equivalence ratios shown in Figure 5.15h and 5.15i, respectively. At constant η_{TC}, Miller cycle intake profiles will typically have a richer charge than the CIVC case due to their lower VE, as shown in Chapter IV, leaving the CIVC case at a NO_x emission disadvantage. Inversely, Figure 5.15g shows the CIVC case has the lowest FSN. However, all cases significantly reduce PM emissions given the leaner charge composition than the baseline. The TBC piston again does not have a meaningful effect on PM emissions.

Figure 5.15b shows the relative change in ISFC compared to the baseline point. LIVC60 no longer outperforms the CIVC case, with the former reducing ISFC by 2.0% and the latter by 2.4%. EIVC40 is the next most efficient case with a 2.3% improvement in ISFC. Delaying IVC timing beyond 60 CAD results in much smaller improvements, as LIVC80 only reduces ISFC by 0.9%. LIVC60 benefits most from the TBC piston, as it gains an additional 1.0% ISFC improvement, followed by a 0.9% increase for the LIVC80 case, a 0.6% improvement for the CIVC case, and finally the smallest improvement of 0.5% for the EIVC40 case. Gas exchange efficiency remains approximately constant with changes in IVC timing and the use of a TBC, as shown in Figure 5.15c. However, the decrease in gross thermal efficiency shown in Figure 5.15d

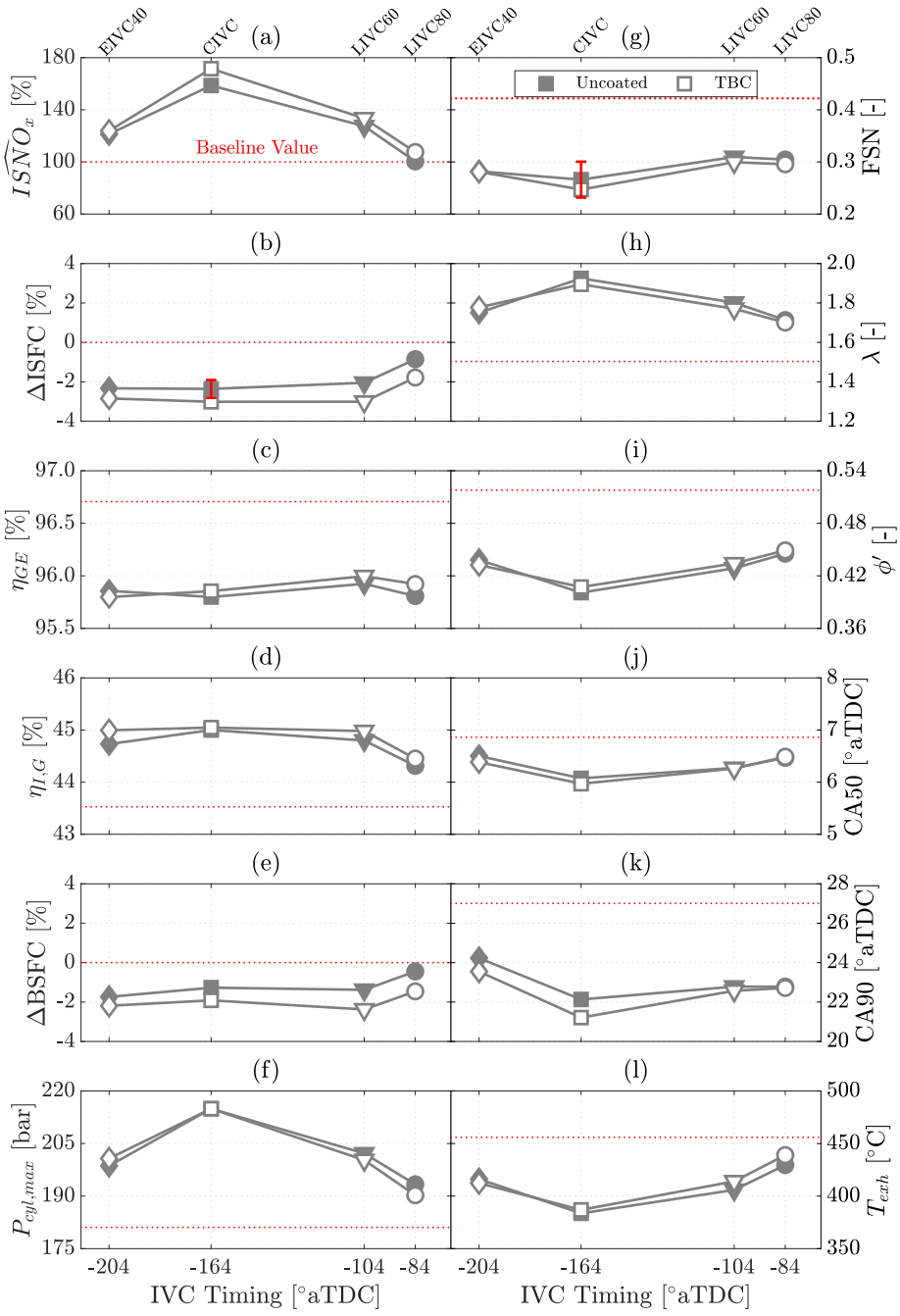

Figure 5.15: (a) Normalized indicated specific NO_x emissions ($\widehat{ISNO_x}$), (b) relative change in ISFC compared to the baseline point (ΔISFC), (c) gas exchange efficiency (η_{GE}), (d) gross thermal efficiency ($\eta_{I,G}$), (e) relative change in BSFC compared to the baseline point (ΔBSFC), (f) peak cylinder pressure ($P_{cyl,max}$), (g) filter smoke number (FSN), (h) air-to-fuel equivalence ratio (λ), (i) fuel-to-charge equivalence ratio (ϕ'), (j) timing of CA50, (k) timing of CA90 and (l) exhaust temperature (T_{exh}) plotted as a function of IVC timing at $\eta_{TC} \approx 65.4\%$. The dotted line represents the baseline value of each parameter.

grows significantly at IVC timings delayed more than 60 CAD. The TBC piston mitigates these penalties for the EIVC40 and LIVC60 cases. These results highlight the importance of the η_{TC} metric in Miller cycle applications, given that studies in the literature report improved fuel consumption with LIVC strategies without sufficient consideration of turbocharger boundary conditions. Guan et al. [39] for example reports a significant 1.5% improvement in fuel conversion efficiency for an optimum LIVC case utilizing elevated intake manifold pressures using only a constant pressure differential across the engine to assess turbocharger performance.

Given the variable cylinder composition, the peak cylinder pressures decreased substantially with changes to IVC timing, as shown in Figure 5.15f. The peak cylinder pressures for the high boost CIVC case are 34 bar higher than that of the baseline case. Those obtained with LIVC60 and LIVC80 are only 21 and 12 bar higher, respectively. The peak cylinder pressure of the EIVC40 case is only 18 bar higher than the baseline case. The TBC piston once again operated at slightly lower peak pressures for the LIVC cases only. Figure 5.15e shows the relative change in BSFC compared to the baseline point. The larger friction losses for the uncoated CIVC case permit LIVC60 to have equivalent BSFC despite worse ISFC. EIVC40, however, netted the lowest BSFC for the uncoated cases with a 1.7% improvement over the baseline case. For the TBC pistons, BSFC was lowest with LIVC60 at a 2.4% reduction over the baseline case, followed by a 2.2% improvement for the EIVC40 case, a 1.9% improvement for the CIVC case, and finally a 1.5% improvement for the LIVC80 case. As shown in Figure 5.15l, the uncoated LIVC60 and LIVC80 cases reduced exhaust temperatures by 50°C and 26°C over the baseline case, respectively, and the EIVC40 case reduced exhaust temperatures by 40°C. Meanwhile the high boost CIVC case reduced exhaust temperatures by 72°C. The TBC piston only affected the exhaust temperatures of the LIVC cases, raising them both by ≈10°C over their uncoated counterparts. While still existent, the issue with elevated NO_x emissions, cylinder

pressures and low exhaust temperatures identified in Section 5.2 are significantly diminished with the combined use of Miller cycle profiles and a TBC coating, without compromising fuel consumption or PM emissions.

Figure 5.16 again presents the total fuel energy utilized by each IVC strategy to match the baseline load. Whereas utilizing Miller cycle profiles should reduce heat transfer losses over the CIVC case, the prescribed η_{TC} constraint counteracts that benefit due to poorer thermodynamic properties from operating at a lower air-to-fuel equivalence ratio and higher fuel-to-charge equivalence ratio. While the EIVC40 case does not increase heat transfer losses over the CIVC case, LIVC60 and LIVC80 do. However, the TBC piston Miller cycle cases all decrease heat transfer losses.

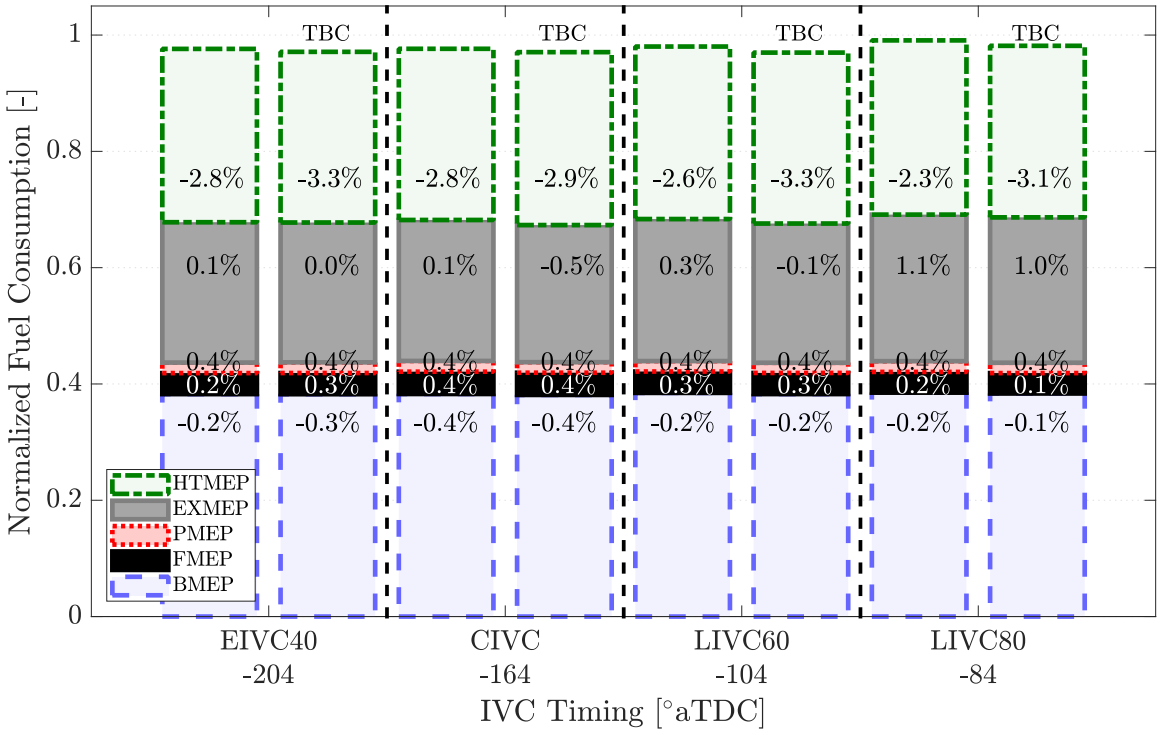

Figure 5.16: Energy breakdown for each IVC timing strategy at $\eta_{TC} \approx 65.4\%$.

Figure 5.17a displays the mass-averaged cylinder temperature, where peak combustion temperatures remain constant regardless of IVC timing. This change in combustion behavior is due to the reduced in-cylinder mass of the Miller cycle cases being subjected to the same engine load as the CIVC case. This lower in-cylinder mass,

combined with slightly extended combustion duration (see Figure 5.15k), negates the heat transfer benefits of the uncoated Miller cycle cases. Figure 5.17c shows that the TBC piston had no significant effect on the combustion temperatures. As before, retarding IVC beyond LIVC60 with the uncoated piston favored the diversion of fuel energy to the exhaust stream over increased work output. With the TBC piston however, this heat transfer-exhaust loss tradeoff was again shifted such that no additional heat transfer reduction resulted in increased exhaust energy.

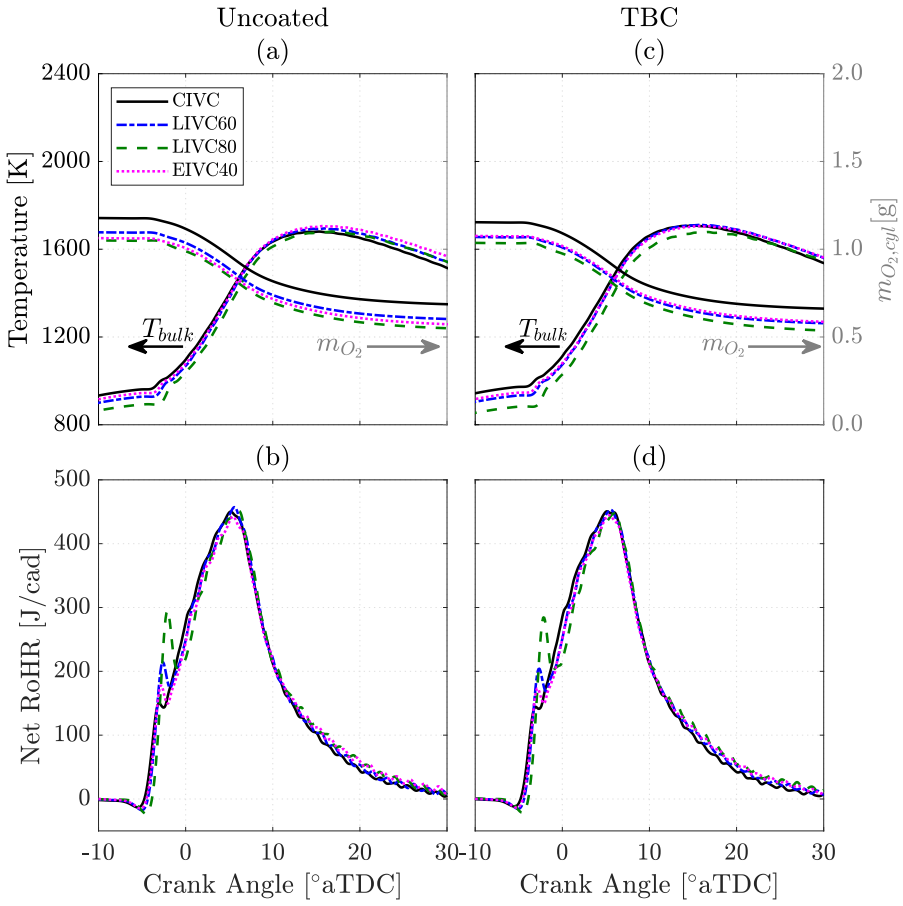

Figure 5.17: The (a) bulk cylinder temperature, in-cylinder O_2 mass and (b) net rate of heat release during combustion for the uncoated CIVC and Miller cycle cases and the (c) bulk cylinder temperature, in-cylinder O_2 mass and (d) net rate of heat release during combustion for the TBC CIVC and Miller cycle cases at $\eta_{TC} \approx 65.4\%$.

Figure 5.17a also shows that the NO_x benefit associated with the Miller cycle profiles is due only to lower in-cylinder O_2 concentration for these η_{TC} parity points,

given the similar peak combustion temperatures. Guan et al. [38] demonstrated similar NO_x emission benefits with Miller cycle operation also as a result of lower in-cylinder air mass and reduced initial burned zone gas temperature. Figure 5.17c shows the TBC piston had a negligible effect on in-cylinder O_2 concentration, and thus no effect on NO_x emissions. Figure 5.17b and Figure 5.17d again show that the TBC piston had no significant effect on the heat release characteristics.

5.5 Summary and Conclusions

This chapter presents an experimental investigation of the effect of extreme Miller cycle-based late intake valve profiles paired with elevated boost pressures and a TBC piston on the combustion process, emissions, and thermal efficiency in a single cylinder heavy-duty research engine equipped with a fully-flexible hydraulic valve train. Miller cycle was achieved using a suite of LIVC profiles with IVC timings ranging from 60 CAD to 100 CAD after the nominal timing and an EIVC profile with an IVC timing of 40 CAD earlier than the nominal timing. The experiments were carried out at a fixed engine load of 1.76 MPa nIMEP at 1160 RPM with a fixed start of injection timing at 6.7° bTDC. Controlled manipulation of intake manifold pressures and intake valve closing timings yielded the following observations:

- The use of elevated intake manifold pressures with the conventional intake valve closing strategy improved brake specific fuel consumption, at the expense of elevated peak cylinder pressures, increased NO_x emissions, and decreased exhaust temperatures.
  - The thermal efficiency improvements were primarily attributed to better thermodynamic properties of the mixture due to air dilution and shorter overall combustion duration resulting in more expansion work.

  - Increasing boost pressure yielded diminishing returns on brake fuel consumption improvements, due to increased friction losses caused by higher cylinder pressures.
  - Utilizing a TBC piston under these high intake manifold pressures further improved brake specific fuel consumption, but also exacerbated the issue of increased NO_x emissions.
    * Modulating Y_{EGR} did not reveal an opportunity for the TBC piston to significantly reduce heat transfer losses relative to the uncoated piston.

- The use of extreme Miller cycle strategies at fixed composition led to reduced heat transfer losses and higher exhaust heat losses, compared to the conventional IVC case. Utilizing LIVC strategies only benefited fuel consumption within a narrow IVC timing range.
  - Miller cycle profiles reduced NO_x emissions and heat transfer losses relative to the conventional IVC strategy due to lower combustion temperatures stemming from lower end-of-compression temperatures caused by lower effective compression ratios.
  - As more aggressive Miller strategies were used, exhaust losses increased at a greater rate than heat transfer losses decreased. This created a tradeoff resulting in an optimum for brake specific fuel consumption at an IVC timing 60 CAD later than conventional.
  - Miller cycle strategies required a more efficient turbocharger system to maintain a similar composition with the conventional IVC case.

- The combined use of high intake boost and extreme Miller cycle offers reduced friction losses, reduced NO_x emissions and elevated exhaust enthalpy over conventional intake valve profiles, without compromising BSFC or PM emissions.

- When constrained by a low NO_x threshold, Miller cycle strategies operated under much leaner conditions, offering superior fuel consumption and PM emissions over conventional IVC case. However, the η_{TC} requirement of the Miller cycle cases exceeded those of the conventional IVC case.
    - The Miller cycle-TBC combination demonstrated a novel improvement to the NO_x-PM tradeoff of diesel engines. The TBC piston shifted the heat transfer and exhaust tradeoff of the Miller cycle profiles such that the most extreme Miller cycle profile obtained a simultaneous 1.8% ISFC and 43% PM emissions reduction.
- At equivalent, high η_{TC}, the optimum IVC timing is 40 CAD earlier than conventional under the conditions investigated for the uncoated piston. This optimum exists due to the tradeoff between operating at unfavorable thermodynamic properties and reducing heat transfer losses. This balance minimizes any decrease in thermal efficiency such that fuel consumption is on par with an equivalent high η_{TC} conventional IVC case, but with 20% lower NO_x emissions.
    - The TBC piston again shifts the heat transfer and exhaust tradeoff of the Miller cycle profiles such that the optimum IVC timing is 60 CAD later than conventional, obtaining a simultaneous 0.5% BSFC and 20% NO_x emissions improvement over an equivalent high η_{TC} conventional IVC case.

This study demonstrated the effects of Miller cycle on the combustion process in a single cylinder research engine utilizing both an uncoated and TBC piston. Further experiments should be conducted on a production engine to validate the effect of the Miller cycle profiles on turbocharger and exhaust aftertreatment system performance. The η_{TC} calculations used in this study are meant to predict real engine behavior,

but behavior in a multi-cylinder engine may be different due to the pulsating flow and cylinder-to-cylinder interaction in the intake and exhaust manifolds. The presence of a TBC can also have a much different influence on volumetric efficiency when utilized in a multi-cylinder engine. From Chapter III, TBC performance was found to be highly dependent on operating condition, as such the trends observed in this work must be validated across the entire engine map. The effect that the change in exhaust temperatures and enthalpy will have on a real exhaust aftertreatment system should be considered in order to rigorously evaluate the impact that each IVC profile will have on tailpipe NO_x emissions given the present study only considers engine-out emissions.

CHAPTER VI

Conclusions and Recommendations

6.1 Summary of Dissertation

This dissertation has presented an experimental investigation of the novel combination of a wave bowl piston with thermal barrier coatings and Miller cycle valve strategies. The results show that the wave bowl geometry enables this combination to improve fuel consumption, steady-state engine-out NO_x emissions, and particulate matter emissions, essentially improving the NO_x-particulate matter tradeoff that plagues diesel engine efficiency. The aforementioned benefits are achieved at the expense of elevated turbocharger efficiency requirements.

Chapter III investigated the effect of coating the wave piston crown with a thermal layer on the combustion process, emissions, and thermal efficiency in a single cylinder heavy-duty research engine. Three thermal barrier coatings of varying composition and thickness were studied at seven operating conditions representative of a broad range of the engine's speed-torque map. This study provided the understanding that TBC performance was highly dependent on volumetric efficiency, as cases with decreased volumetric efficiency increased the heat transfer gradient between the combustion gasses and the combustion chamber. While the temperature swing characteristics of each coated piston, engine load, and engine speed determined volumetric efficiency, the insulative properties of each coating were what determined

whether the aforementioned change in heat transfer gradient would impact fuel conversion efficiency. The thinner of the two PEA TBCs consistently yielded smaller decreases in volumetric efficiency and statistically insignificant changes in ISFC. The thicker PEA TBC yielded up to a 0.6% increase in ISFC due. Additionally, the soot oxidation impacts of the wave piston were found to be diminished by operation at higher engine speeds, with the lowest increase in PM emissions with the coated pistons observed at the low speed conditions. The findings of this chapter motivated the use of the low speed-medium load operating condition in Chapters IV and V.

In Chapter IV, the effect of Miller cycle on the combustion process, emissions, and thermal efficiency was investigated in a single cylinder heavy-duty research engine equipped with a fully-flexible hydraulic valvetrain. Miller cycle operation at the low speed-medium load condition was achieved using a suite of EIVC and LIVC profiles ranging from up to 60 CAD before to up to 80 CAD after the nominal IVC timing, respectively. Miller cycle profiles of equivalent volumetric efficiency reduction were found to cause similar changes in combustion characteristics and emissions. The implementation of an overall turbocharger efficiency metric clarified the source of discrepancies found in the current body of work on Miller cycle, as studies reporting increased fuel consumption were typically underutilizing their boost capabilities while those reporting significant efficiency improvements were exceeding boost capabilities. This novel analysis of Miller cycle performance at equivalent turbocharger efficiency to a conventional baseline showed that an 8% relative increase in turbocharger efficiency is required for Miller cycle profiles to reduce peak cylinder pressures and elevate exhaust temperatures without increasing BSFC or particulate matter emissions.

Finally, in Chapter V, the optimal coated wave piston from Chapter III and the optimal Miller cycle intake valve profiles from Chapter IV were utilized in conjunction under high boost conditions based on the low speed-medium load condition of Chapter III. The use of extreme Miller cycle strategies at fixed composition creates

a tradeoff between reduced heat transfer losses and elevated exhaust heat losses that only improved fuel consumption within a narrow IVC timing range, 60 CAD later than conventional under the tested conditions. This study provided the novel insight that the use of variable EGR rates for NO_x control, such as in Chapter IV, suppress the benefits of the inherent low NO_x operation of Miller cycle applications. By increasing boost pressures to maintain NO_x parity, the optimal Miller cycle strategy, LIVC60, operates under much leaner conditions, offering a simultaneous 1.3% reduction in ISFC and small 6% decrease in PM emissions over the conventional IVC case. Using a TBC piston shifts the heat transfer and exhaust loss tradeoff of the Miller cycle profiles such that the optimum IVC timing is 20 CAD more extreme than with the uncoated case, increasing the ISFC improvement to 1.8% and the PM emissions reduction to 30%. However, these improvements require the Miller cycle cases to exceed the turbocharger efficiency of the conventional IVC case by up to 10% (absolute) at the most extreme timing. At equivalent high turbocharger efficiencies, Miller cycle strategies maintain fuel consumption parity to the conventional IVC case at 31% lower NO_x emissions due to the robust efficiency of Miller cycle profiles at richer cylinder composition that stems from their innate ability to reduce heat transfer losses. Using a TBC piston again shifts the optimum IVC timing compared with the uncoated case, doubling BSFC improvements without compromising NO_x or particulate matter emissions.

6.2 Future Research Questions

The future work recommended to address the limitations of the single cylinder configuration of our research engine have been addressed in the respective conclusion sections of Chapters III, IV, and V. The following recommendations aim to expand upon the scope and impact of the work presented in this dissertation.

This work has focused on isolating the underlying, fundamental behavior of Miller

cycle strategies. Thus, most all operating parameters were intentionally fixed. The impact of the presented Miller cycle work could benefit from the optimization of those operating parameters, specifically timing and quantity of fuel injections. Reducing the magnitude of the heat release during the premixed burn portion of combustion, occurring prior to TDC, should help increase the efficiency of the more extreme Miller cycle profiles.

The turbocharger efficiency of a real device depends on a plethora of variables, many more than those used in this study to estimate turbocharger performance. The turbocharger efficiency evaluations presented in this study are meant to motivate future research efforts to prioritize thorough turbocharger system evaluations when investigating the real world implications of high boost Miller cycle applications. Furthermore, this work relies on the assumption that high boost capabilities will be obtainable at the low speed condition examined. Interest in electrically assisted boosting systems, or eTurbos, for heavy-duty diesel applications is increasing rapidly due to their appeal for increasing low-speed torque [80]. As such, conducting studies with an electronically assisted turbo under both steady-state and transient conditions would add tremendous value to the existing body of work on Miller cycle applications.

The effect the change in exhaust temperatures and enthalpy from Miller cycle applications will have on an exhaust aftertreatment system should be considered to rigorously evaluate the impact the reported NO_x emission improvements from Miller cycle will have on tailpipe NO_x emissions and urea consumption. Recent studies have shown the importance of considering total fluid consumption, defined as $\dot{m}_{fuel}+\dot{m}_{urea}$, when determining the lowest total cost of ownership [37–39]. As these studies estimate the reduction in urea consumption, their claims merit experimental validation with a real exhaust aftertreatment system. Additionally, though EGR modulation for NO_x was shown to be less beneficial to decreasing fuel consumption compared to modulating intake boost pressures, leveraging the NO_x benefit of Miller cycle profiles

to significantly reduce the EGR demand and extend the useful life of the engine's EGR cooler would justify pursuing EGR cooler fouling studies under Miller cycle operation.

Finally, the surface roughness and porosity of TBC B and C (from Chapter III) should be examined and compared to that of the baseline wave piston, as the slow combustion rates of TBC C across all test conditions are indicative of slower flame speeds along the piston wall reducing combustion speed [81, 82]. Given TBC B and C do not alter combustion phasing, and only TBC C extends combustion duration, it is likely the PEA process increases permeable porosity as the thermal layer grows thicker. Permeable porosity is the phenomena in which the pores of a TBC surface trap combustion gasses, acting as a crevice volume that absorbs heat or traps unburned fuel for a significant portion of combustion [64]. Repeating these experiments with both intentionally more porous and sealed, to reduce porosity, variants of TBC B and TBC C would make for a novel, informative study aimed at understanding the effect of TBC porosity on combustion in a heavy-duty diesel engine.

6.3 Closing Statement

With the looming introduction of fully-electric heavy-duty vehicles, I will conclude by saying that the internal combustion engine is not dead yet. The thorough investigation of TBCs and Miller cycle strategies with this engine point to opportunities to enhance the fuel conversion efficiency and NO_x emissions of heavy-duty diesel engines that will only benefit from increased electrification. Whether implemented as a fixed or variable valve timing strategy in the next generation of heavy-duty diesel engines, Miller cycle has shown the necessary merit for on-road applications. TBCs will play an important role in maximizing the fuel conversion efficiency of those Millerized heavy-duty engines. These engines can maintain a prominent role in the transportation industry despite increasingly stringent emissions mandates by incor-

porating electrified auxiliaries, such as electric EGR pumps or eTurbos, to maximize the benefits and address the caveats of the TBCs and Miller cycle strategies presented in this thesis.

APPENDIX

APPENDIX A

Uncertainty Analysis

The 95% confidence interval, denoted by error bars in select plots, was calculated using two distinct methods. Errors in cylinder pressure and fuel flow measurements used to determine indicated specific fuel consumption (ISFC) were calculated using the zeroth-, first-, and Nth-order uncertainty analysis outlined in [83]. An example of the resulting error bounds for the pressure trace is presented in Figure A.1. The 95% confidence interval for ISFC itself was then calculated utilizing the maximum cylinder pressure bounds and minimal fuel flow bounds to determine the minimum ISFC bound, and vice versa for the upper ISFC bound.

Emissions data, specifically filter smoke number and NO_x emissions, had their 95% confidence interval calculated utilizing the standard error formula for a two-tailed distribution, as shown in Equation A.1.

$$95\%\ \text{CI} = \bar{x}\ \pm\ t\frac{\sigma}{\sqrt{n}} \tag{A.1}$$

where $\bar{x}$ is the mean value, σ is the standard deviation, n is the number of samples, and t is the t-score value for 95% confidence corresponding to n samples.

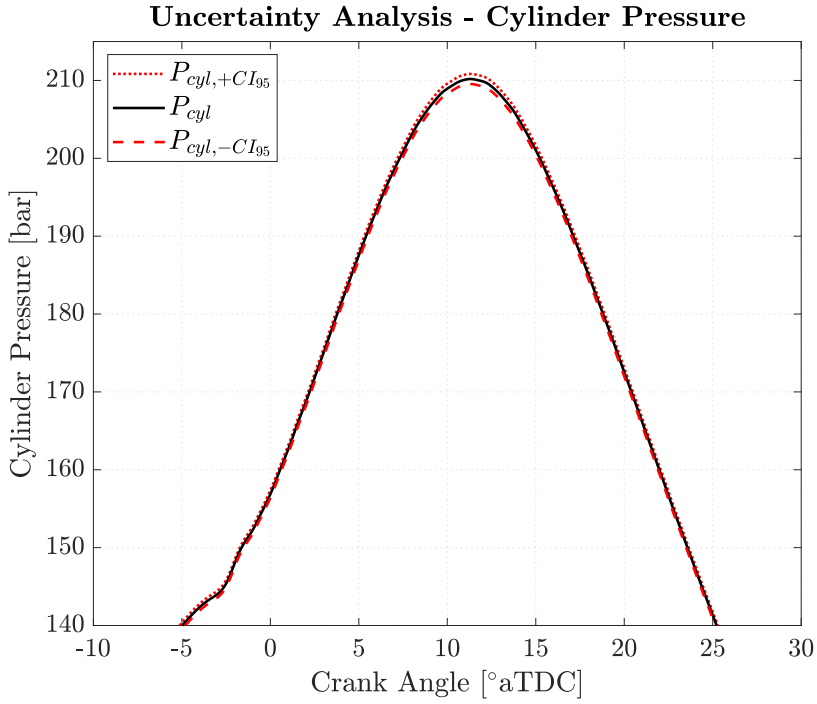

Figure A.1: Zeroth-, first-, and Nth-order uncertainty analysis was used to form the 95% confidence interval for the cylinder pressure trace.

BIBLIOGRAPHY

BIBLIOGRAPHY

[1] "Fast Facts: U.S. Transportation Sector Greenhouse Gas Emissions, 1990-2019," Environmental Protection Agency, https://nepis.epa.gov/Exe/ZyPDF.cgi?Dockey=P10127TU.pdf

[2] "Annual Energy Outlook 2020 with Projections to 2050," U.S. Energy Information Administration, https://www.eia.gov/outlooks/aeo/pdf/AEO2020%20Full%20Report.pdf

[3] Amar, P. and Li, J., 2020, *Volvo SuperTruck 2 Pathway to Cost-Effective Commercialized Freight Efficiency*, U.S. Department of Energy Vehicle Technologies Office Annual Merit Review.

[4] Caton, J. A., 2018, "Maximum efficiencies for internal combustion engines: Thermodynamic limitations," International Journal of Engine Research, **19**(10), pp. 1005–1023.

[5] Bryzik, W. and Kamo, R., 1983, "TACOM/Cummins Adiabatic Engine Program," SAE Transactions, **92**, pp. 1063–1087.

[6] Vittal, M., Borek, J. A., Marks, D. A., Boehman, A. L., Okrent, D. A., and Bentz, A. P., 1999, "The Effects of Thermal Barrier Coatings on Diesel Engine Emissions," Journal of Engineering for Gas Turbines and Power, **121**(2), pp. 218–225.

[7] Wakisaka, Y., Inayoshi, M., Fukui, K., Kosaka, H., Hotta, Y., Kawaguchi, A., and Takada, N., 2016, "Reduction of Heat Loss and Improvement of Thermal Efficiency by Application of "Temperature Swing" Insulation to Direct-Injection Diesel Engines," SAE International Journal of Engines, **9**(3), pp. 1449–1459.

[8] Amann, C. A., 1988, "Promises and Challenges of the Low-Heat-Rejection Diesel," Journal of Engineering for Gas Turbines and Power, **110**(3), pp. 475–481.

[9] Caputo, S., Millo, F., Cifali, G., and Pesce, F. C., 2017, "Numerical Investigation on the Effects of Different Thermal Insulation Strategies for a Passenger Car Diesel Engine," SAE International Journal of Engines, **10**(4), pp. 2154–2165.

[10] Afify, E. M. and Klett, D. E., "The Effect of Selective Insulation on the Performance, Combustion, and NO Emissions of a DI Diesel Engine," SAE Technical Paper No. 960505, 1996.

[11] Assanis, D., Wiese, K., Schwarz, E., and Bryzik, W., 1991, "The Effects of Ceramic Coatings on Diesel Engine Performance and Exhaust Emissions," SAE Transactions, **100**, pp. 657–665.

[12] Yan, Z., Gainey, B., Gohn, J., Hariharan, D., Saputo, J., Schmidt, C., Caliari, F., Sampath, S., and Lawler, B., 2020, "The Effects of Thick Thermal Barrier Coatings on Low-Temperature Combustion," SAE International Journal of Advances and Current Practices in Mobility, **2**(4), pp. 1786–1799.

[13] Gingrich, E., Tess, M., Korivi, V., Schihl, P., Saputo, J., Smith, G. M., Sampath, S., and Ghandhi, J., 2021, "The impact of piston thermal barrier coating roughness on high-load diesel operation," International Journal of Engine Research, **22**(4), pp. 1239–1254.

[14] Powell, T., O'Donnell, R., Hoffman, M., Filipi, Z., Jordan, E. H., Kumar, R., and Killingsworth, N. J., 2021, "Experimental investigation of the relationship between thermal barrier coating structured porosity and homogeneous charge compression ignition engine combustion," International Journal of Engine Research, **22**(1), pp. 88–108.

[15] Andruskiewicz, P., Najt, P., Durrett, R., and Payri, R., 2018, "Assessing the capability of conventional in-cylinder insulation materials in achieving temperature swing engine performance benefits," International Journal of Engine Research, **19**(6), pp. 599–612.

[16] Uchida, N., 2020, "A review of thermal barrier coatings for improvement in thermal efficiency of both gasoline and diesel reciprocating engines," International Journal of Engine Research. Advance online publication.

[17] O'Donnell, R., Powell, T., Hoffman, M., Jordan, E., and Filipi, Z., 2017, "Inverse Analysis of In-Cylinder Gas-Wall Boundary Conditions: Investigation of a Yttria-Stabilized Zirconia Thermal Barrier Coating for Homogeneous Charge Compression Ignition," Journal of Engineering for Gas Turbines and Power, **139**(10), 102808.

[18] Uchihara, K., Ishii, M., Nakajima, H., and Wakisaka, Y., "A Study on Reducing Cooling loss in a Partially Insulated Piston for Diesel Engine," SAE Technical Paper No. 2018-01-1279, 2018.

[19] Parsons, C., 2020, "EPA Update on the Cleaner Trucks Initiative," Association of Air Pollution Control Agencies - Energy Committee Meeting, https://www.epa.gov/sites/production/files/2020-10/documents/cti-update-aapca-2020-08-05.pdf

[20] Pless, J. D., Naseri, M., Klink, W., Spreitzer, G., Chatterjee, S., and Markatou, P., 2014, "Development of SCR on High Porosity Substrates for Heavy Duty and Off-Road Applications," SAE International Journal of Commercial Vehicles, **7**(1), pp. 177–185.

[21] Shingne, P. S., Gerow, M. S., Triantopoulos, V., Bohac, S. V., and Martz, J. B., 2014, "A Comparison of Valving Strategies Appropriate For Multimode Combustion Within a Downsized Boosted Automotive Engine—Part I: High Load Operation Within the Spark Ignition Combustion Regime," Journal of Engineering for Gas Turbines and Power, **136**(10), 101507.

[22] Gerow, M. S., Shingne, P. S., Triantopoulos, V., Bohac, S. V., and Martz, J. B., 2014, "A Comparison of Valving Strategies Appropriate for Multimode Combustion Within a Downsized Boosted Automotive Engine—Part II: Mid Load Operation Within the SACI Combustion Regime," Journal of Engineering for Gas Turbines and Power, **136**(10), 101508.

[23] Borgnakke, C. and Sonntag, R. E., 2012, *Fundamentals of Thermodynamics, 8th Edition*, Wiley.

[24] Heywood, J. B., 2018, *Internal Combustion Engine Fundamentals, 2nd Edition*, McGraw-Hill Education.

[25] Wang, Y., Zeng, S., Huang, J., He, Y., Huang, X., Lin, L., and Li, S., 2005, "Experimental investigation of applying miller cycle to reduce NOx emission from diesel engine," Proceedings of the Institution of Mechanical Engineers, Part A: Journal of Power and Energy, **219**(8), pp. 631–638.

[26] Murata, Y., Kusaka, J., Odaka, M., Daisho, Y., Kawano, D., Suzuki, H., Ishii, H., and Goto, Y., 2007, "Emissions suppression mechanism of premixed diesel combustion with variable valve timing," International Journal of Engine Research, **8**(5), pp. 415–428.

[27] Benajes, J., Molina, S., Martín, J., and Novella, R., 2009, "Effect of advancing the closing angle of the intake valves on diffusion-controlled combustion in a HD diesel engine," Applied Thermal Engineering, **29**(10), pp. 1947–1954.

[28] De Ojeda, W., "Effect of Variable Valve Timing on Diesel Combustion Characteristics," SAE Technical Paper No. 2010-01-1124, 2010.

[29] Aoyagi, Y., Yamaguchi, T., Osada, H., Shimada, K., Goto, Y., and Suzuki, H., 2011, "Improvement of thermal efficiency of a high-boosted diesel engine with focus on peak cylinder pressure," International Journal of Engine Research, **12**(3), pp. 227–237.

[30] Ehleskog, M., Gjirja, S., and Denbratt, I., "Effects of Variable Inlet Valve Timing and Swirl Ratio on Combustion and Emissions in a Heavy Duty Diesel Engine," SAE Technical Paper No. 2012-01-1719, 2012.

[31] Zhao, C., Yu, G., Yang, J., Bai, M., and Shang, F., "Achievement of Diesel Low Temperature Combustion through Higher Boost and EGR Control Coupled with Miller Cycle," SAE Technical Paper No. 2015-01-0383, 2015.

[32] Kovács, D. and Eilts, P., "Potentials of the Miller Cycle on HD Diesel Engines Regarding Performance Increase and Reduction of Emissions," SAE Technical Paper No. 2015-24-2440, 2015.

[33] He, X., Durrett, R. P., and Sun, Z., 2009, "Late intake valve closing as an emissions control strategy at Tier 2 Bin 5 engine-out NOx level," SAE International Journal of Engines, **1**(1), pp. 427–443.

[34] Yamaguchi, T., Aoyagi, Y., Osada, H., Shimada, K., and Uchida, N., 2013, "BSFC Improvement by Diesel-Rankine Combined Cycle in the High EGR Rate and High Boosted Diesel Engine," SAE International Journal of Engines, **6**(2), pp. 1275–1286.

[35] Braun, T., Rabl, H.-P., and Mayer, W., "Emission Reduction Potential by Means of High Boost and Injection Pressure at Low- and Mid-Load for a Common Rail Diesel Engine under High EGR Rates," SAE Technical Paper No. 2013-01-2541, 2013.

[36] Gopalakrishnan, V., Vassallo, A., Peterson, R. C., and De la Morena, J., "Effect of High Levels of Boost and Recirculated Exhaust Gas on Diesel Combustion Characteristics at Part Load," SAE Technical Paper No. 2014-01-1245, 2014.

[37] Guan, W., Pedrozo, V., Zhao, H., Ban, Z., and Lin, T., "Exploring the NOx Reduction Potential of Miller Cycle and EGR on a HD Diesel Engine Operating at Full Load," SAE Technical Paper No. 2018-01-0243, 2018.

[38] Guan, W., Pedrozo, V. B., Zhao, H., Ban, Z., and Lin, T., 2020, "Miller cycle combined with exhaust gas recirculation and post–fuel injection for emissions and exhaust gas temperature control of a heavy-duty diesel engine," International Journal of Engine Research, **21**(8), pp. 1381–1397.

[39] Guan, W., Pedrozo, V. B., Zhao, H., Ban, Z., and Lin, T., 2020, "Variable valve actuation–based combustion control strategies for efficiency improvement and emissions control in a heavy-duty diesel engine," International Journal of Engine Research, **21**(4), pp. 578–591.

[40] Gosala, D. B., Shaver, G. M., James E McCarthy, J., and Lutz, T. P., 2021, "Fuel-efficient thermal management in diesel engines via valvetrain-enabled cylinder ventilation strategies," International Journal of Engine Research, **22**(2), pp. 430–442.

[41] Vos, K. R., Shaver, G. M., Joshi, M. C., Ramesh, A. K., and McCarthy, J., 2021, "Strategies for using valvetrain flexibility instead of exhaust manifold pressure modulation for diesel engine gas exchange and thermal management control," International Journal of Engine Research, **22**(3), pp. 755–776.

[42] Vos, K. R., Shaver, G. M., Lu, X., Allen, C. M., James McCarthy, J., and Farrell, L., 2019, "Improving diesel engine efficiency at high speeds and loads through improved breathing via delayed intake valve closure timing," International Journal of Engine Research, **20**(2), pp. 194–202.

[43] de Risi, A., Donateo, T., and Laforgia, D., 2004, "An innovative methodology to improve the design and the performance of direct injection diesel engines," International Journal of Engine Research, **5**(5), pp. 425–441.

[44] Kim, S., Fukuda, D., Shimo, D., Kataoka, M., and Nishida, K., 2017, "Simultaneous improvement of exhaust emissions and fuel consumption by optimization of combustion chamber shape of a diesel engine," International Journal of Engine Research, **18**(5-6), pp. 412–421.

[45] Genzale, C. L., Reitz, R. D., and Musculus, M. P. B., 2008, "Effects of Piston Bowl Geometry on Mixture Development and Late-Injection Low-Temperature Combustion in a Heavy-Duty Diesel Engine," SAE International Journal of Engines, **1**(1), pp. 913–937.

[46] Pickett, L. M. and López, J. J., "Jet-Wall Interaction Effects on Diesel Combustion and Soot Formation," SAE Technical Paper No. 2005-01-0921, 2005.

[47] Minamino, R., Kawabe, T., Omote, H., and Okada, S., "The Effect of Compression Ratio on Low Soot Emission from a Small Non-Road Diesel Engines," SAE Technical Paper No. 2013-24-0060, 2013.

[48] Funayama, Y., Yoshitomi, K., Ishii, M., Nakajima, H., and Fuyuto, T., 2019, "Influence of Combustion Chamber Shape and In-Cylinder Density on Soot Formation in Diesel Combustion," SAE International Journal of Advances and Current Practices in Mobility, **2**(1), pp. 415–425.

[49] Eismark, J. and Balthasar, M., 2013, "Device for reducing emissions in a vehicle combustion engine," US Patent #8,499,735 B2, https://patents.google.com/patent/US8499735?oq=8%2c499%2c735+B2

[50] Eismark, J., Balthasar, M., Karlsson, A., Benham, T., Christensen, M., and Denbratt, I., "Role of Late Soot Oxidation for Low Emission Combustion in a Diffusion-controlled, High-EGR, Heavy Duty Diesel Engine," SAE Technical Paper No. 2009-01-2813, 2009.

[51] Gibble, J. and Amar, P., 2016, *SuperTruck Powertrain Technologies for Efficiency Improvement*, U.S. Department of Energy Vehicle Technologies Office Annual Merit Review.

[52] Eismark, J., Andersson, M., Christensen, M., Karlsson, A., and Denbratt, I., 2019, "Role of Piston Bowl Shape to Enhance Late-Cycle Soot Oxidation in Low-Swirl Diesel Combustion," SAE International Journal of Engines, **12**(3), pp. 233–249.

[53] Gatti, D. and Jansons, M., "One-Dimensional Modelling and Analysis of Thermal Barrier Coatings for Reduction of Cooling Loads in Military Vehicles," SAE Technical Paper No. 2018-01-1112, 2018.

[54] Louis, S., 2014, "Expanding Combustion Knowledge – Lotus AVT System," Lotus Engineering, https://lotusproactive.wordpress.com/2014/04/09/expanding-combustion-knowledge-lotus-avt-system/

[55] Bjärehall, E., Burman, T., and Elamin, E. H., 2017, "Design and Assembly of an EGR-circuit for an MD11 Research Engine," Bachelor's thesis, Chalmers University of Technology Department of Applied Mechanics, https://hdl.handle.net/20.500.12380/250005

[56] 2005, "Smoke Value Measurement With The Filter-Paper-Method," https://www.avl.com/documents/10138/885893/Application+Notes

[57] Pipitone, E., Beccari, A., and Beccari, S., "The Experimental Validation of a New Thermodynamic Method for TDC Determination," SAE Technical Paper No. 2007-24-0052, 2007.

[58] 2010, "Indicating Systems - AVL OT-SENSOR 428," https://www.avl.com/documents/10138/885965/PD+OT+Sensor+428+engl+2010.pdf

[59] Ortiz-Soto, E. A., 2013, "Combustion Modeling of Spark Assisted Compression Ignition for Experimental Analysis and Engine System Simulations," Ph.D. dissertation, University of Michigan, http://hdl.handle.net/2027.42/102314

[60] Ortiz-Soto, E. A., Lavoie, G. A., Martz, J. B., Wooldridge, M. S., and Assanis, D. N., 2014, "Enhanced heat release analysis for advanced multi-mode combustion engine experiments," Applied Energy, **136**, pp. 465–479.

[61] Szybist, J. P., Kirby, S. R., and Boehman, A. L., 2005, "NOx Emissions of Alternative Diesel Fuels: A Comparative Analysis of Biodiesel and FT Diesel," Energy & Fuels, **19**(4), pp. 1484–1492.

[62] Hyvönen, J., Wilhelmsson, C., and Johansson, B., "The Effect of Displacement on Air-Diluted Multi-Cylinder HCCI Engine Performance," SAE Technical Paper No. 2006-01-0205, 2006.

[63] Hohenberg, G. F., 1979, "Advanced Approaches for Heat Transfer Calculations," SAE Transactions, **88**, pp. 2788–2806.

[64] Somhorst, J., Uczak De Goes, W., Oevermann, M., and Bovo, M., "Experimental Evaluation of Novel Thermal Barrier Coatings in a Single Cylinder Light Duty Diesel Engine," SAE Technical Paper No. 2019-24-0062, 2019.

[65] Somhorst, J., Oevermann, M., Bovo, M., and Denbratt, I., 2021, "Evaluation of thermal barrier coatings and surface roughness in a single-cylinder light-duty diesel engine," International Journal of Engine Research, **22**(3), pp. 890–910.

[66] Zhao, C., Sun, J., Nie, X., Tjong, J., and Matthews, D., 2020, "Anodic plasma electrolytic deposition of composite coating on ferrous alloys with low thermal conductivity and high adhesion strength," Surface and Coatings Technology, **398**, p. 126081.

[67] AlRamadan, A. S., Ben Houidi, M., Aljohani, B. S. E., Eid, H., and Johansson, B., 2019, "Compression Ratio and Intake Air Temperature Effect on the Fuel Flexibility of Compression Ignition Engine," SAE International Journal of Advances and Current Practices in Mobility, **2**(2), pp. 623–637.

[68] Powell, T., Killingsworth, N., Hoffman, M., O'Donnell, R., Prucka, R., and Filipi, Z., 2017, "Predicting the gas-wall boundary conditions in a thermal barrier coated low temperature combustion engine using sub-coating temperature measurements," International Journal of Powertrains, **6**(2), pp. 125–150.

[69] Alkidas, A. C., "Performance and Emissions Achievements with an Uncooled Heavy-Duty, Single-Cylinder Diesel Engine," SAE Technical Paper No. 890144, 1989.

[70] Oikawa, H., Nakashima, N., Miyairi, Y., Matsuhisa, T., and Ozawa, T., "Selective Heat Insulation of Combustion Chamber Walls for a DI Diesel Engine with Monolithic Ceramics," SAE Technical Paper No. 890141, 1989.

[71] Marks, D. A. and Boehman, A. L., "The Influence of Thermal Barrier Coatings on Morphology and Composition of Diesel Particulates," SAE Technical Paper No. 970756, 1997.

[72] Büyükkaya, E., Engin, T., and Cerit, M., 2006, "Effects of thermal barrier coating on gas emissions and performance of a LHR engine with different injection timings and valve adjustments," Energy Conversion and Management, **47**(9), pp. 1298–1310.

[73] Garcia, E., Triantopoulos, V., Boehman, A., Taylor, M., and Li, J., "Impact of Miller Cycle Strategies on Combustion Characteristics, Emissions and Efficiency in Heavy-Duty Diesel Engines," SAE Technical Paper No. 2020-01-1127, 2020.

[74] Song, K., Upadhyay, D., and Xie, H., 2021, "An assessment of the impacts of low-pressure exhaust gas recirculation on the air path of a diesel engine equipped with electrically assisted turbochargers," International Journal of Engine Research, **22**(1), pp. 3–21.

[75] Kocher, L., Koeberlein, E., Alstine, D. G. V., Stricker, K., and Shaver, G., 2012, "Physically based volumetric efficiency model for diesel engines utilizing variable intake valve actuation," International Journal of Engine Research, **13**(2), pp. 169–184.

[76] Kim, J. and Bae, C., 2017, "Emission reduction through internal and low-pressure loop exhaust gas recirculation configuration with negative valve overlap

and late intake valve closing strategy in a compression ignition engine," International Journal of Engine Research, **18**(10), pp. 973–990.

[77] Millo, F., Bernardi, M. G., and Delneri, D., 2011, "Computational Analysis of Internal and External EGR Strategies Combined with Miller Cycle Concept for a Two Stage Turbocharged Medium Speed Marine Diesel Engine," SAE International Journal of Engines, **4**(1), pp. 1319–1330.

[78] Lavoie, G. A., Martz, J., Wooldridge, M., and Assanis, D., 2010, "A multi-mode combustion diagram for spark assisted compression ignition," Combustion and Flame, **157**(6), pp. 1106–1110.

[79] Triantopoulos, V., Bohac, S., Martz, J., Lavoie, G., Boehman, A., Sterniak, J., and Assanis, D., 2020, "The Effect of EGR Dilution on the Heat Release Rates in Boosted Spark-Assisted Compression Ignition (SACI) Engines," SAE International Journal of Advances and Current Practices in Mobility, **2**(4), pp. 2183–2195.

[80] Men, Y., Martz, J. B., Curtis, E., and Zhu, G. G., 2019, "A Numerical Study of an Electrically Assisted Boosting System for Turbocharged Diesel Engines," *ASME 2019 Dynamic Systems and Control Conference*, Vol. 59155, American Society of Mechanical Engineers, doi:10.1115/DSCC2019-9039.

[81] Tree, D. R., Wiczynski, P. D., and Yonushonis, T. M., "Experimental Results on the Effect of Piston Surface Roughness and Porosity on Diesel Engine Combustion," SAE Technical Paper No. 960036, 1996.

[82] Wakisaka, Y., Fukui, K., Kawaguchi, A., Iguma, H., Yamashita, H., Takada, N., Nishikawa, N., and Yamashita, C., "Thermo-Swing Wall Insulation Technology; - A Novel Heat Loss Reduction Approach on Engine Combustion Chamber -," SAE Technical Paper No. 2016-01-2333, 2016.

[83] Moffat, R. J., 1988, "Describing the uncertainties in experimental results," Experimental Thermal and Fluid Science, **1**(1), pp. 3–17.